Reacting surface nanodroplets and sensitive chemical detection

by

Zhengxin Li

A thesis submitted in partial fulfillment of the requirements for the degree of

Doctor of Philosophy

in

Chemical Engineering

Department of Chemical and Materials Engineering
University of Alberta

Abstract

Due to the large surface-to-volume ratio, micro-sized droplets (i.e. a few microns in radius) provide a unique compartmentalized environment for biphasic processes (i.e. biphasic reaction and liquid-liquid microextraction) that are reported to be cost-effective, streamlined, and high-throughput. However, we still lack a quantitative understanding of the mechanisms and kinetics of chemical reactions and mass transfer with micro-sized droplets, especially for droplets reacting with reactants from the external phase.

This Ph.D. thesis focused on reactions and mass transfer with surface nanodroplets, the liquid microdomains sitting on a solid surface and immersed in an immiscible surrounding liquid. As the three-phase contact line of nanodroplets was immobilized on the solid substrate, the evolution of droplet morphology and droplet size can be followed in situ by optical observation methods with high temporal and spatial resolution. Based on our achieved research progress on surface nanodroplets, systematic research was performed to understand the effects of external flow, droplet size, and many other conditions on the reaction kinetics between droplets and an external phase.

The mass transfer of reactants and products between the bulk and the interface can be a determining factor of the kinetics of biphasic reactions (i.e. reactions involving reactants from two immiscible phases), as reactants isolated in immiscible phases need to be transported together to react, and products need to be removed from the reacting site. Since the external flow enhanced the mass transfer between the droplet and surrounding phase, and interface-crossing mass transfer is more efficient for a

smaller droplet with higher a surface-to-volume ratio, we expected that the biphasic reaction would be faster in smaller droplets or under faster flow rates.

To address our assumptions, the on-drop neutralization between oleic acid surface nanodroplets and sodium hydroxide from an external flow was followed in situ by an optical microscope. By tracing the droplet shrinkage from produce dissolution, we confirmed that the overall kinetics can be enhanced by increasing the external flow rate or reducing the droplet size. Our theoretical analysis attributes the faster kinetics to 2 factors: i. Product diffusion in the Prandtl-Blasius boundary layer, which should be faster at a higher linear flow rate (or Peclet number Pe) and in smaller droplets; ii: Surface-to-volume-ratio-associated product accumulation inside the droplet. The quantitative analysis coupling two factors above predicts the overall kinetics scale with $Pe^{1.5}R^2$ (R is the droplet radius), consistent with our experimental results.

Another case of the faster reaction in smaller droplets was from the dehydrocoupling of siloxane by water diffusing from the external phase into the droplet. From the reaction, generated hydrogen gas triggered the formation of hydrogen bubbles inside the droplet. Followed by a confocal microscope, the bubble formation was found to be faster in smaller droplets. Additionally, a decreasing reaction rate profile from the droplet surface to the droplet center was found, as reflected by the slower bubble formation far from the droplet rim. Our theoretical analysis attributed the non-uniform reaction kinetics to the balance between water diffusion and consumption by the reaction.

Due to the slow diffusion, the concentration of water decrease dramatically from the interface and was found to be depleted in a few microns. For micro-sized droplets, such a diffusion length was already enough for reactant to penetrate the droplet, however, for a macroscopic drop (millimeter size or larger), such a small diffusion length only allows for reactions nearing the interface. In this case, the efficiency of the reaction is dramatically limited by the interface-crossing mass transfer.

Taking the advantages of surface pinning and efficient mass transfer, this thesis

further explored the application of surface nanodroplets in liquid-liquid extraction and chemical detection. In a long capillary tube, octanol surface nanodroplets were prepared to extract triclosan and chlorpyrifos from the aqueous flow. After extraction, octanol droplets were collected by capillary force, and analyzed by ultraviolet-visible spectroscopy (UV-Vis). A good linear relationship between analyte concentration and absorbance, with a limit of detection (LOD) of $\sim 10^{-9}$ M, which is comparable to prior arts, could be achieved both for triclosan and chlorpyrifos. The versatility of the setup was further confirmed by coupling with gas chromatography-mass spectrometry (GC-MS), and fluorescence microscopy, suggesting a powerful method for rapid extraction and detection in tandem with offline analytic instruments.

Preface

This thesis is an original work by Zhengxin Li, which is composed of several papers that have been published, submitted, or is under preparation.

Published Journal Papers:

1. **Zhengxin Li**, Akihito Kiyama, Hongbo Zeng, Detlef Lohse, Xuehua Zhang. Speeding Biphasic Chemical Reactions with Surface Nanodroplets. *Lab on a Chip*, 2020, 20(16), 2965-2974 [1].

Zhengxin Li performed the experiments and data analysis, and wrote the manuscript. Akihito Kiyama helped with the data analysis, writing, and illustration. Xuehua Zhang was involved in the experimental design and supervised the work. All the authors contributed to the discussion and commented on the manuscript.

2. **Zhengxin Li**, Akihito Kiyama, Hongbo Zeng, Xuehua Zhang. Size Effect on the Reaction Rate of Surface Nanodroplets. *The Journal of Physical Chemistry C*, 2021, 125(28), 15324-15334 [2].

Zhengxin Li performed the experiments and data analysis, and wrote the manuscript. Akihito Kiyama helped with the data analysis, writing, and illustration. Xuehua Zhang was involved in the experimental design and supervised the work. All the authors contributed to the discussion and commented on the manuscript.

3. **Zhengxin Li**, Hongbo Zeng, Xuehua Zhang. Growth Rates of Hydrogen Microbubbles in Reacting Femtoliter Droplets. *Langmuir*, 2022, 38(21), 6638–6646 [3].

Zhengxin Li performed the experiments and data analysis, and wrote the manuscript.

Xuehua Zhang was involved in the experimental design and supervised the work. All the authors contributed to the discussion and commented on the manuscript.

Submitted Journal Paper:

1. **Zhengxin Li**, Hongyan Wu, Jae Bem You, Xiaomeng Wang, Hongbo Zeng, Detlef Lohse, Xuehua Zhang. Surface nanodroplet-based nanoextraction combined with offline analytic methods for detection and quantification. Submitted to *Langmuir*. Zhengxin Li performed the experiments and data analysis, and wrote the manuscript. Hongyan Wu, Jay Bem You, and Xiaomeng Wang helped with the data collection and writing. Xuehua Zhang was involved in the experimental design and supervised the work. All the authors contributed to the discussion and commented on the manuscript.

Acknowledgments

When I recall my four-year PhD career, I would like to express my gratitude for the support and help from many people.

First and foremost, I would like to appreciate my supervisors Professor Xuehua Zhang as well as Professor Hongbo Zeng, for all your constant guidance, support, patience, and encouragement throughout the each stage of my PhD study. All the invaluable treasures you taught me, including ability of thinking independently, critically, and creatively, skills of writing and presentation, time management, knowledge, and also scientific literacy, will be engraved on my heart and memory, and permanently help me with my life in the future.

I greatly thank to Dr. Jiasheng Qian and Dr. Akihito Kiyama, for all your suggestions, help, and encouragement both in my academy and life. I also thank to my colleagues, many fellow and researchers from many projects, including but not limited to (in no particular order) Dr. Stephen Ogg, Dr. Brendan Dyett, Dr. Jae bem you, Dr. Lei Bao, Dr. Amir Muhammad, Dr. Zixiang Wei, Jia Meng, Qiuyun Lu, Yawen Gao, and all other members in Soft Matter & Interfaces Group. Their help and company in the past years becomes an important section of my life.

I would like to acknowledge the Natural Science and Engineering Research Council of Canada (NSERC), and Future Energy Systems (Canada First Research Excellence Fund), for supporting me with the research funding, tuition, and the living fee, which made my PhD study goes smoothly.

I would also like to thank the administration staff and technical staff in Department of Chemical Engineering at University of Alberta for their support and assis-

tance during my PhD study.

Last but the most important, my deepest gratitude goes to my parents, for all your unconditional love, support, tolerance, encouragement, and understanding.

Table of Contents

List of Tables

List of Figures

List of Symbols

Latin

$[OA]$ Oleic acid concentration in the droplet

$[OH^-]_{sur}$ Alkali concentration at the droplet surface

$\bar{U}$ Average linear flow rate

$\dot{m}(D_s)$ Local production rate of hydrogen by the chemical reaction

$\dot{m}_{pr}$ Rate of product mass loss

$\dot{R}$ Dissolution rate of surface droplet

$\dot{r}(D_s)$ Local average growth rate of hydrogen bubbles

A Absorbance/Base area of surface droplet

A_b Base area of surface droplet

a_b Base area of surface bubble

$A_{(t)}$ Interfacial area of surface droplet

A_{283} Absorbance at 283 nm

A_{291} Absorbance at 291 nm

Ar Archimedes number

b Length of the light path

C_d Analyte concentration in extractant droplet

C_w Analyte concentration in water sample

$C_w(D_s)$ Local water concentration with the distance D_s from the droplet surface

$c_\infty(t)$ Oil concentration in bulk

$c_{pr,\infty}$ Product concentration in bulk

$c_{pr,in}$ Product concentration in the droplet

$c_{pr,sur}$ Product concentration at the droplet surface

$c_{re,bulk}$ Reactant concentration in bulk

$c_{re,sur}$ Reactant concentration at the droplet surface

$c_{s,w}$ Oil solubility in poor solvent

C_{SiH} Siloxane concentration in the droplet

D Diffusion coefficient

D_b Distance from bubble center to the droplet rim

D_s Distance from bubble center to the droplet surface

EF Enrichment factor

g Acceleration of gravity

h channel height

k Reaction rate constant

K_r Reaction equilibrium constant

k_r Reaction rate constant

Pe Peclet number

Q Volume flow rate

R Base radius of surface droplet

r Distance from bubble center to the droplet rim

R_0 Initial base radius of surface droplet

R_b Base radius of surface droplet

R_f Final radius of surface droplets during the solvent exchange

R_s Radius of the curvature

SC Surface coverage

SC_0 Initial surface coverage

t Time

t_0 Time zero

t_e The time when the droplet was 1.2 μm in base radius

U Linear flow rate

V Volume

V_f Final volume of surface droplet during the solvent exchange

w Channel width

Greek

Δ Laplace operator

ϵ Characteristic diffusion length of water in surface droplets/molar absorptivity

λ Thickness of diffusion boundary layer

μ Viscosity

Nablae operator

∇ Nabra operator

ν Kinematic viscosity

ρ Density

ρ_{oil} Oil density

$\sigma_{liq-air}$ Interfacial tension between liquid and air

τ	Droplet life time
θ	Contact angle of surface droplet on the solid substrate
θ_f	Final contact angle of surface droplet on the solid substrate
$\zeta(t)$	Oversaturation level

Chapter 1

Introduction

1.1 Motivations and thesis objectives

Small-size droplets are omnipresent in nature and technology, including lab-on-chip, emulsions, aerosols, sneezing and coughing, cell metabolism compartments, heterogeneous catalysis, polymer synthesis, micro-extraction, among many others [4–11]. The employment of small droplets in biphasic processes (i.e. biphasic reactions and liquid-liquid microextraction) offers advantages such as enhanced mass transfer, highly specified chemical conversion, and streamlined produces [12]. With the large surface-to-volume ratio, microdroplets are desirable for efficient interface-crossing mass transfer between two immiscible phases [13]. With these benefits, microdroplets are widely employed in the fabrication of advanced bio- and nano-materials [14], drug discovery [15, 16], fast and sensitive chemical analysis [17], and among many others.

However, for droplet systems with a large surface area like emulsion droplets and aerosol droplets, they all exhibit most classical behaviours of metastable colloids, such as Brownian motion, reversible phase transitions as a result of droplet interactions, and irreversible transitions that generally involve the destruction of the emulsion [18]. For example, coalescence consists of the rupture of the thin liquid film forming between two adjacent droplets. Then, a hole takes shape in the thin film and grows, resulting in the fusion of two adjacent droplets. Ultimately, the dispersed system is destructed and two macroscopic immiscible phases are recovered. To maintain the

metastable biphasic system, stabilizers such as surfactants or particles are required to cover the surface of the droplet, which will tune the interphase properties of the droplet interface. Features listed above for bulk droplets are the reason why it is so hard to track biphasic processes of droplets as time goes by. Apart from the unstable system and tracing reaction process, influence from the interface between two phases on dynamics and kinetics of the chemical reaction and mass transfer is still unclear.

Surface nanodroplets immobilized on the solid-liquid interface with a long lifetime and stability can be produced with unprecedented flexibility in the aspects of controlling droplet sizes, morphology, and droplet compositions by solvent exchange. As a platform, chemical reaction and mass transfer within surface nanodroplets can be well followed with optical methods such as confocal microscopy, Fourier-transform infrared spectroscopy (FTIR) and many others. With high temporal and spatial resolutions from these optical techniques, the kinetics of the chemical reaction and mass transport crossing the droplet interface and inside the droplet can be quantitatively analyzed, understand, and thus we can establish the basis for controlling biphasic processes within micro-sized droplets.

Therefore, based on the foundation of research on surface nanodroplets, this Ph.D. project aims to understand factors such as droplet size, droplet composition, the geometry and flow rates of the external flow on the biphasic reactions and mass transfer between reacting surface nanodroplets and the surrounding phase. Furthermore, we expected that surface nanodroplets with high efficiency of mass transfer can be taken as a template for liquid-liquid nanoextraction and chemical sensing. Specifically, the objectives of this Ph.D. project were proposed as below:

1. To understand the effects of the rate and geometry of the external flow on the reaction kinetics and mass transfer of reacting surface nanodroplets. To understand interactions between reacting droplets (collective effects).

2. To understand the effects of droplet size and droplet composition on the reaction kinetics and mass transfer of reacting surface nanodroplets.

3. To understand the formation and growth of nanobubble triggered by a gas-generating reaction and involved reaction kinetics and mass transfer within the droplets.

4. To develop the surface nanodroplet as a template for liquid-liquid extraction with versatility and simplified procedures.

1.2 Thesis outline

According to the motivations and aims of this Ph.D. project, this thesis is outlined chapter by chapter.

Chapter 1. Introduction

This chapter provides a brief introduction of the background and motivations, the objectives, and the structure of the thesis.

Chapter 2. Literature review

This chapter is a literature review of the general information relevant to this Ph.D. research. This chapter mainly reviews the background and mechanisms of droplet reaction, droplet-based microextraction, formation, dissolution, and applications of surface nanodroplets.

Chapter 3. Speeding up biphasic reactions with surface nanodroplets

(*Published paper: Li, Z., Akihito, K., Zeng, H., Lohse, D., Zhang, X. Speeding up biphasic reactions with surface nanodroplets. Lab Chip, 2020, 20, 2965-2974*)[1]

In this chapter, we experimentally and theoretically investigate the rate for biphasic chemical reactions between acidic nanodroplets on a substrate surface and basic reactants in a surrounding bulk flow. The reaction rate is measured by droplet shrinkage as the product is removed from the droplets by the flow. In our experiments, we determine the dependence of the reaction rate on the flow rate and the solution con-

centration. The theoretical analysis predicts that the life time τ of the droplets scales with Peclet number Pe and the reactant concentration in the bulk flow $c_{re,bulk}$ as $\tau \propto Pe^{-3/2} c_{re,bulk}^{-1}$, in good agreement with our experimental results. Furthermore, we found that the product from the reaction on an upstream surface can postpone the droplet reaction on a downstream surface, possibly due to the adsorption of interface-active products on the droplets in the downstream. The time of the delay decreases with increasing Pe of the flow and also with increasing reactant concentration in the flow, following the scaling same as that of the reaction rate with these two parameters. These findings provide insight for the ultimate aim to enhance droplet reactions under flow conditions.

Chapter 4. Size Effect on Reaction Rate of Surface Nanodroplets

(*Published paper: Li, Z., Akihito, K., Zeng, H., Zhang, X. Size Effect on Reaction Rate of Surface Nanodroplets. J. Phys. Chem. C, 2021, 125, 28, 15324–15334*)[2]

In this chapter, surface nanodroplets were employed to quantitatively understand the size effect on the chemical reaction rate of droplets. In our systems, a surface-active reactant in pure or binary nanodroplets reacted with the reactant in the bulk flow. Meanwhile, the product was removed from the droplet surface. The shrinkage rate of the nanodroplets was characterized by analyzing the lateral size as a function of time, where the droplet size was solely determined by chemical reaction rate at a given flow condition for the transport of the reactant and the product. We found that the overall kinetics increases rapidly with the decrease of droplets lateral radius R, as $dR/dt \sim R^{-2}$. The faster increase in the concentration of the product in smaller droplets contributes to accelerating reaction kinetics. The enhancement of reaction rates from small droplet sizes was further confirmed when a non-reactive compound presented inside the droplets without reducing the concentrations of the reactant and the product on the droplet surface. The results of our study improve the understand-

ing of chemical kinetics with droplets. These findings highlight the effectiveness of small droplets for the design and control of enhanced chemical reactions in a broad range of applications.

Chapter 5. Growth Rates of Hydrogen Microbubbles in Reacting Femtoliter Droplets

(*Published paper: Li, Z., Zeng, H., Zhang, X. Growth Rates of Hydrogen Microbubbles in Reacting Femtoliter Droplets. Langmuir, 2022, 38, 21, 6638–6646*)[3]

In this chapter, we investigate the local rate of gas-evolution reaction within femtoliter droplets immobilized on a solid surface. The growth rate of hydrogen microbubbles ($\geq$ 500 nm in radius) produced from the reaction was measured online by high-resolution confocal microscopic images. The growth rate of bubbles was faster in smaller droplets, and of bubbles near the three-phase boundary in the same droplet. The results were consistent for both pure and binary reacting droplets and on substrates of different wettability. Our theoretical analysis based on diffusion, chemical reaction and bubble growth in a steady state predicted that the concentration of the reactant diffusing from the surrounding depended on the droplet size and the bubble location inside the droplet, in good agreement with experimental results. Our results reveal that the reaction rate may be spatially non-uniform in the reacting microdroplets. The findings may have implications for formulating chemical properties and uses of these droplets.

Chapter 6. Surface nanodroplet-based extraction combined with offline analytic tools for detection and quantification

(*Under preparation: Li, Z., Wu, H., You, J., Wang, X., Zeng, H., Lohse, D., Zhang, X. Surface nanodroplet-based extraction with offline analytic methods for detection and quantification.*)

To expand the versatility of the liquid-liquid extraction based on surface nanodroplets, in this work, the formation of octanol surface nanodroplets and extraction

were performed inside a 3-meter Teflon capillary tube. After extraction, surface nanodroplets were collected by injecting air into the tube, by which the contact line of surface droplets was depinned from the solid substrate by capillary force. As the capillary allows for the formation of $\sim 10^{12}$ surface nanodroplets on the capillary wall, $\geq$ 2 mL octanol can be collected after extraction. The volume of the collected octanol was enough for the analysis of offline analytical techniques such as UV-Vis, GC-MS, and others. Coupled with UV-Vis, reliable extraction and detection of two common water pollutants, triclosan and chlorpyrifos, was shown by a linear relationship between the analyte concentration in the sample solution and UV-Vis absorbance. The limit of detection (LOD) was 2×10^{-9} M for triclosan (~ 0.58 μg/L) and 3×10^{-9} M for chlorpyrifos (~ 1.05 μg/L). To confirm the flexibility of extraction, the collected surface droplets were also analyzed via gas chromatography (GC) and fluorescence microscopy.

Chapter 7. Conclusions and Future work

This chapter summarizes the main conclusions and plans for future research.

Chapter 2

Literature review

2.1 Enhanced chemical reactions in microdroplets

The kinetics of chemical reactions in microdroplets have been reported to be dramatically accelerated compared with their bulk counterparts. For instance, Pomeranz-Fritsch synthesis of isoquinoline was found by a factor of 10^6 faster in microdroplets than in bulk [19]. Cooks and Zare investigated a wide range of chemical reactions within microdroplets on flight produced by atomized sprays [20–24]. They found that reactions are extremely slow occur readily in flying droplets, including the formation of biomolecules, such as sugar phosphate and ribonucleoside [22, 23]. The shifted balance of reactions and accelerated synthesis of these complex biomolecules outside of living systems may pave the way to explain the origin of life on the early earth [25–27].

Enhanced chemical kinetics was also reported in droplets not produced by atomized spray. For instance, the formation of hydroperoxide, which is thermodynamically unfavourable in bulk, spontaneously reacts in aerosol droplets formed by vapour condensation [28]. Mannich reaction was also found to be much faster in emulsion droplets with liquid-liquid interface [29]. Additionally, new intermediates or products not present in the bulk reaction can be produced within droplets, such as isomers during phosphorylation between phosphoric acid and sugars [22].

Multiple hypotheses have been proposed to interpret the enhanced chemical re-

action within small droplets. The accelerated reaction rate was attributed to the faster electron transfer [30–33] and chemical configuration of reactant molecules at the liquid-gas interface [22, 23, 34]. As shown in Figure 2.1, the lowered energy barrier speeds up the Mannich reaction at the interface. Besides, water molecules near the air-water interface can easily auto-ionize, which favours the redox reaction at the droplet surface. An example is the enzymatic digestion of proteins was found to be accelerated in droplets [35].

For droplets in flight, a local electric field from a general effect of surface enrichment and orientation alignment was found at the droplet surface, which may partially account for the enhanced chemical kinetics of droplets in air [36, 37]. As a result of electrostatic repulsion, an ordered orientation of the molecules at the droplet surface contributes to a lower energy barrier than in bulk [38]. Additionally, as the droplet decreases in size, the enhanced mass transfer crossing the interface was introduced by the higher surface-to-volume ratio, thus accelerating the overall reaction kinetics [1, 2, 29, 39]. The flow of the external phase may also contribute to the turbulence in the droplet, by which the reaction can be enhanced with the fast diffusion and mixing inside the droplet [40].

Despite multiple possible mechanisms being proposed to explain the unique properties of droplet reaction, it remains unclear what the quantitative correlations are among the droplet size, external flow, mass transfer, and reaction kinetics. For the further understanding, systematic researches were performed in situ in Chapters 3, 4, and 5 to explicit the above knowledge gaps.

2.2 Droplet-based liquid-liquid microextraction

Sensitive detection and analysis of chemicals is crucial in many areas including water pollutant detection [41, 42], air quality monitoring [43, 44], analysis of drugs and pharmaceuticals [45, 46], biological sensing [47, 48], and food quality control [49–51]. To enhance the detection sensitivity, the compounds of interest are often pre-

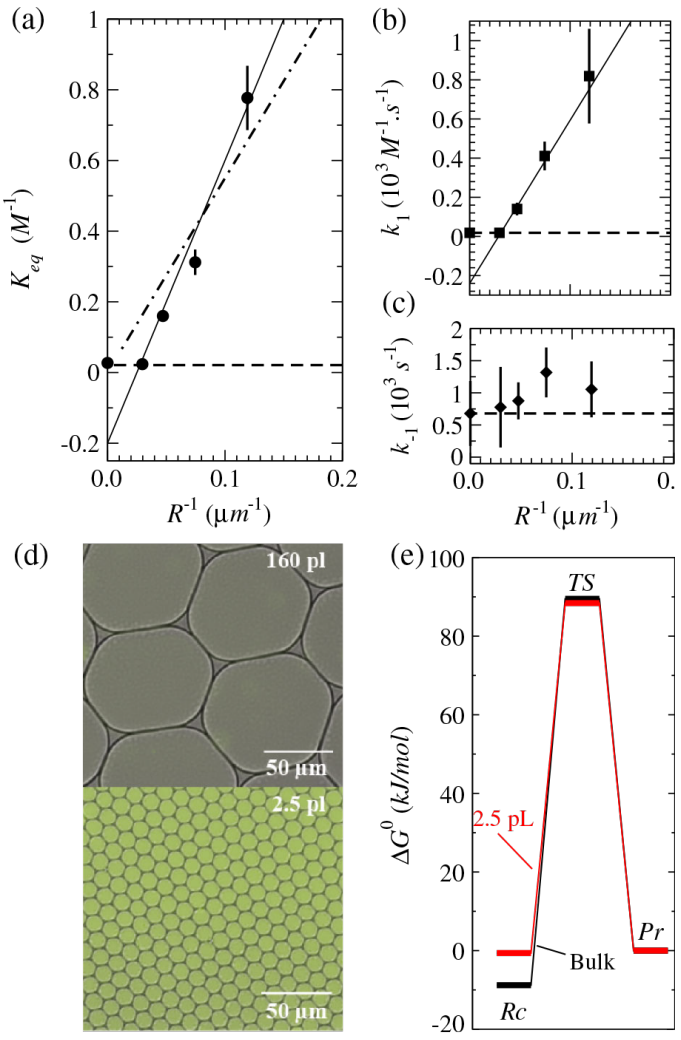

Figure 2.1: The formation of a fluorescent amine was enhanced with the decrease of the droplet size. The equilibrium constant K (a) and forward rate constant k_1 (b) were found to be proportional to the droplet radius R. The backward rate constant (c) was not a function of R. (d) The enhanced formation of the fluorescent amine in smaller droplets. Results from (a)-(c) suggest that the free energy of reactant at the 2.5 pL droplet surface was higher than in bulk (e). With permissions from [29]. Copyright (2014) American Physical Society

concentrated using an extractant material. Liquid-liquid microextraction has been widely used to achieve this purpose.

Liquid-liquid extraction, usually named partitioning, is used as a separation technique to transfer the target analyte from sample solution to an immiscible extractant based on solubility differences [52]. As a result of slow mass transfer between two macroscopic phases, conventional liquid-liquid extraction require excessive processes including shaking, centrifuging, and filtration, which consumes time and energy [53]. Moreover, conventional liquid-liquid extraction require large amounts of toxic organic solvents [54]. To enhance the mass transfer and to simplify the complicated extraction processes, microdroplets with a higher surface-to-volume ratio were employed to enhance the extraction efficiency.

Single drop microextraction (SDME), which is inexpensive, nearly solvent-free, and easy to operate, is widely used after its introduction over twenty years ago [54]. During SDME, a drop of extractants with the volume of 1 to 10 μL was held by the syringe needle and extract analytes from sample solution [55]. Depending on the volatility of the analyte, the drop can be either immersed in or out of the sample [56]. By repeatedly withdrawn into and expelled out of the syringe, the extraction efficiency of SDME can be enhanced.[57]. The organic drop held by the tip was also immersed in a continuously flowing liquid sample, named continuously flow microextraction (CFME), to further improve the mass transfer between two phases [58]. While extracting some nitroaromatic compounds and chlorobenzenes by CFME, the enrichment factor can go up to 1000 in 10 min [58].

However, with the limitation of the syringe precision, it is hard to produce a droplet smaller than 1 μm for SDME. As the mass transfer crossing the interface is inversely proportional to surface-to-volume ratio of the droplet, droplets with smaller sizes to further accelerate the extraction process. In this case, dispersive microdroplets formed by self-emulsification are applied to accelerate the extraction process, which is known as dispersive liquid-liquid microextraction (DLLME) [59].

DLLME was firstly reported in 2006 to preconcentrate polycyclic aromatic hydrocarbons (PAHs) in water samples [59]. After it was first introduced, DLLME was then widely used as a separation technique for its simple procedures and high efficiency [60]. For a standard DLLME, an extractant solvent, the aqueous sample solution, and a disperser solvent are required to form emulsion droplets. The extractant solvent must be insoluble to the aqueous phase, while the disperse solvent should be a polar solvent that is soluble in the aqueous phase and the extractant solvent.

Figure 2.2 sketches the standard processes of DLLME. After adding the extractant solvent and disperser solvent into the water sample, a cloudy emulsion of extractant droplets spontaneously formed to extract analytes from the sample. The self-emulsification above was also named as ouzo effect [61]. Apart from self-emulsification, various disperse techniques including shaking [62], ultrasound-assisted emulsification [63], vortex-assisted emulsification [64], surfactant-assisted emulsification [65], and microwave-assisted emulsification [66] were employed to form emulsion droplets. After extraction, centrifugation was performed to separate the sample solution and the extractant solvent. Then the extractant solvent containing analytes will be analyzed with various techniques, including GC-MS [51, 67], HPLC-MS [68, 69], UV-Vis [70], and atomic absorption spectrometry [42]. With the large contact surface between the dispersive phase and the continuous phase, DLLME promises advantages such as simple procedures, rapid mass transfer, and high enrichment factor.

However, the extractant solvents used in DLLME such as chlorobenzene, chloroform, and carbon tetrachloride, are usually toxic [60]. DLLME also requires a large amount of disperser solvent such as alcohol, which is not only environmentally unfriendly, but also decreases the partition coefficient of the analytes in the extractant phase. Moreover, dedicated instruments are necessary for DLLME to separate and collected the emulsion droplet. To address these drawbacks, surface nanodroplets were employed for the liquid-liquid extraction. The introduction and characteristics of surface nanodroplets will be discussed later in Section 2.3. The conceptions, advan-

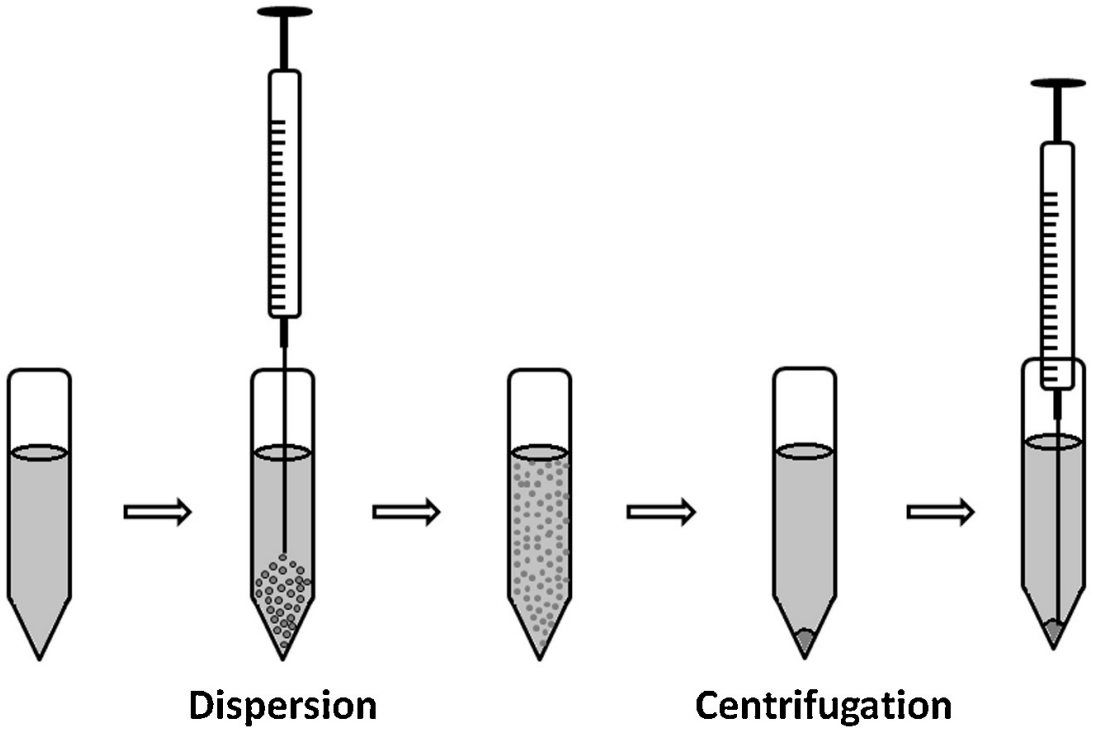

Figure 2.2: Sketch of standard DLLME processes. With permissions from [60]. Copyright (2014) Elsevier Ltd.

tages, and knowledge gaps of liquid-liquid extraction based on surface nanodroplets will be further discussed in Section 2.7.

2.3 Surface nanodroplets

Surface nanodroplets are liquid domains located on a solid surface immersed in another immiscible liquid environment [4, 71]. Assuming surface nanodroplets are in a shape of spherical-cap, radius of the droplet curvature R, volume V, base radius L, droplet height H, and contact angle θ of a surface nanodroplet are sketched in Figure 2.3.

Compared to their macroscopic counterpart, surface nanodroplets are much smaller both in size and in aspect ratio [72]. Their lateral size is usually ranging from microns to tens of microns, while their height is as small as hundreds of nanometers (less than 1 μm). The term 'nano' refers to at least one dimension less than 1 μm.

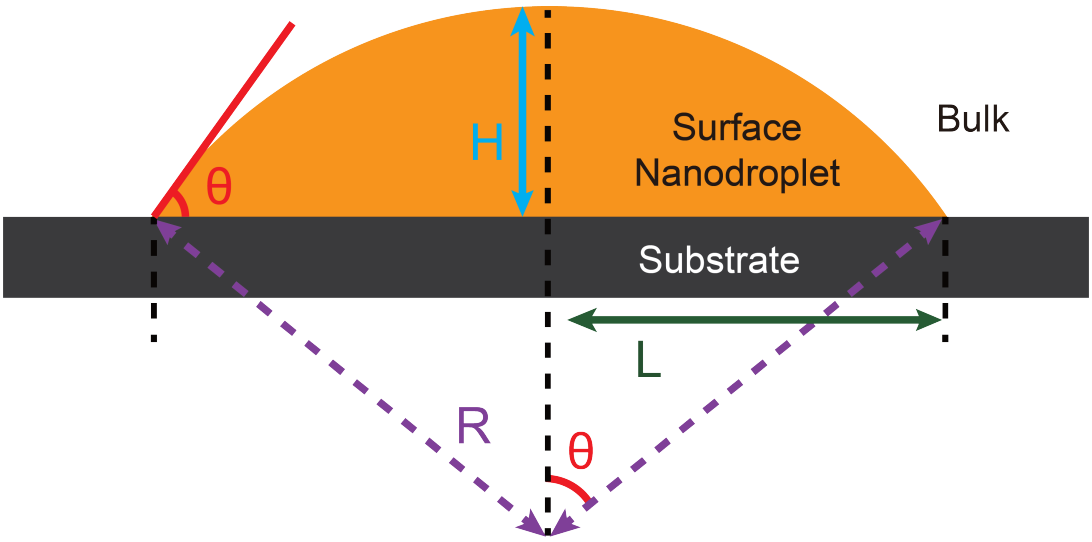

Figure 2.3: Sketch of a surface droplet in a shape of spherical cap on a solid substrate, and definitions of parameters.

Such dimensions correspond to volume in femtoliters, which is already six orders of magnitude smaller than a nanoliter. Compared with hundreds of billions of molecules in a nanoliter droplet, a femtoliter droplet only accommodate hundreds of thousands of molecules. Due to the dramatic decrease of the droplet volume, the properties of surface nanodroplets vary in multiple aspects. For instance, the mass transport crossing the interface, such as evaporation and dissolution of surface nanodroplets, can be extremely rapid as a result of the high surface-to-volume ratio.

Apart from their morphology characteristics, the lifetime of surface nanodroplets can be flexibly controlled. This is because the stability of surface nanodroplets is tightly related to the saturation level of droplet liquid in the surrounding phase. They are quite stable in a saturated environment and can survive for several days. In sharp contrast, their fast dissolution only takes several seconds in a highly unsaturated environment. Such a long lifetime not only results from low interface energy between droplets and substrate, but also as the three-phase contact line of surface nanodroplets is pinned on the substrate [73–75].

With advantages such as soft interface, high surface-to-volume ratio, stability, and immobility, surface nanodroplets can be taken as an ideal platform for the investiga-

tion of surface nanodroplets attracts significant interest, both in fundamental study and in applications. For the fundamental study, research about nano-scale surface droplets paves the way for understanding theories of wetting and heterogeneous nucleation. For the application side, surface nanodroplets are of great potential in many fields, including lubrication [76], highly efficient liquid-liquid micro-extraction and analysis [77–80], high-resolution near-field imaging [81, 82], high throughput chemical micro-reactors[83, 84], and 3D printing of optical and electronic devices [85, 86].

As a platform, chemical reaction and mass transfer within surface nanodroplets can be well followed with optical methods such as confocal microscopy, Fourier-transform infrared spectroscopy (FTIR) and many others. With high temporal and spatial resolutions from these optical techniques, the kinetics of the chemical reaction and mass transport crossing the droplet interface and inside the droplet can be quantitatively analyzed, understand, and thus we can establish the basis for controlling biphasic processes within micro-sized droplets. Moreover, surface nanodroplets with high surface-to-volume ratio, high stability, and immobility can also be employed as an ideal platform for the droplet extraction from a sample flow. To address the knowledge gaps discussed in above sections, surface nanodroplets were employed in all following Chapters for the study of droplet reaction and droplet-based liquid-liquid extraction.

2.4 Ouzo effect

Well-known aperitifs, such as Ouzo in Greece and Pastis in France, are ethanol extracts of anise seeds. While diluted in water, the dissolved anise oil insoluble to water nucleates out as micro-sized oil droplets, leading to the cloudy mixture remaining for a long period [87]. The phenomenon above, named the ouzo effect, was generally taken as an approach for producing dispersed emulsion droplets without using any agitation or stabilizers such as surfactants and nanoparticles [88, 89]. The strategy is also called as solvent displacement [90], solvent shifting [91], nanoprecipitation, or

spontaneous emulsification [92], was applied to produce highly homogeneous droplets for producing nanoparticles as pharmaceutical products [87], or for drug delivery [93].

Producing dispersed micro-sized droplets by the ouzo effect is cost-effective, energetically free, and easy to operate. It only involves three compounds: water, a hydrophobic oil that is immiscible with water, and a co-solvent such as ethanol, which is miscible to both water and oil. The hydrophobic oil was at first dissolved in co-solvent and then diluted by water. The addition of water leads to the decrease of oil solubility in the mixture, building up oil oversaturation. As a result, oil droplets nucleate out and form emulsions. Water and oil can also be exchanged in the procedure above, for the formation of water emulsion droplets.

In the phase diagram of an oil/water/co-solvent ternary system with the ouzo effect, an existing metastable region was named the ouzo region. In the ouzo region, oil can nucleate out and form emulsion droplets, as sketched in Figure 2.4. The ouzo region is located between the binodal line and the spinodal line. The binodal line and the spinodal line are respectively the thermodynamic equilibrium for phase separation and the stability boundary of the dispersed droplets system. Though the Gibbs free energy of the dispersed droplets system at the ouzo region has not been minimized, an energy barrier exists here to stabilize the emulsions and prevent them from thorough phase separation immediately. Droplet size in ouzo emulsion depends on the droplet liquid concentration in the mixture and can be predicted by Smoluchowski kinetic model [94].

2.5 Solvent exchange

Similar to the principle of the ouzo effect, a general lab protocol named solvent exchange was recently developed to produce a large number of surface nanodroplets on solid substrates. During a standard solvent exchange process, the solution of high oil solubility is replaced by another miscible solution of lower oil solubility on a substrate with a suitable wettability for droplet nucleation and growth [95]. Figure

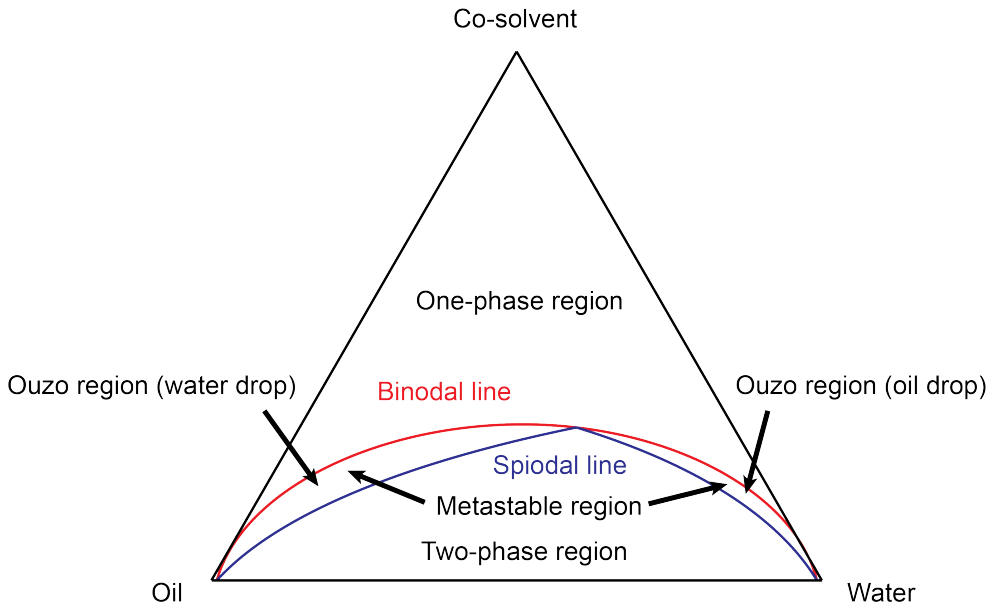

Figure 2.4: Ternary phase diagram of an oil/water/co-solvent ternary system. Ouzo effect occurs when solution transfer from the one-phase region into the metastable region between the binodal line (red) and spinodal line (blue).

2.5A sketches the fluid channel in which solvent exchange is performed. During the solvent exchange, local oversaturation of the droplet liquid can be created in the mixing front due to the solubility gap between the two solutions. When the mixing front of two solutions passes through the substrate, droplet liquid will precipitate from the oversaturation and nucleate on the substrate, as sketched in Figure 2.5B [4, 96]. Droplets will continue to grow until the oversaturation of droplets liquid is depleted by droplet formation.

Compared to other techniques for producing surface nanodroplets, such as immersing with microcavities, emulsion adsorption, and chemical reactions, the solvent exchange is easy to operate and can produce a large number of droplets with uniform and repeatable size distribution and number density [4, 96]. Besides, droplet size distribution and droplet morphology can be tuned and well-controlled during the solvent exchange by adjusting several factors, including solution composition [97, 98], flow geometries such as flow rate and gravity effect [4, 96], temperature [99], substrate properties [4], external interference like an acoustic field [100], etc. With the simplic-

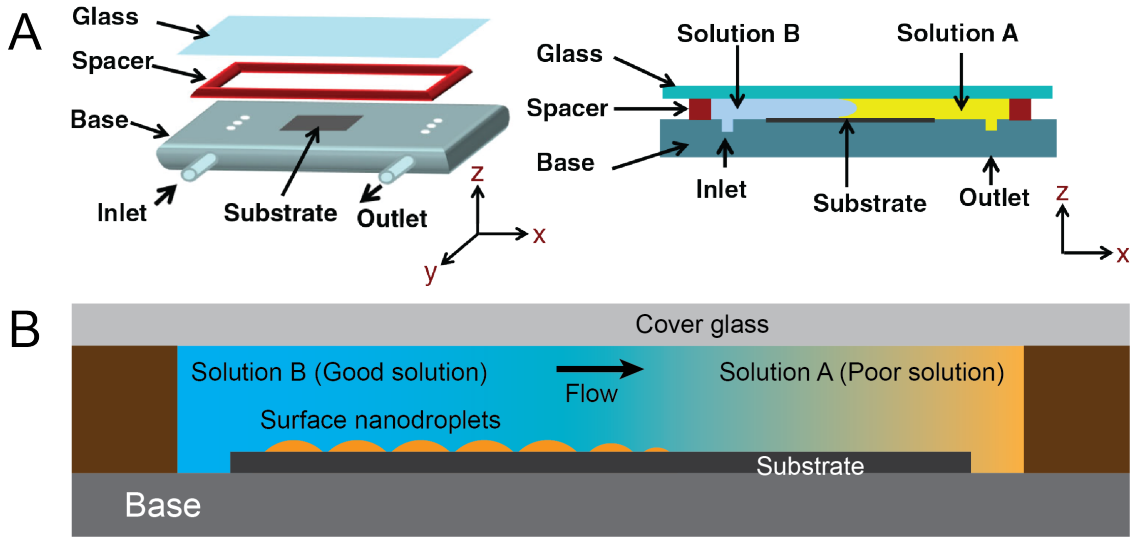

Figure 2.5: (a) Sketches of the fluid channel in which solvent exchange is performed. (B) Droplet formation by the solvent exchange. When the mixing front between the good solvent and poor solvent passes the substrate, surface nanodroplets nucleate and grow. With permissions from [4]. Copyright (2015) American Physical Society

ity, versatility, and well-controlled droplet formation, solvent exchange method was employed throughout our research for the preparation of surface nanodroplets.

2.5.1 Effect from flow rate and flow geometry

The flow rate and flow geometry can cast a significant effect on droplets formation during the solvent exchange. In 2015, Zhang et al. revealed the role of flow rate in the primary mechanism of surface nanodroplets formed by solvent exchange [96]. During the solvent exchange, a pulse of oil oversaturation can be generated in the mixing front by the diffusion between two solvents with the solubility gap of oil. Surface nanodroplets nucleate and grow as the mixing front with oversaturation pulse passes the substrate. The droplet growth can be expressed by the diffusive growth of a spherical model [96]:

$$\dot{m} = 4\pi\rho_{oil}R^2\dot{R} = 4\pi DR^2\partial_c|R. \tag{2.1}$$

D and ρ are respectively diffusion coefficient of ethanol in water and density of oil. $\partial_c|R$ is concentration gradient of oil in the diffusive boundary layer. As the solvent exchange was performed with a laminar flow, the oil transport in the diffusive bound-

ary layer can be determined by a Prandtl–Blasius–Pohlhausen type behaviour, in which the thickness of the diffusive boundary layer λ is given by $\lambda \sim R/\sqrt{Pe}$ [96]. Pe is defined as $Uh/D = Q/wD$, which is a dimensionless number describing the convection of the laminar flow over the diffusion in the boundary layer. U is average velocity. h and w are channel height and channel width.

Concentration gradient of oil in the boundary layer can be calculated as

$$\partial_c|R \sim \frac{c_\infty(t) - c_{s,w}}{c_{s,w}} \sim c_{s,w}\frac{\zeta(t)}{\lambda} \sim c_{s,w}\sqrt{Pe}R^{-1}\zeta(t), \tag{2.2}$$

in which $c_\infty(t)$ is oil concentration, $c_{s,w}$ is oil solubility in poor solvent. Oil oversaturation $\zeta(t)$ is defined as

$$\zeta(t) = \frac{c_\infty(t)}{c_{s,w}} - 1. \tag{2.3}$$

Coupling equations 2.1, 2.2, and 2.3, we obtain

$$R\dot{R} \sim \frac{Dc_{s,w}}{\rho_{oil}}\sqrt{Pe}\zeta(t), \tag{2.4}$$

which can be integrated from 0 to final radius R_f, as

$$R_f \sim (\frac{Dc_{s,w}}{\rho_{oil}}\zeta_{max}\tau Pe^{1/2})^{1/2}. \tag{2.5}$$

Equation 2.5 means that the droplet growth can be determined by maximum oversaturation ζ_{max} and duration τ. In the laminar flow, τ depends on the diffusion time and channel height h, with the scaling law: $\tau \propto h^2/D$. Coupled with equation 2.5, the final droplet volume can be determined by Pe and h as

$$Vol_f \sim R_f^3 \sim h^3(\frac{c_{s,w}}{\rho_{oil}})^{3/2}(\frac{c_{s,e}}{c_{s,w}-1})^{3/2}Pe^{3/4} \tag{2.6}$$

Here $c_{s,e}$ is the oil solubility in ethanol. The scaling law $Vol_f \sim Pe^{3/4}$ from the theoretical model is in good agreement with the experimental results, given that droplet size is flow rate dependent [96].

During the solvent exchange, the duration of droplet growth on the homogeneous substrate scales with $Pe^{-1/2}$, which can be well described by Taylor-Aris dispersion

[101]. Equations 2.1 and 2.2 can be integrated over time as

$$\int_0^{R(t)} R\dot{R} \sim \frac{Dc_{s,w}}{\rho}\sqrt{Pe}\int_\infty^t \zeta(t)dt. \tag{2.7}$$

The oversaturation pulse $\zeta(t)$ was considered as a Gaussian distribution,

$$\zeta(t) = \zeta_{max}e^{-(t-t_0)^2/2\tau^2}. \tag{2.8}$$

The definition of the error function is given as

$$Erf(x) = \frac{2}{\sqrt{\pi}}\int_0^x e^{-y^2}dy. \tag{2.9}$$

From equations 2.7 to 2.9, we obtain

$$(R(t))^2 \sim \frac{Dc_{s,w}}{\rho}\sqrt{Pe}\zeta_{max}\tau Erf(\frac{t-t_0}{\sqrt{2}\tau}) \tag{2.10}$$

In Taylor-Aris dispersion, the concentration profile in the channel enlarges the concentration gradient and thus enhances the radial diffusion of the solute, which smear out the concentration distribution in the flow direction [102–105]. As a result, $\zeta_{max} \sim Pe^{1/2}$ and $\tau \sim h^2Pe^{-1/2}/D$ are expected, suggesting that at a fixed position downstream for large advection velocity the blob of oversaturation will be smeared out less as less time has passed [101, 106]. Consequently, $\zeta_{max}\tau \sim h^2/D$, resulting in

$$(R(t))^2 \sim h^2\frac{c_{s,w}}{\rho}\sqrt{Pe}Erf(\frac{t-t_0}{\sqrt{2}\tau}), \tag{2.11}$$

or in 3 dimension,

$$V(t) \sim R(t)^3 \sim h^3(\frac{c_{s,w}}{\rho})^{3/2}Pe^{3/4}(Erf(\frac{t-t_0}{\sqrt{2}\tau}))^{3/2} \sim V_f(Pe)(Erf(\frac{t-t_0}{\sqrt{2}\tau})^{3/2}, \tag{2.12}$$

in which $V(t)$ and $V_f(Pe)$ respectively are the volume as a function of time, and final volume, respectively.

The influence of the channel height on the droplet formation was further studied by performing solvent exchange in a micro-structure fluid chamber with varied channel height [106]. Droplets were found to be larger at the gap with higher channel height

h. According to the simulation, the larger droplet size was attributed to the change in the local flow profile of the oversaturation pulse in response to channel microstructures with a large h [106].

Gravitation from two solutions can also influence the nucleation and growth of surface nanodroplets during the solvent exchange. By applying solution A and solution B with different densities, a nonsymmetric parabolic profile of the mixing front can be achieved during the solvent exchange, as sketched in Figure 2.6 [107]. The velocity maximum is off-center. Taking the distances to the lower wall and upper wall as αh and $(1-\alpha)h$, respectively. α was found as a function of Archimedes number Ar, which is defined as

$$Ar = \frac{gh^3}{\nu^2}\frac{\Delta\rho}{\rho_A}. \tag{2.13}$$

g is the acceleration of gravity, taken as 9.81 m/s^2. ρ_A and $\Delta\rho$ are the density of solution A and the density difference between two solutions. ν is the kinematic viscosity. The ratio of the total droplet volume on the lower and upper wall is theoretically to be $(\alpha(Ar)/(1-\alpha(Ar)))^3$.

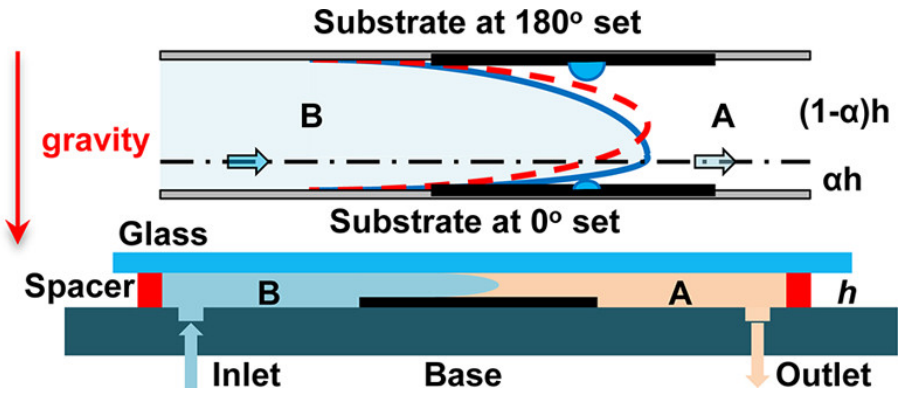

Figure 2.6: Sketch of the nonsymmetric parabolic profile of the mixing front formed by the solvent exchange between two solutions with different densities. (With permissions from [107]. Copyright (2015) American Chemical Society.)

2.5.2 Composition effect and formation of multi-component droplets

Apart from effects from flow conditions and flow geometry, solution composition can cast a great influence on solvent exchange [97, 98]. The influence from solution composition on the solvent exchange are on the variation of c_∞, c_s, and ζ in equations 2.2 and 2.3.

Taking the example of a ternary system with water, cyclohexane, and ethanol, the mixture of ethanol and water with dissolved cyclohexane was taken as the good solution A, while water was taken as the poor solution B. With the increase of initial ethanol concentration in solution A, droplet size increases at first and then decreases, as shown in Figure 2.7A&B [97]. During the solvent exchange, droplets can be either water or oil with the same ternary system, depending on the abundance of oil and water in the mixing front [98]. The effect quantity of poor solvent (water for forming oil droplets, oil for forming water droplets) on the droplet size can be neglected during the solvent exchange [98].

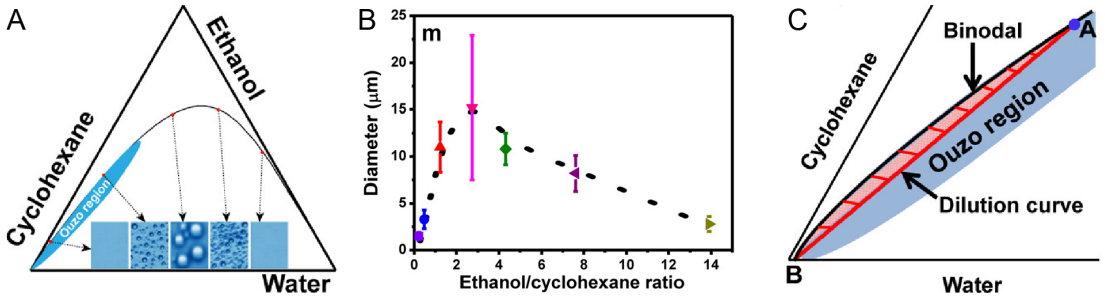

Figure 2.7: (A)&(B) Relationship between the composition of solution A and droplet size. (C) Shaded area representing oversaturation in the mixing front during the solvent exchange. (With permissions from [97]. Copyright (2015) American Chemical Society)

In the ternary diagram, the dilution path linearly links the composition points of solution A and solution B, reflecting the composition profile of the ternary system crossing the mixing front. On the other hand, the binodal line represents the solubility of oil crossing the mixing front. As illustrated in Figure 2.7C, the shaded region

surrounded by the binodal curve and dilution path represent the oversaturation in the mixing front. As the ethanol composition increases in solution A, the dilution path move downwards, reducing the area of the shaded region and thus oversaturation in the mixing front, resulting in droplets of smaller size. For higher ratios of ethanol to water in solution A, a macroscopic phase separation takes place and contributes to an oil-rich sub-phase and a water-rich sub-phase, as the dilution path passes the spinodal line below which the emulsion droplets are unstable [97]. As the concentration of ethanol in solution A increases, more oversaturation in the mixing front will be consumed by forming the oil-rich sub-phase. In this case, oversaturation consumed for forming nanodroplets can only be represented by the area surrounded by the binodal line, spinodal line, and the dilution curve.

Apart from the droplet size in pure surface nanodroplets, the composition of multi-component surface nanodroplets can also be controlled during the solvent exchange. For the formation of multi-component droplets, the ratio of different components in the droplet did not directly correspond to the ratio in the solution. Instead, the composition of droplets correlates to the oversaturation level of each component in the mixing front, which can be reflected by the region surrounded by the dilution curve and binodal line in the ternary phase diagram [108].

2.5.3 Effects from substrates

The morphology of surface nanodroplets is highly sensitive to the polarity of the surrounding solution and the wettability of the surface of the solid substrate. The local wettability of the substrate can be well characterized by surface nanodroplets at the micro-level. Surface nanodroplets growing on a homogeneous substrate by solvent exchange generally take the influence from and even coalescence with neighbouring droplets [96]. As a result of the interaction between droplets, there is a maximum plateau for the surface coverage of nanodroplets formed by solvent exchange, regardless of various conditions [109].

Though the average size of surface nanodroplets on the homogeneous substrate can be well-controlled during the solvent exchange, however, the wide distribution of droplet size limits further research on the mechanisms and applications of surface nanodroplets. To address this problem, highly ordered micro-patterns arrays were prepared by lithography and silanization on the substrate. As sketched in Figure 2.8A, nucleation and growth of surface nanodroplets were constrained on the hydrophobic domains (OTS-Si) pre-patterned on the hydrophilic silica substrate. With the patterns to constrain the droplets, the regulation of droplets size, number density, and the position can be well controlled by hydrophobic patterns with precise morphology, as in Figure 2.8B-D [110, 111]. Different from droplets on the homogeneous substrate growing with a constant contact angle (CA mode), droplets on the pre-patterned substrate grow with a constant radius (CR mode), as the droplet rim is pinned on the rim of the hydrophobic patterns. The droplet growth with a CR mode was governed by

$$\theta_f = G^{-1}(G(\theta_c) + const\frac{D}{L^2}\frac{c_s}{\rho}\zeta_{max}\tau Pe(1-\alpha(L,Pe))), \tag{2.14}$$

in which θ_f is the final contact angle of the droplet [111]. L is the base radius of the patterns or the droplet. $G(\theta)$ is defined as a Gaussian function with the variable of θ. $1-\alpha(L,Pe)$ means the fraction of time for droplets growing in the CR mode.

Surface nanodroplets were also produced on the substrates with spherical cap microstructure, in which droplets grow around the structure [112]. As droplets grow, the number of surface nanodroplets around the cap decreased as a result of coalescence. In the end, droplets finally self-organized into highly symmetric arrangements in the aspects of droplet size, position, and mutual distance. The position of the merged droplet depends more on the large parent droplet. The location of the merged droplets from two neighboring droplets follows a scaling law $\Delta\theta_1/\Delta\theta_2 = r_1/r_2$, in which r_1, r_2, $\Delta\theta_1$, and $\Delta\theta_2$ are radius of two droplets and the angle differences between two un-merged (parent) droplets and the final position of the as-merged droplet, respec-

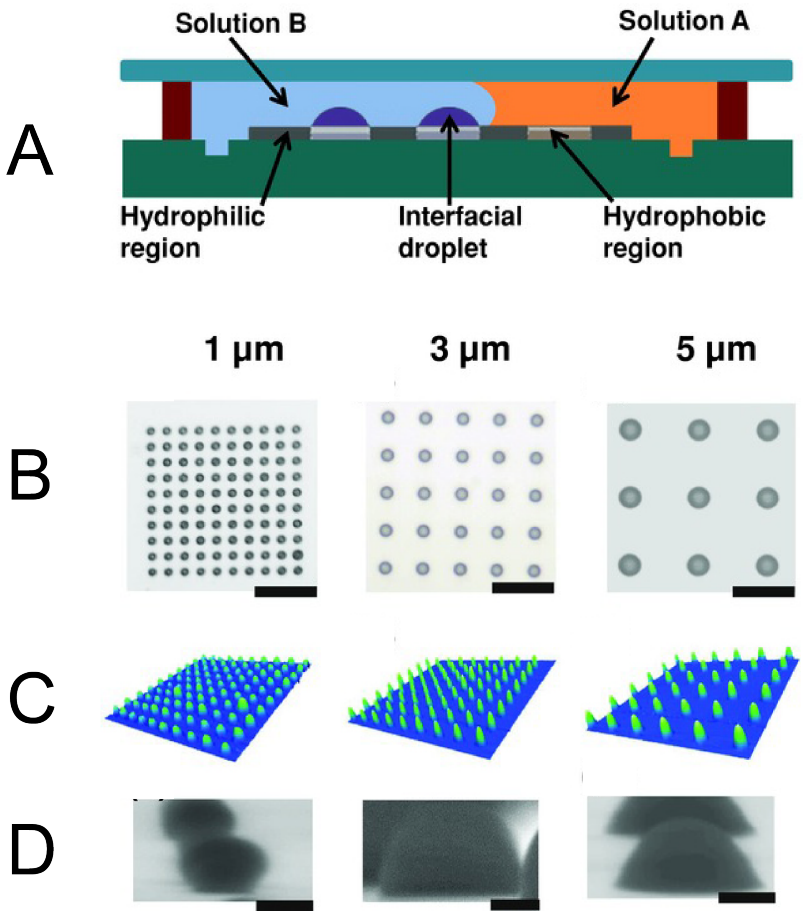

Figure 2.8: (A) Sketch of droplets formed by solvent exchange on the pre-patterned substrate. (B)-(D) Top view (B), profile from atomic force microscope (C), and (D) side view of polymerized surface droplets formed by solvent exchange on pre-patterned substrates with different pattern sizes. (With permissions from [110]. Copyright (2015) Wiley)

tively [113]. The surface nanodroplets were also produced on the curve surface of a micro-fiber[114]. On the wall face of the microfiber, the droplet formation was significantly enhanced compared with the droplet formation on the plane substrate under the same condition.

2.6 Dissolution of surface nanodroplets

As our experiments in Chapters 3&4 involve droplet dissolution when surface nanodroplets react, this section summarizes the mechanisms of dissolving surface nanodroplets for later theoretical analysis. During the dissolution on a homogeneous substrate, surface droplets shrink in a mixed mode consisting of constant contact radius (CR) mode (Figure 2.9A) and constant contact angle (CA) mode (Figure 2.9B), known as the stick-slide mode (Figure 2.9C) with alternate reduction of the contact angle and the base radius [115]. Additionally, the fourth mode named stick-jump mode (Figure 2.9D) was also found during the dissolution of surface nanodroplets, which is more pronounced for microscopic droplets than their macroscopic counterparts. In this mode, the intermittent pinning of the droplet contact line from the surface roughness leads to the switching between sticking and jumping during the dissolution. For droplets growing on pre-patterned hydrophobic domains surrounded by hydrophilic area, droplets dissolved as CR mode when the droplet contact line is pinned on the rim of patterns [110, 111].

Normally smaller droplets tend to dissolve faster in terms of radial shrinkage. However, the specific rate of droplets of the same size may be different, which can be attributed to two factors: i. different pining stress from geometric heterogeneity of the substrate surface; ii. interaction with neighbouring droplets in terms of diffusion out of the droplets. The dissolution of surface nanodroplets is driven by the solubility and the saturation level in the surrounding phase, following the diffusion-driven mechanism derived by Epstein and Plesset. Based on the diffusion equation, Laplace pressure, and Henry's law, the dissolution time t_diss for a droplet dissolve in a CA

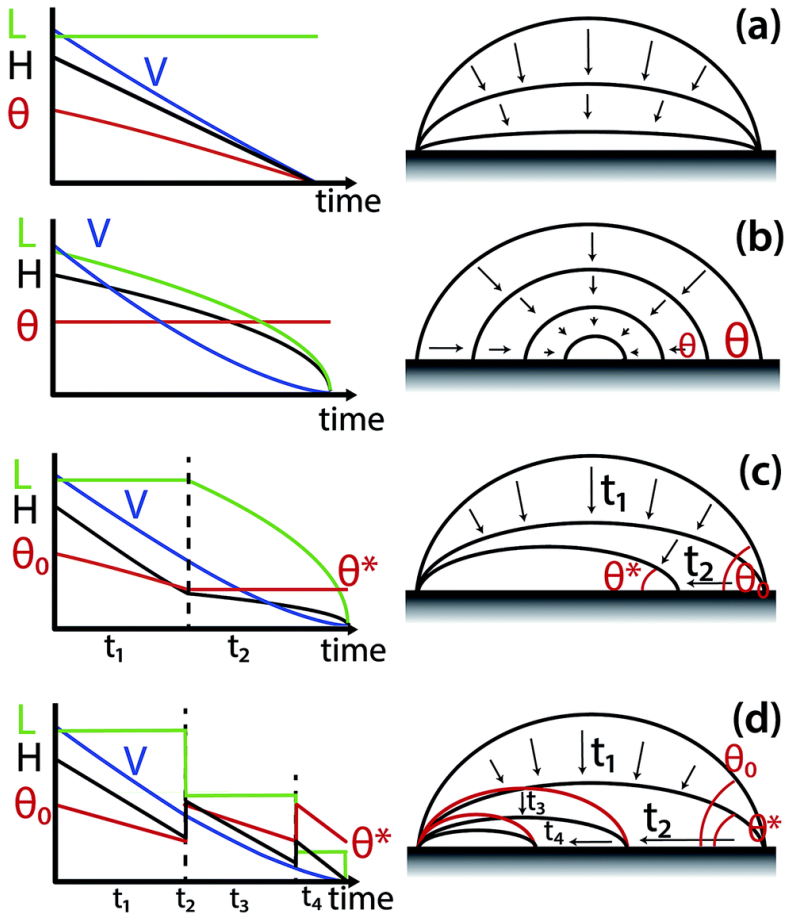

Figure 2.9: Sketch of four dissolution modes of a surface droplet: (A) constant contact radius (CR) mode; (B) constant contact angle (CA) mode; (C) stick-slide mode; (D) stick jump mode. (With permissions from [115]. Copyright (2015) Royal Society of Chemistry)

mode can be evaluated with the following equation:

$$t_{diss} = \frac{L_0^2 \rho}{8D(c_{s,w} - c_\infty)} \frac{3g(\theta)}{f(\theta)} = \tau(L_0) \frac{1}{\zeta} \frac{3g(\theta)}{f(\theta)} \tag{2.15}$$

2.7 Surface nanodroplets for liquid-liquid extraction and chemical sensing

With the advantages of outstanding stability, long lifetime, pinning effect on the substrate, flexible and controllable producing method, surface droplets promise deep potential in extraction and chemical sensing techniques. Compared with DLLME discussed in Section 2.2, the Preparation of surface nanodroplets is fast, green, and versatile, as the solvent exchange method avoids the use of harmful extractants and reduces the consumption of dispersive solvents. Moreover, time-consuming separation techniques such as filtration or centrifugation are not required for liquid-liquid extraction based on surface nanodroplets, as the contact line of surface droplets is pinned on the solid surface.

Extraction by surface nanodroplets combined with surface-enhancement Raman scattering (SERS) was reported for one-step in-situ chemical sensing with high sensitivity [77]. The silver precursor solution was taken as the external flow to react with binary surface nanodroplets of vitamin E and octanol. The silver precursor was reduced to silver nanoparticles at the droplet surface by vitamin E. After the reaction, the aqueous solution of the analyte was then injected into the system and extracted by the surface nanodroplets. Analyzed by the Raman spectrometer, the limit of detection (LOD) was confirmed down to 10^{-9} M with a quantitative range from 10^{-6} M to 10^{-9} M, simplifying the multiple steps from the traditional DLLME.

The interface of surface nanodroplets can also be taken as the protective barrier for droplets to extract analytes from suspensions. On the hydrophobic inner wall of a narrow capillary tube, surface nanodroplets were produced to extract the model compound (Nile red) from a simulated oil sand wastewater [80]. The Nile red in the

droplets was detected by a fluorescence microscope. The LOD can reach $10^{-}8$ M with a linear range from $10^{-}6$ M to $10^{-}8$ M, providing a green and feasible extraction method in severe environmental conditions. Additionally, surface nanodroplets were also reported in the extraction enhancement for encapsulated droplets and the determination of partition coefficient [78, 116].

However, although the surface nanodroplets were confirmed to be highly efficient for liquid-liquid extraction, the fact that they are pinned on a substrate and that the volume of each nanodroplet is on the femtoliter scale make the collection of these nanodroplets extremely challenging by conventional methods such as centrifugation. While in situ methods such as surface-enhanced Raman spectroscopy (SERS) or optical microscopy can be employed for analysis during extraction, a method to collect the droplets would greatly expand the applicability of surface nanodroplet-based extraction method as it would enable the use of offline analytical techniques such as GC-MS, HPLC, UV-Vis, and others. To expand the versatility of the method, in Chapter 6, the droplet extraction was performed in and collected from a 3-meter Teflon capillary tube.

2.8 Summarization of identified knowledge gaps from literature review

From the literature review above in Chapter 2, multiple knowledge gaps were identified as below:

1. The quantitative understanding of effects from external flow conditions and interactions between droplets on the kinetics of droplet reaction and mass transfer is missing. The knowledge gap will be addressed in Chapter 3.

2. The quantitative understanding of effects from droplet size, droplet composition on the kinetics of droplet reaction and mass transfer is missing. The knowledge gap will be addressed in Chapters 4&5.

3. Due to the extremely small volume and the pinning effect, the extraction and

chemical detection based on surface nanodroplets were limited to only a few in-situ analytical techniques, such as SERS and fluorescence microscopy with limited model compounds. The methodology developed in Chapter 6 expands the versatility of the extraction based on surface nanodroplets by collecting droplets for multiple offline analytical tools.

Chapter 3

Speeding up biphasic reactions with surface nanodroplets

3.1 Introduction

Small-size droplets are omnipresent in nature and technology, including lab-on-chip, emulsions, aerosols, sneezing and coughing, cell metabolism compartments, heterogeneous catalysis, polymer synthesis, micro-extraction, among many others [4–11]. At present, 'on-droplet' chemistry attracts increasing research attention [12]. Chemical reactions compartmentalized in small-size droplets can potentially be highly efficient with large throughputs due to their high surface area-to-volume ratio and their discrete nature [13, 117–119]. Noticeably, the kinetics of chemical reactions on the droplet surface can be significantly enhanced [120]. For instance, chemical reactions in aerosol droplets are accelerated, in some cases even by a factor of 10^6 compared to their bulk counterparts [20, 121]. Acceleration can also be found in a diverse range of biphasic reactions in confinement that involves two immiscible fluids, such as in micro-sized emulsion droplets, thin liquid films, inverted micelles or at the surface of aerosol particles [122–124]. Apart from the reaction kinetics, the intermediates or products from droplet reactions can also be different from those from the counterparts in bulk [125]. Some reactions that are impossible without catalysts in the bulk can take place spontaneously in droplets. For example, Nam et al. demonstrated that phosphorylation of sugars occurred spontaneously in aqueous microdroplets [22]. The

shifted balance and accelerated kinetics of reactions in small droplets may demonstrate a plausible route to the production of complex biomolecules outside of living systems [29]. Reactions confined in small droplets have been proposed to explain how synthetic reaction for complex biomolecules that are thermodynamically unfavorable in aqueous bulk could occur in the origin of life on early earth [25, 26].

The mechanisms for reaction acceleration in droplets are still unclear so far. Two possible explanations are proposed in the literature. (1) In case of flying droplets in air created from electrospraying, the solvent in the droplet may evaporate, leading to rapid shrinkage in droplets size and the increase in the concentration of reagents inside droplets. In addition, reagent diffusion is quick in small size droplets, which may contribute to the enhanced reaction kinetics [20, 126]. (2) Another important effect may be from the large surface area-to-volume ratio of droplets, compared to larger drops or the bulk liquid. Nakatani and co-workers found that electron transfer was accelerated at droplet surface [30–32]. Furthermore, Fallah-Araghi et al [29]. demonstrated that the reaction rate is inversely proportional to the droplet radius, related to the preference of product adsorption and desorption at the droplet interface that accelerates the rate and shifts the balance of the chemical reaction [29]. The active energy barrier was found to be negligible for the reactions within droplets, possibly due to the molecular configuration of reactants at the droplet surface [22].

How to distinguish between the relevance of these two suggested mechanisms? Immersed surface nanodroplets provide a unique platform for studying reaction kinetics under well-controlled conditions, eliminating the influence from concentrating effects due to solvent evaporation though one has dissolution effect. These droplets have a maximal thickness from several to several hundred nanometers (namely nanodroplets) and a volume typically on the order of femto- or atto- liters, located on the solid surface in contact with a bulk liquid that is immiscible with the droplet liquid [4]. The size distribution and the number density of surface nanodroplets can be well controlled by solution composition and flow condition during a simple process of solvent

exchange [96, 98]. The droplet morphology can be tailored by the properties and patterns of the substrates [112, 127]. The long term stability of surface nanodroplets due to their poor solubility enables us to track the reaction kinetics in-situ with sufficient temporal and spatial resolution.

In this work, we investigate the rate of biphasic reactions between surface nanodroplets and the reactant solution in an external flow. In our model systems, acidic droplets react with basic solution in the flow. The product from the reactions is surface active, carried away by the surrounding flow after desorption from the reacting droplets. The combined effects from the reaction and the mass loss of the product lead to the shrinkage of surface nanodroplets. The objective of this study is to improve the understanding of the chemical kinetics on the surfaces of small-sized droplets. The findings will be valuable to guide the design of droplet-based reactions in flows for heterogeneous catalysis, micro-extraction and other applications.

3.2 Methodology

3.2.1 Chemicals and materials

Oleic acid (90%, Fisher Scientific), ethanol (90%, Fisher Scientific), octyldecyltrichlorosilane (OTS) (95% Fisher Scientific) were used as received without further purification. Water was from Milli-Q (18.2 MΩ). Silicon substrates were hydrophobilized with OTS, prepared by following a procedure reported previously [128]. The OTS-coated substrates were cleaned by sonication in ethanol for 10 min and dried in a stream of air before use.

Oleic acid (OA) was chosen as the droplet liquid. To perform the solvent exchange, two solutions were prepared. The first solution (solution A) was 2.4% (v/v) oleic acid in the mixture of ethanol and water, where the ratio was 6.5:3.5. The second solution (solution B) was water. To trigger the chemical reaction of oleic droplets, solution C (sodium hydroxide aqueous solution) was also prepared.

3.2.2 Formation of droplets

The solvent exchange was used to prepare reactive oil droplets of oleic acid. Solution A introduced inside a house-made fluid chamber was replaced by solution B. The design and components of the fluid chamber are shown in Figure 3.1(a). The height of the chamber (the distance between the substrate and the cover glass) was 0.4 mm, the width of the chamber was 15 mm and the length of the substrate was 25 mm in all experiments. The solvent exchange was performed at 21°C. The injection of solution B was controlled at 500 μL/min in terms of volume flow rate, to keep droplets formed with consistent number density and size distribution. The initial surface coverage, the ratio of the substrate's surface area taken up by OA droplets after the solvent exchange, was fixed about $\approx 4\%$ for all groups of experiments.

3.2.3 Chemical reaction

After formation of nanodroplets by the solvent exchange, solution C was introduced into the fluid chamber to initiate the reaction, as sketched in Fig. 3.1(b). The schematic drawing of the reaction process in a single droplet is shown in Fig. 3.1(c). Owning to the hydrophilic property, hydrophilic carboxyl groups of oleic acid at the interface tend to stay at the water side. At the same time, hydroxide ions from the bulk are convected to the droplet interface by the flow, attack carboxyl groups in the water side and convert the acid to oleate. Due to its high surface activity, oleate stays at the interface, and in a long term, gradually dissolves into the aqueous phase and removed by the flow.

3.2.4 Parameter space for experiments

We conducted the experiments at different flow rate Q controlled by a syringe pump. Q is the volume flow rate of the alkaline flow. The dimensionless Peclet number for the product (Pe) is defined as

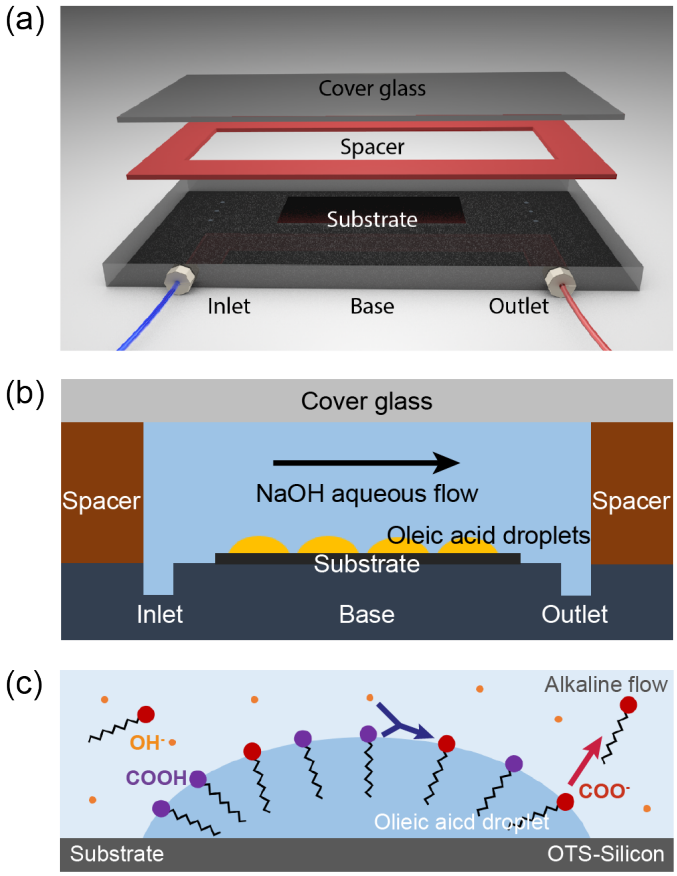

Figure 3.1: Schematics of the experimental set-up: (a) A fluid chamber for solvent exchange and droplets reaction. The chamber consists of a top cover glass, a spacer, and a base with inlet and outlet. The hydrophobic substrate was attached to the base. The height of the fluid chamber was adjusted by the thickness of the spacer. (b) The experimental set-up. Oleic acid (OA) droplets on the substrate were formed by solvent exchange, and the alkaline solution was introduced from the inlet. NaOH reacts with the –COOH group of oleic acid at the droplet surface. (c) An oleic droplet with a base radius R reacting with the alkaline flow. The –COOH group (purple head group in the sketch) reacts with OH^-(orange circle) in the alkaline flow, forming a $–COO^-$ group (red dot). The reactant and the product have the same hydrophobic tail (black chain). The blue arrow indicates the reaction. The product oleate desorbs from the droplet surface, transported away by the flow as indicated by the red arrow.

$$Pe = \frac{\bar{U}h}{D} = \frac{Q}{wD} \tag{3.1}$$

where D, $\bar{U}$, h and w are respectively the diffusion constant of oleic acid, the average linear flow rate, the channel height (400 μm) and the channel width (130 mm). To study the effect from the flow rate, the concentration of NaOH in the solution $c_{re,bulk}$ was fixed at 4.0×10^{-4}M while Pe varied from 5 to 198. The time required for the solution to reach the same region of the surface at different flow rate was predetermined in experiments by flowing the solution inside an empty fluid cell at the same flow rate.

To investigate the concentration effect, we kept the Pe number constant at 31, while the concentration of NaOH ($c_{re,bulk}$) in the solution varied from 1.0×10^{-4} M to 0.1 M.

3.2.5 Characterization of droplet size

Reaction processes were recorded *in-situ* by an upright microscope with video camera (Nikon, 10x objective lens, 0.24 μm/pixel, 15.0 fps). White-light LED was applied to trace the surface of the substrate by bright field imaging. The filmed images were processed by ImageJ and analyzed frame-by-frame by self-written Matlab codes. Based on the binarized images, the surface coverage SC, the base radius R with time, and the characteristic lifetime τ are determined. Surface coverage of the droplets on the substrate was analyzed over an area of 0.34 mm^2 with around 2000 droplets.

3.3 Results and discussion

3.3.1 Dependence of droplet reaction rate on Pe

In order to obtain consistent initial droplet conditions, all experiments were conducted from similar surface coverage ($\sim$ 4%) of droplets on the substrate with averaged droplets radius of ~ 1.2 μm. Seven series of snapshots in Figure 3.2 reveals progressive

shrinkage of reacting droplets from reacting with the alkaline flow at different flow rates. The time at the start of the reaction (t_0) shown in the first image of each row was defined as the moment when the flow of the solution enters the field of the view. Figure 3.2 (h) shows the probability distribution functions (PDF) at varying Peclet numbers. Results provided in plots suggest that initial droplet size distributions are highly consistent in the reactions with the basic solution supplied at different flow rates. Therefore any effect from different surface-to-volume ratios of the droplets on the reaction kinetic is expected to be same in all experiments.

Starting from t_0, droplets became darker in several seconds, which is seen by comparing images in the first and the second columns in Figure 3.2. The darker color of the droplets was possibly due to the formation of the product that is surface active. Thus the shape of droplets may change and appear darker in images. In other words, the droplets were possibly covered by the product from the reaction.

After a period of time from the arrival of the alkaline solution, droplets started to shrink with a noticeable rate and eventually disappeared from the surface. The droplets dissolved faster as the Peclet number of the solution Pe increases. In the two most apparent cases in Figure 3.2(a)&(g), at $Pe = 198$ the droplets completely dissolved in 85 seconds t, but dissolution takes 6 hours at $Pe = 5$. As comparison, droplets had not shrunk after 8 hrs under a continuous flow of pure water at 6 ml/h, showing that droplet shrinkage was not due to the dissolution of the droplet liquid, but due to the loss of the product from the chemical reaction. These results clearly demonstrate that the flow rate of the reactant solution has a significant impact on the rate of droplet reaction.

The quantitative analysis is shown in Fig. 3.3(a) where the temporal surface coverage (normalized by surface coverage at t_0) is plotted as function of the Pe number of the alkaline flow. A general feature is that there were two stages in the droplet dissolution after the arrival of the reacting solution in the flow. At an initial stage, the surface coverage and the droplet sizes did not experience significant shrinkage and

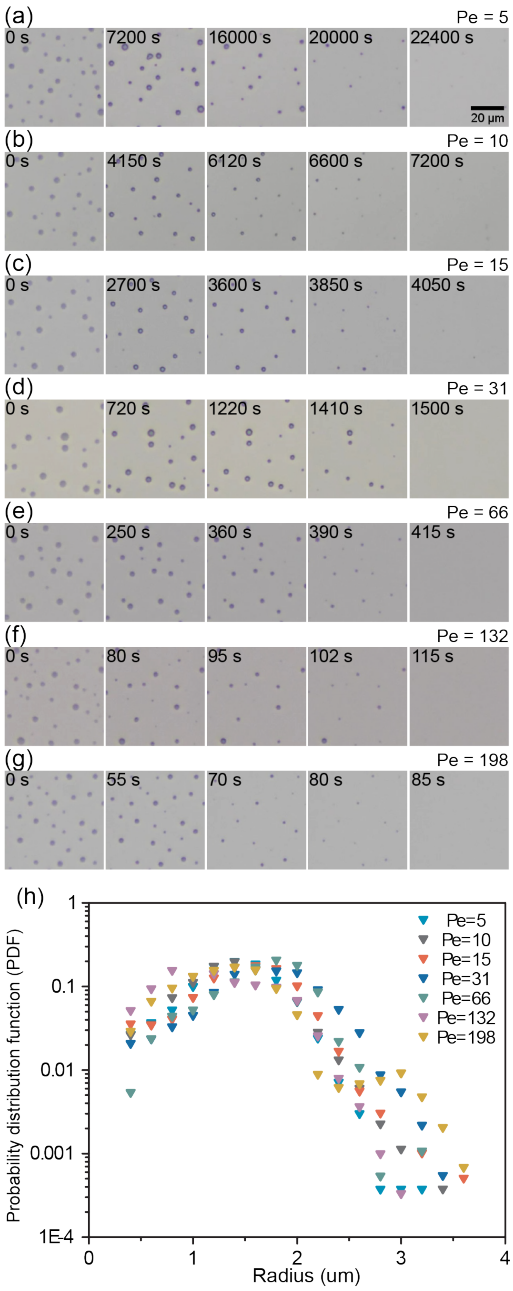

Figure 3.2: Optical images of reacting nanodroplets with alkaline solution of different flow rates. The frame rates of the videos are 15 fps, and the spatial resolution is 0.24 μm /pixel. The concentration of NaOH in each group was controlled at 4.0×10^{-4} M. The flow rates from (a) to (g) were respectively 17, 33, 50, 100, 215, 430 and 645 μL/min (corresponding Peclet numbers (Pe=Q/(wD)) thus were 5 to 198). The droplets in all images were produced by solvent exchange with exactly same flow and solution conditions to make initial droplets with consistent size and number density. (h) Probability distribution functions (PDF) of initial droplet sizes at different flow rates. Data shown are from droplets with the measured radius larger than 0.3 μm due to the spatial resolution.

showed somewhat flat responses with time. At the second stage, the droplets started to shrink with an increasing shrinkage rate. The higher Pe of the alkaline solution was, the earlier the surface coverage of the droplets started to decrease. The droplets continuously dissolved till they disappeared. We note that a single exponential decay function cannot completely fit the curve of droplet dissolution. Especially at the late stage of dissolution, the slope of our experimental data is much faster than that of the fitting line generated by a single exponential decay function (Fig. S1). The reason is that droplet reactions take place in a background with product concentration varying with time, which will be analyzed and explained in detail later in §3.3.4.

Here we compare the difference in droplet lifetime for different Pe numbers, measured by the shrinking rate in surface coverage (Figure 3.3(b)). The colors of markers correspond to that in Figure 3.3(a).

The lifetime of droplets τ here is defined as the time from the start of the reaction t_0 to the moment when surface coverage SC decreases to 10 % of the initial surface coverage, SC_0. Remarkably, all the data collapse into a single universal curve with a best fitting effective scaling exponent of -1.60, as indicated by the solid black line in the plot. Note that the slope resulting from scaling analysis (slope$=-3/2$, presented later in §3.3.2) is also shown in the plot. We also tried to analyze half of the original region (around 1000 droplets) and the analysis of fewer droplets can still yield consistent results (Fig. S2).

In addition to the surface coverage, the lateral sizes R of individual droplets were also analyzed, namely its dependence on Pe. The initial radii R_0 of these droplets were all around 2.1 μm. We analyzed the lifetime of individual droplets τ, as shown in Fig. 3.3(c). Consistent with the two-stage reaction, as highlighted in Figure 3.3(a), individual droplets also exhibit the feature of two-stage dissolution. The lifetime of individual droplets is shorter when the reacting solution is supplied at a faster flow rate. Here τ is the duration from the droplet in contact with the solution to the end of droplet dissolution.

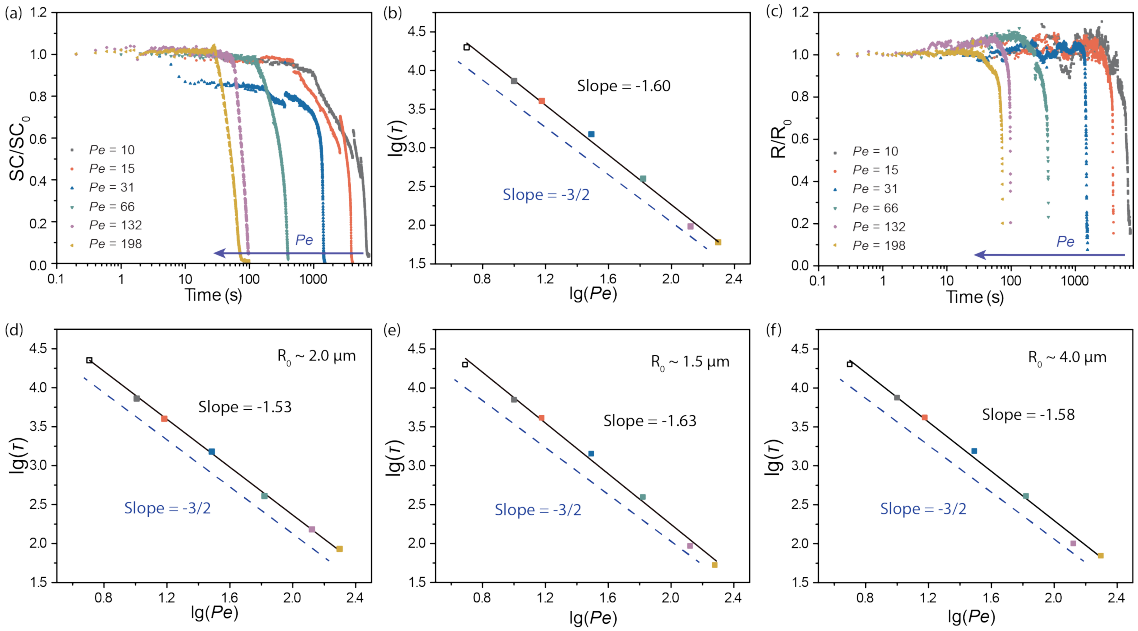

Figure 3.3: (a) Normalized surface coverage as function of time for droplet reaction at different flow rates. SC: surface coverage; SC_0: initial surface coverage. (b) Droplet lifetime τ as function of Peclet number. τ on the x-axis is the time required for SC/SC_0 to reach 0.1. (c) Normalized lateral radius as function of time for individual reacting droplets at different flow rates. Droplets presented here all have a similar initial size ($\sim$ 2.1 μm) and located at a similar location on the substrate. As the optical resolution of the microscope was 0.24 μm/pixel, the droplets once smaller than 0.24 μm in lateral diameters cannot be resolved. (d)$-$(f) Droplet lifetime τ based on the droplet radius as function of Peclet number. The initial radii of droplets in (d), (e), and (f) were around 2.1, 1.5, and 4.0 μm, respectively. The initial τ is the time required for R/R_0 to reach 0.1. The data in (a) and in (c) were obtained from the analysis of the images (b)$-$(g) in Fig.3.2 and data in (b) and in (d)$-$(f) were from (a)$-$(g) in Fig.3.2. The black lines in (b) and (d)$-$(f) were obtained by fitting the experimental data, while the blue dashed lines represent the result $\tau \propto Pe^{-3/2}$ from the scaling analysis.

Fig. 3.3(d) quantitatively shows the droplets lifetime τ of individual droplets as function of the Pe number. An effective scaling law of $\tau \propto Pe^{-1.53}$ was found from the individual droplets, which fairly agrees with that found from the overall surface coverage (Figure 3.3(b)).

To support that the results are unaffected by the droplet size, the lifetime of two additional groups of droplets were also analyzed at different Pe. The initial radii R_0 of droplets in these two groups were around 1.5 μm and 4.0 μm respectively. The effective scaling laws yield by these two groups were $Pe^{-1.63}$ and $Pe^{-1.58}$ (Fig. 3.3(e)&(f)), consistent with results in the 2.0 μm initial radii group. Results from droplets with other initial sizes are shown in Fig. S3.

3.3.2 Dependence of droplet reaction on NaOH concentration

It is expected that the droplet dissolution rate is influenced by the concentration of the reacting solution. At identical flow conditions, we examined droplet reaction rates as the concentration of the alkaline solution was varied over three orders of magnitudes.

Figure 3.4 displays microscopic images of oleic acid droplets dissolving in alkaline flow with different sodium hydroxide concentration. The difference in the lifetime of droplets shown in each row in Figure 3.4 demonstrates that the droplets dissolve faster at a higher concentration of the alkaline solution. The lifetime τ drops from $\sim$4400 seconds for 10^{-4}M NaOH concentration (Figure 3.4(a)) to nearly 7 seconds for 0.1M NaOH concentration (Figure 3.4(g)). Figure 3.4 (h) demonstrates the probability distribution functions (PDF) at varying NaOH concentrations. Results provided in plots suggest that initial droplet size distributions are highly consistent in the reactions at different NaOH concentrations.

We noticed that for high NaOH concentrations, some residues were found at the end of the reaction (last column in Figure 3.4(e)$\sim$(g)). The residues with irregular

shapes may be the product that did not dissolve into the alkaline flow immediately after the chemical reaction. At higher NaOH concentrations, the chemical reaction is very fast, and thus the local concentration of the product near the droplets becomes higher. The product cannot be transported by the flow immediately, resulting in residues left on the substrate.

We now want to quantitatively obtain the dependence of the droplet lifetime τ on the concentration of the alkaline solution. Therefore, similar to our above analysis for the effects from the flow rate, the normalized surface coverage SC/SC_0 as function of time is presented in Figure 3.5(a). Again, there is always a two-stage decrease in droplet surface coverage: not much change at the beginning and then a sudden decrease after a certain transition. The first stage of the droplet reaction is the shortest as the reactant concentration of the flow is the highest.

Fig. 3.5(b) shows the effective scaling relationship between the droplet lifetime and reactant concentration in the flow quantitatively. The lifetime of the droplets effectively scales as $\tau \propto {c_{rc,bulk}}^{-1}$. The exponent of -1.0 fits the dissolution rate of the droplet radius as function of the concentration of alkaline over three orders of magnitude ($0.1\text{M}-10^{-4}\text{M}$).

3.3.3 Scaling analysis of droplet reaction with the flow

In this subsection, we focus on the theoretical analysis of the coupled effects from the flow and the reactant concentration on the reaction rate of surface nanodroplets. We consider that the overall process of the droplet dissolution consists of four sub-steps: (i) mass transport of the reagent (alkali) in the flow, (ii) chemical neutralization at the droplet surface, (iii) desorption of the product from the droplet surface, and (iv) the transport of the product in the flow. The reaction equation is given as

$$\begin{aligned} &CH_3(CH_2)_7CHCH(CH_2)_7COOH + OH^- \\ &\rightleftharpoons CH_3(CH_2)_7CHCH(CH_2)_7COO^- + H_2O. \end{aligned} \tag{3.2}$$

In the droplet, the concentration of the acid is 100% (i.e. pure oleic acid). The alkali

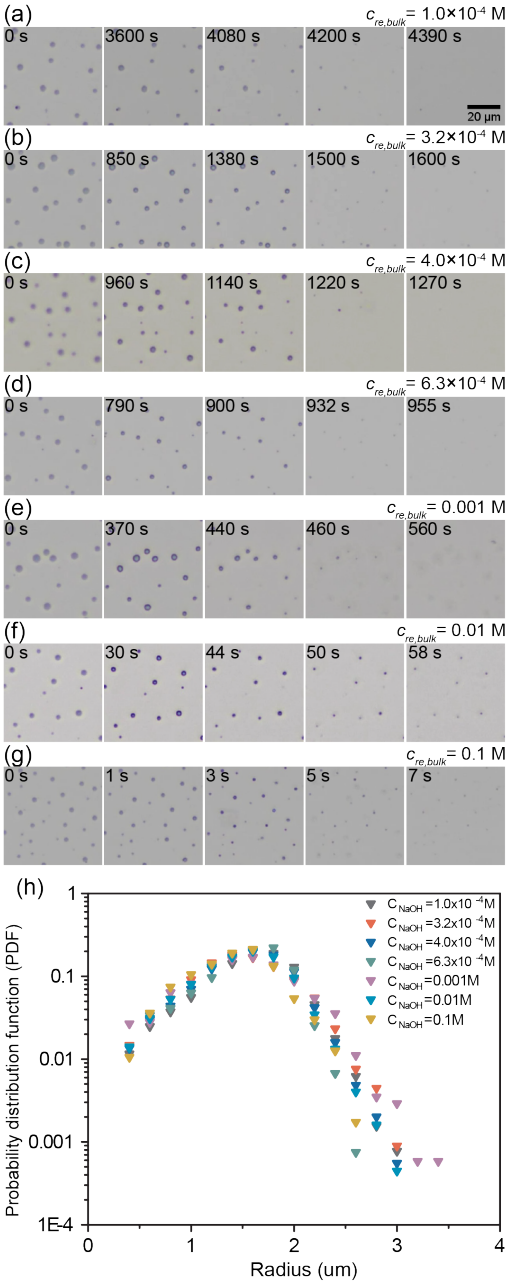

Figure 3.4: Optical images of surface nanodroplets reacting with the alkaline solution of different concentrations. The frame rate of videos was 15 fps, and the resolution was 0.24 μm /pixel. The flow rate for all groups from (a-g) was same, controlled at 100 μL/min (Pe=31). The concentration of alkaline in the solution $C_{re,bulk}$ was 1.0×10^{-4}M (a), 3.2×10^{-4}M (b), 4.0×10^{-4}M (c), 6.3×10^{-4}M (d), 0.001M (e), 0.01M (f), and 0.1M (g). (h) Probability distribution functions (PDF) of initial droplet sizes at different NaOH concentrations. Data shown are from droplets with the measured radius larger than 0.3 μm.

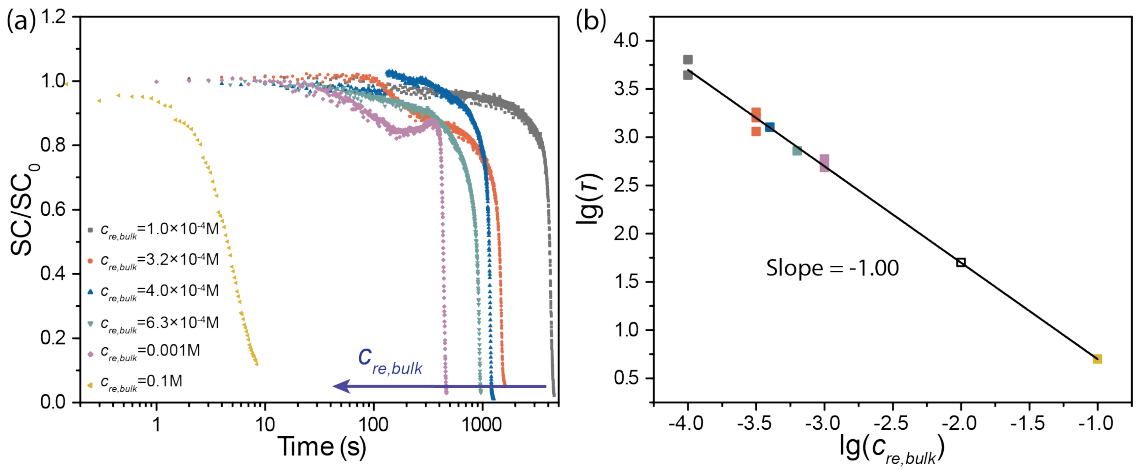

Figure 3.5: (a) Normalized surface coverage as function of time for droplets reacting with the alkaline solution of different concentrations. SC: surface coverage; SC_0: initial surface coverage. Data in (a) was obtained from the analysis of the images in (a)−(g) in Fig. 3.4 (b) Droplet lifetime τ as function of alkaline concentration. τ on x-axis is the time required for SC/SC_0 to reach 0.1. Multiple data points for one concentration are the repeating experiments with initial surface coverage in a small range of variation ($3\% \sim 6\%$).

in the flow must reach the droplet surface to react. The amount of reactants supplied by the flow to the droplet surface per unit time is proportional to the Pe number of the reacting flow and the concentration of the reactant in the bulk. Meanwhile, the depletion of alkali, which results from the reaction in the boundary layer adjacent to the droplet surface, can be immediately replenished by the influx from the flow due to the abundance of alkali in the flow.

For given time, as the neutralization is a fast reaction, we assume that the concentration ratio of the free acid and the product reaches the dynamic equilibrium immediately. The product concentration at interface $c_{pr,sur}$ is governed by the kinetics of the neutralization between oleic acid and sodium hydroxide.

$$c_{pr,sur} \sim K_r c_{re,sur}. \tag{3.3}$$

K_r is the equilibrium constant of the forward chemical reaction (2), which is determined by the Gibbs free energy of the chemical reaction with the droplets, in-

dependent of Peclet number and reactant concentration. In the range of reactant concentration for all our experiments, the droplet surface can be fully converted to the product when the reaction takes place in a fixed environment without the flow [129]. However, under the flow condition, the product concentration at the interface $c_{pr,sur}$ is dependent on Peclet number, as the product is removed from the surface constantly by the flow.

We consider a simple mode in the analysis of a droplet with the shape of a spherical cap, assuming the droplet dissolves in a constant contact angle, same as the situation of dissolving nanodroplets in a flow reported in the literature [96, 127]. The mass loss rate $\dot{m}_{pr}$ of the product from the droplet is given by the product concentration gradient $\partial_r c_{pr}|_R$ at the interface,

$$\dot{m}_{pr} \propto \rho R^2 \dot{R} \propto D R^2 \partial_r c_{pr}|_R, \tag{3.4}$$

where R and ρ are respectively the droplet radius and the density.

The concentration gradient at the droplet surface $\partial_r c_{pr}|_R$ can be estimated from the product concentration difference between the oleate concentration in the flow $c_{pr,\infty}$ and at the interface $c_{pr,sur}$ and the thickness λ of the concentration boundary layer. Assuming the product concentration in the flow is negligibly small ($c_{pr,\infty} \approx 0$), we then obtain

$$\partial_r c_{pr}|_{r=R} \sim \frac{c_{pr,sur} - c_{pr,\infty}}{\lambda} \sim \frac{c_{pr,sur}}{\lambda}. \tag{3.5}$$

Here the diffusive boundary layer of the product is assumed to be of Prandtl-Blasius-Pohlhausen-type for laminar flow, namely

$$\lambda \sim \frac{R}{\sqrt{Pe}}. \tag{3.6}$$

From equations 3.4, 3.5, and 3.6, we obtain

$$\rho R\dot{R} \sim D\sqrt{Pe}c_{pr,sur}. \tag{3.7}$$

From here we immediately deduce the scaling of the life time τ of a droplet of radius R_0, namely

$$\tau \propto \frac{R_0^2}{D}\frac{\rho_o}{c_{pr,sur}}Pe^{-1/2}. \tag{3.8}$$

Now the concentration of the product on the surface linearly depends on the supply rate of reactant by the flow, i.e. on Pe.

$$c_{pr,sur} \propto PeK_r c_{re,bulk}. \tag{3.9}$$

Coupling equations 3.8 and 3.9 leads the scaling law for the lifetime of droplets as function of the Pe number and the concentration of the alkaline flow $C_{re,bulk}$ as

$$\tau \propto Pe^{-3/2}(K_r c_{re,bulk})^{-1}. \tag{3.10}$$

3.3.4 Postponed reactions of downstream droplets

Oleates produced by chemical reaction upstream can be transported along the flow to downstream droplets. However, as the product is surface active, their adsorption on the surface of pristine droplets may influence the reaction of droplets along the path of the flow that is doped with the product. Here we examine the effect of the product from the upstream droplet reaction on the reaction with downstream droplets. While we reported the dissolution rate by comparing the change of the overall surface coverage in time, it is worth to note that the dissolution of droplets propagates along the flow direction. Figure 3.6(a) shows a snapshot taken from the video ($Pe = 31$, $c_{re,bulk} = 4 \times 10^{-4}$M). The whole snapshot was divided into several regions. Two of these regions were defined as 'upstream region' and 'downstream region', respectively. Although the droplets in the upstream (blue) region have fully disappeared, those in the downstream (brown) region still remain intact.

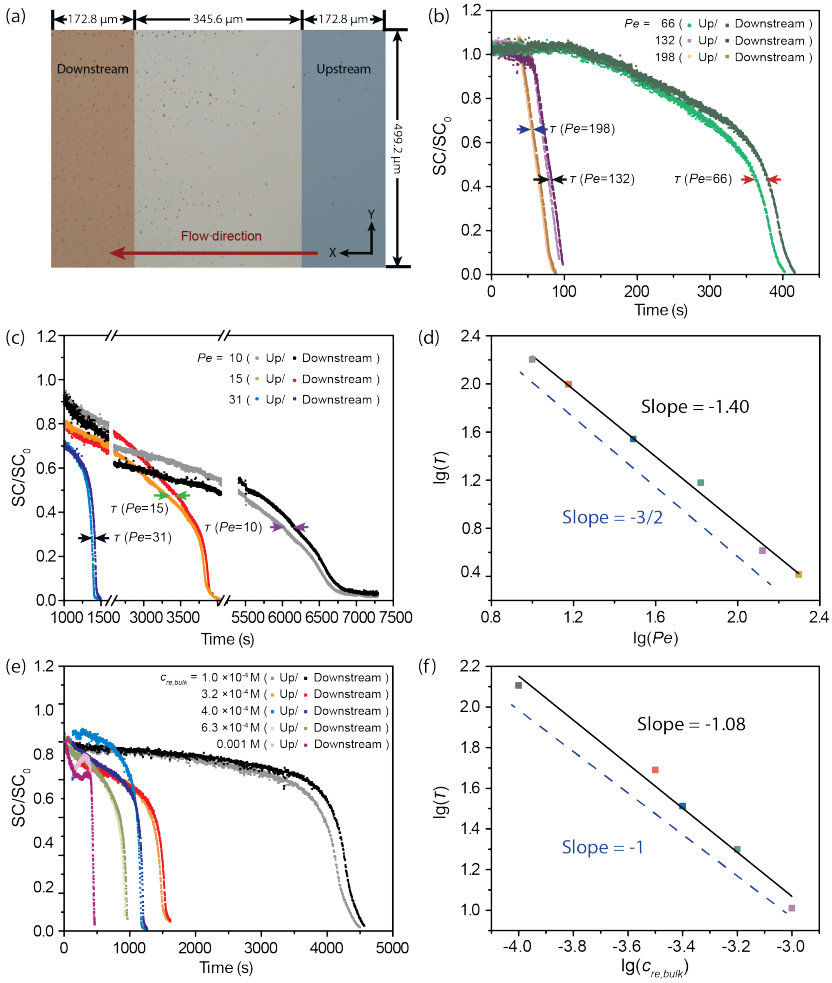

Figure 3.6: (a) An optical image showing the delayed downstream reaction, taken from the same experiment as Fig. 3.2(d), at $t = 1240s$ (Pe=31, $c_{re,bulk} = 4.0 \times 10^{-4}$M). The red arrow indicates the direction of the alkaline flow in X direction. The distance between the defined upstream region (blue shaded) and the downstream region (orange shaded) is 345.6 μm. Both regions span 172.8 μm along X direction. The width of the field of view is 499.2 μm. (b) and (c): the surface coverage normalized by its initial value (SC/SC_0) as function of time for different Peclet numbers in upstream (darker plots) and downstream (brighter plots) regions. The arrows indicate the measured delayed time τ for each flow rate between upstream and downstream. τ is the average time difference between upstream and downstream for the normalized surface coverage SC/SC_0 to reach 0.2, 0.3, 0.4, 0.5 and 0.6. (d) τ as function of Peclet number. The black line was obtained by fitting the experimental data, while the blue dashed line was derived from the scaling analysis. (e) Normalized surface coverage (SC/SC_0) in upstream (darker symbols) and downstream (brighter symbols) regions as function of time at different alkaline concentrations. (f) τ as function of the alkaline concentration. The black line was obtained by fitting the experimental data, while the blue dashed line is from the scaling analysis.

It is remarkable that the product from the upstream region can completely inhibit the reaction of droplets in the downstream region. A possible explanation for the inhibition effect is that the product from the droplet reaction that happened upstream is transported to the surface of the droplets located downstream. Owning to the high surface activity, the product in the flow readily adsorbs onto the droplet surface downstream, and inhibit the reaction and stabilize the coated droplets. After the upstream droplets were depleted, there is no more continuous supply of the product from the upstream region. The product attached to the downstream droplets then is gradually flushed away with the fresh flow. The acid in the droplet becomes exposed to the alkali in the flow, initiated the shrinkage of the droplet from the reactions downstream. In this way, the droplets on the substrate progressively react with the alkali in the flow and dissolve gradually along the flow direction.

Since the product concentration influences the the surface coverage of the reactant on the droplet surface and consequently the reaction rate, we are not able to obtain the kinetic constant based on the initial concentration of the reactant with product concentration varying with time. For the same reason, we cannot calculate the Damkohler number (Da), a dimensionless number relating the chemical reaction timescale to the mass transport. However, the strong influence of the flow rate on the lifetime of the droplets suggests that Da is larger than 1 under all of our flow rates. That is, the rate-limiting step is not the reaction rate but mass transport.

Fig. 3.6(b) and (c) compares how the normalized surface coverage (normalized by initial surface coverage) evolves upstream and downstream under different flow rates (the life time τ starts when the alkaline flow reaches the observed region). The gap between the upstream and downstream dissolution curves represents the timescale of the delay. The delay is shorter for the higher flow rate. Fig. 3.6(d) shows the scaling relation between the timescale and the Peclet number. The result demonstrates that the timescale of the delay also obeys the scaling law $\tau \propto Pe^{-3/2}$. The delay τ represents the time consumed for depleting all droplets in between the

upstream and the downstream region. The reason why the scaling for the delay again is $-3/2$ is simple. The downstream reactions speed up only when upstream droplets have already dissolved. So that the delay between two different regions should be similar to the timescale for droplets between these two regions to react and dissolve.

The delay can also be quantified in the solution of different concentrations while the flow conditions of the solution flow are constant. Fig. 3.6(e) shows the temporal evolution of normalized surface coverage upstream and downstream for different NaOH concentrations. The delay is shorter for the higher concentration of alkali. The relationship between the timescale for the delay and NaOH concentration seen in 3.6(f) also obeys the scaling law $\tau \propto c_{re,bulk}^{-1}$. This scaling is entirely consistent with the correlation between the lifetime of droplets and the alkali concentration in the flow shown in Fig. 3.3.

The dissolution of non-reacting droplet array exposed to a flow of immiscible liquid has been studied in previous work. It was found that not only the flow rate but also the location of the droplet in the array influence the rate of droplet dissolution [127]. Droplets at the corners and the edges of the arrays dissolve faster than the droplets surrounded by many neighbours due to collective effect in droplet dissolution. The collective effects are more pronounced at low flow rates [130, 131], resembling the delay of downstream droplet reactions observed in our present work. The lifetime of the non-reacting droplets followed the scaling law $\tau \propto Pe^{-1/2}$, clearly different from the case of reacting droplets in our cases. As shown here, the difference in the scaling relation with Pe can be attributed to the effect of the transport of reactants with the flow.

3.4 Conclusion

We investigate the kinetics of chemical reaction between surface nanodroplets and the solute in a flow, and establish the relationships between the reaction rate of the droplets as revealed by their shrinkage and the flow rate and the reactant concentra-

tion in the bulk. The reaction of the droplets becomes faster at higher flow rate or with a higher concentration of the reactant in the flow. The droplet reaction time scales with $\sim Pe^{-3/2} c_{re,bulk}^{-1}$. Enhanced transport of the reactant and of the product from the droplet surface by the flow contribute to accelerated kinetics of droplet reaction. Along the direction of the flow, the product from the upstream reaction postpones the reaction of the downstream droplets.

As demonstrated in this work, even a simple acid-base reaction that takes place at the interface between the droplets and the immiscible flow can involve complicated mechanisms influenced by chemical kinetics, interface phenomena, convective and diffusive transport. The understanding presented in this work provides a useful insight into the design and control of droplet reactions in a broad range of applications, such as droplet-based sensing, heterogeneous catalysis or polymer particle synthesis.

Chapter 4

Size Effect on Reaction Rate of Surface Nanodroplets

4.1 Introduction

In-droplet chemistry is important for a wide range of reactions that involve reactants or products in immersible solvents. The large surface-to-volume ratio of microdroplets is desirable for efficient mass transfer crossing the interface in biphasic reactions [13]. In heterogeneous catalytic reactions, catalyst adsorbed at the droplet surface has access to the compounds dissolved in both aqueous and organic phases [84, 132]. Thanks to these advantageous features, droplet reactions are increasingly employed in drug discovery, synthesis of fine chemicals, biofuel conversion [83, 133], and in fabrication of structured materials [134, 135], such as polymeric microcapsules or microspheres [136], porous membranes [137], lightweight materials [138], and food grade foams [139]. In tandem with fast analytic techniques, droplet reactions are indispensable in personalized medicine [15, 16], point-of-care diagnostics [140], anti-counterfeiting, [17] food safety [141], or environmental monitoring [142]. However, up to now what determine the rate of droplet reactions is not fully understood yet.

Rates of droplet reactions have been reported to be dramatically different from their macroscopic counterparts. Cooks and Zare investigated a range of chemical reactions in microdroplets on flight produced by atomized sprays [20, 21, 24]. They found that Pomeranz-Fritsch synthesis of isoquinoline was much faster, sometimes

even by a factor of 10^6 faster than the same synthesis in bulk [19]. Reactions that are extremely slow in bulk may occur readily in droplets. Notably, biomolecules including sugar phosphate and ribonucleoside can be synthesized at enhanced reaction rate in these flying droplets [22, 23]. Accelerated reaction kinetics was also observed in droplets from vapor condensation [28], and immersed droplets with liquid-liquid interface [29, 39]. The reactions are hydroperoxide generation [28], Mannich reaction [29], and dehydrocoupling of hydrosilanes [39]. Apart from accelerated rates, droplet reactions may even produce new intermediates and product [22, 143]. For instance, new intermediates not present in bulk reaction was observed in droplets for phosphorylation between phosphoric acid and sugars [22].

Several hypotheses have been proposed to account for the accelerated kinetics of droplet reactions. For droplets on flight, rapid solvent evaporation leads to droplet shrinkage in volume and consequently the increase in the reagent concentration, which may explain the enhanced reaction rate in the droplets [121, 144]. Besides, a general effect of surface enrichment and orientation alignment for water-soluble probes, which results in a local electric field at the interface between water and a hydrophobic medium, might account in part for unique properties of chemical reactions in microdroplets [36, 37]. In case of reagents localized at the liquid-liquid interface of the droplet, higher surface-to-volume ratio of the droplet contributes to enhanced mass transport of reagents and product throughout the interface, and thus the overall reaction kinetics [1, 29, 39]. Other important effects are from the accelerated electron transfer and molecular configuration of chemicals at the interface with asymmetric environment on each side [22, 30]. The interfacial molecules are activated from solvation with lower energy barrier for the reaction and faster kinetics [31, 32]. Though multiple possible mechanisms were proposed to interpret the accelerated kinetics, however, the quantitative analysis based on tracing in-situ droplet reaction is still missing.

Surface nanodroplets serve as an ideal model system for in-droplet chemistry to

quantitatively study the reaction rate. Surface nanodroplets are droplets on a solid substrate in contact with a liquid immiscible with the droplet liquid [4]. Here nano- refers to the height of the droplets less than 100 nm. The base diameter of the droplets ranges from hundreds nanometer to tens of micrometer and the volume from atto- to femto- litters. The size distribution and chemical composition of surface nanodroplets can be well controlled by a simple method called solvent exchange [96–98]. Surface nanodroplets are stationary, due to pinning on their boundary. Stability of surface nanodroplets enables us to follow in-situ the change in the droplet size resulted from chemical reactions [4], and to quantify the chemical composition in nanodroplets by sensitive molecular spectroscope, such as attenuated total internal reflection infrared [145] or surface enhanced Raman spectra [77]. In particular, the stability of surface nanodroplets allows for supplying the reactant in an external flow under well-controlled conditions to investigate the effect of diffusion and convection on the reaction rate of droplets.

As a nanodroplet is usually surrounded by many neighbours, the collective effect from the reaction of neighbouring droplets is an important aspect to understand the rate of droplet reaction. In our recent work, we studied the effects from external flow conditions on chemical kinetics of the biphasic reaction. In a model system, surface nanodroplets of oleic acid reacted with alkali dissolved in an external flow [1]. The flow rate influenced the transport of both the reactant and the product. We obtained a scaling law of droplet shrinkage rate with the dimensionless number Peclet [1]. The reaction of neighbouring droplets hinders the droplet reaction, due to product diffused in the surrounding. However, it remains unclear what the correlation is between the reaction rate and the droplet size and how a non-reactive component in droplets influences the reaction rate.

In this work, we will focus on the dependence of reaction rates on the size of individual droplet with or without neighbouring effect. The reactive droplets consist of either pure or binary liquid (binary droplet). We are able to establish quantita-

tive correlation between the reaction rate and the size of both pure and composite droplets. The findings in our work may not only serve as the basis for improving the understanding of the altered kinetics of chemical reactions at the droplet surface, but also help to design the droplet reactions, heterogeneous catalysis, advanced materials fabrication, and other applications based on reactions with droplets.

4.2 Methodology

4.2.1 Chemicals and materials

Oleic acid (OA in brief, ≥90%, Fisher), ethanol (≥89%, Fisher), sodium hydroxide (≥97%, Alfa Aesar), decane (≥99%, Fisher), and octadecyltrichlorosilane (OTS) (≥95% Fisher) were used as received without any further purification. Ultra-pure Water (18.2 MΩcm, Millipore) was used in all experiments. Silicon substrates (100 mm in diameter and 500 μm in thickness, Universitywafer, US) were hydrophobized with OTS by following a reported procedure [128]. Before use, coated substrates were sonicated in ethanol and then in water for 5 minutes, and dried in a stream of air.

A fluid channel was self-designed for droplet formation and reaction. As sketched in Figure 4.1A, the channel consisted of a polymethyl methacrylate (PMMA) base, an inlet and an outlet drilled in the base, a top cover glass, and a silicone spacer. The micro-channel inside PMMA was drilled by hole puncher. The substrate was located on the center of the base. All experiments of droplet formation and chemical reaction were performed at temperature of 21°C.

4.2.2 Preparation of pure OA droplets with low surface coverage

OA droplets with low surface coverage were prepared by the film breaking method [79]. Figure 4.1B schematically demonstrates the film breaking method. An OA drop was placed on the substrate (25 mm by 8 mm) by using a micropipette. The initial OA drop was controlled at 500 μm in base radius. Then, the channel was assembled

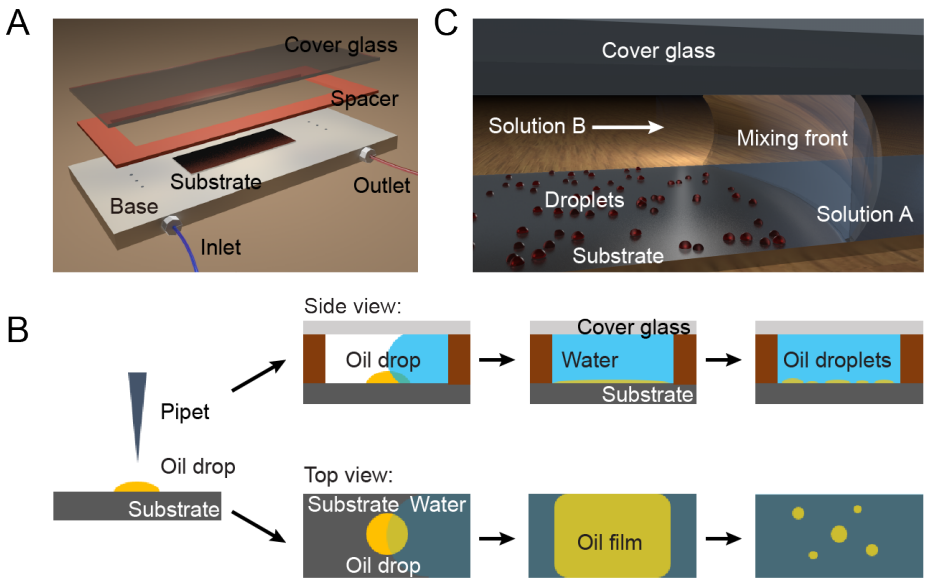

Figure 4.1: Sketch of the experiment setup: (A) The micro-channel for formation and reaction of surface nanodroplets. (B) Procedure of droplet formation by the method of film breaking. (C) Illustration of droplets formed by solvent exchange. The white arrow in the chamber points the direction of the alkali flow.

and sealed with spacers and clips. The height h and the width w of the channel were respectively 2.4 mm and 15 mm.

After the channel was assembled, water was slowly injected into the channel through a syringe. When the water-air interface passed the drop, the drop deformed into a film of oil. The oil film broke up and formed several smaller OA droplets. The lateral diameters of the newly formed droplets ranged from several microns to tens of microns. After film breaking, around 10 to 30 droplets were formed in each experiment. The distances between newly formed droplets were from tens of micrometers to several millimeters.

4.2.3 Preparation of pure OA droplets with high surface coverage

OA droplets with high surface coverage were formed by solvent exchange [96], to test the collective effect from neighbouring droplets on the reaction kinetics. In solvent exchange experiments, the height h and the width w of the channel were respectively

0.4 mm and 15 mm. Before solvent exchange, two solutions were prepared. Solution A was 2.6% (v/v) OA in the mixture of ethanol and water with the ratio of 7:3 (v/v). At first, the fluid channel was filled with solution A. Water (solution B) was then injected into the channel with a programmable syringe pump (New Era, NE-1000). The volume flow rate of solution B was 500 μL/min.

When the mixing front of two solutions passes over the substrate, as sketched in Figure 4.1C, droplets nucleate and grow due to the oversaturation of OA in the mixing front. In each group of the experiments, around 4,000 surface droplets can be formed in the field of view (0.34 mm^2). Thanks to the well-controlled fluid conditions, droplets for different experiments had consistent size distribution and number density. The initial surface coverage SC_0 were $\approx 25\%$. SC_0 is defined as the proportion of the substrate surface occupied by droplets after droplet formation. The averaged droplet radius was controlled at ~ 2.4 μm.

4.2.4 Preparation of binary droplets

Binary droplets of OA and decane with low surface coverage were also prepared by film breaking method. A binary drop of 5%/10% decane and 95%/90% OA in volume was placed the substrate. Water was slowly introduced into the chamber by a syringe, and the initial drop broke up to several smaller droplets. Binary droplets with high surface coverage were prepared by solvent exchange method. Solution A was prepared by adding decane and OA into 70% ethanol aqueous solution. Then standard solvent exchange was performed.

When producing binary droplets by solvent exchange method, the composition of binary droplets was determined by the oversaturation level of each component in the mixing front [108]. The oversaturation level can be expressed on the ternary phase diagram, by the area surrounded by the binodal curves and the dilution path. Based on the solution composition in initial solutions and ternary phase diagram, the corresponding composition of surface droplets can be approximately calculated.

The details of the calculation can be found in literature [97, 98]. Nine points in the ternary phase diagrams of oleic acid and decane in Figures 4.2A&B were taken from IUPAC-NIST Solubility Database and additional points were obtained by titration for a complete diagram. Table 4.1 lists all solution A compositions, solution B flow rates, and the composition of formed surface nanodroplets.

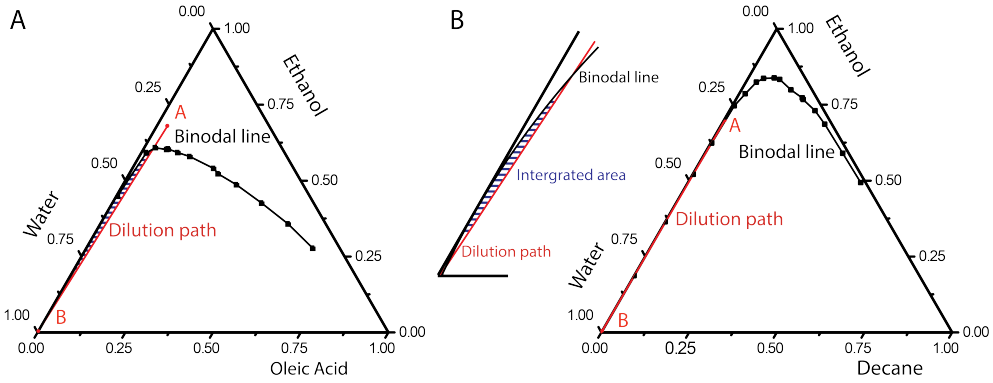

Figure 4.2: Ternary phase diagram of (A) oleic acid and (B) decane. Points A and B in plots are the composition points of solutions A and B. The shaded area surrounded by the dilution curve (red line) and binodal line (black line) in the plot reflect the oversaturation level of OA (A) and decane (B) in the mixing front.

Table 4.1: Solvent exchange conditions and corresponding droplet compositions

OA in solutin A (v/v)	Decane in solution A (v/v)	Solution B flow rate (μL/min)	Decane in droplet (v/v)
2.8%	0%	500	0%
2.8%	0.16%	500	3%
2.8%	0.21%	500	5%
2.8%	0.25%	500	7%
2.8%	0.28%	500	9%

After solvent exchange, around 5,000 binary droplets were produced with a similar number density and size distribution in the field of view. The initial surface coverage of binary droplets was controlled at $\approx$ 34% for all groups of experiments. We note that the group with 10% decane in droplets was an exception. Due to the coalescence

of droplets during the solvent exchange, only around 3,000 droplets formed in the recorded area, and the surface coverage was around 38%.

4.2.5 Flow and solution conditions for droplet reaction

An aqueous solution (solution C) of sodium hydroxide was prepared to react with OA droplets. The concentration of NaOH was constant at 4.0×10^{-4} M for all experiments. We chose the specific concentration of NaOH for a suitable reaction rate that the reaction process is not too fast or too slow to be followed in-situ.

After droplet formation, solution C was injected into the channel by the syringe pump at a constant flow rate. In experiments of droplets with low surface coverage, the flow rate in volume Q were controlled at 167 μL/min, where the corresponding Peclet number Pe was 52. Pe is defined as $Pe = Q/(wD)$, where Q and w are the volume flow rate and the channel width. In experiments of pure droplets with high surface coverage, the flow rates Q varied from 100 to 645 μL/min, where corresponding Peclet numbers were Pe =15-198. In experiments of binary droplets with high surface coverage, Q =167 μL/min and Pe =52.

Reacting droplets were recorded by an upright microscope (Nikon H600L, 10x objective lens) with a video camera (Nikon, DS-Fi3, 0.24 μm/pixel, 5.0 fps). A white-light LED lamp was used for bright field imaging. How droplets were selected and presented in different sections was discussed in Supporting Information. ImageJ and self-written Matlab codes were used to process and analyze the filmed images. The base area, A, of droplets as function of time, and the surface coverage, SC were extracted frame by frame. Time zero (t_0) was defined as the moment when solution C reached droplets. t_0 was separately predetermined by flowing the alkali solution at the same flow rate in an empty fluid channel.

We assume that the droplets are spherical caps. Their boundaries are expected to be circular, due to low surface tension of the surfactant product and low pinning effect on the homogeneous substrate. Only occasionally droplets were seen to be

pinned, possibly due to imperfection of the substrate. The base radius of the droplet R was calculated as $R = (A/\pi)^{0.5}$. Droplets that are too large ($R_0 > 13$ μm) or too small ($R_0 < 3$ μm) in their initial sizes were excluded, to avoid too long or too short reaction time.

The experimental uncertainty was estimated to be the spatial resolution of the microscope (0.24 μm, pixel size). We note that although there may be systematic errors in the dimension due to the spatial resolution limitation in our optical images, such systematic errors do not influence our results determined by the change of droplet size.

4.3 Results and discussion

The reaction between oleic acid (OA) droplets and alkali in the solution is shown below

$$\begin{aligned} &CH_3(CH_2)_7CHCH(CH_2)_7COOH + OH^- \\ &\rightleftharpoons CH_3(CH_2)_7CHCH(CH_2)_7COO^- + H_2O. \end{aligned} \tag{4.1}$$

Figure 4.3 sketches the process of the droplet reaction. Carboxyl groups of OA tended to stay at the waterside of the interface, since they are hydrophilic. Hydroxide ions in the solution were transported to the droplet by the flow, and reacted with the carboxyl groups. OA is converted to oleate. After reaction, oleate dissolved in the OA droplet and the surrounding solution. The later and was carried away by the flow. The overall process consisted of (1) mass transport of alkali from the laminar flow to droplet interface, (2) reaction between alkali and carboxyl at the droplet interface, (3) product (oleate) desorption from the droplet surface, and (4) product dissolution in the droplet and transport by the flow [1].

4.3.1 Size effect on reaction kinetics of pure droplets

Three series of snapshots in Figures 4.4A-C reveals progressive shrinkage of reacting droplets with different initial sizes. The second and third columns of snapshots in

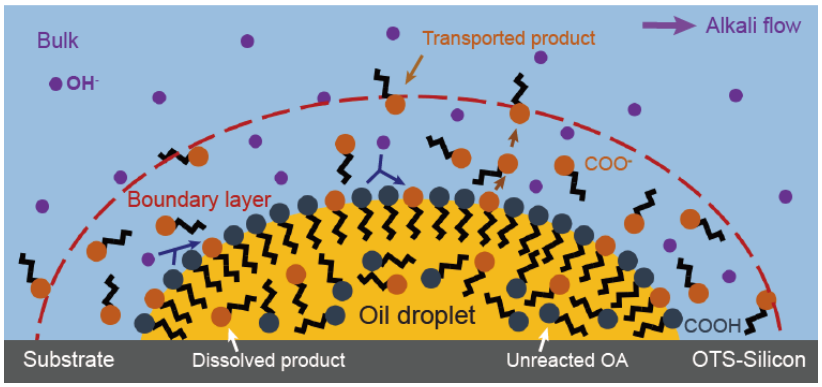

Figure 4.3: Reaction between alkali in the flow and an OA droplet. The –COOH head group (indigo) reacts with OH^- (purple) from bulk, producing $–COO^-$ head group (orange). Black chain in the figure is the hydrophobic tail of reactant and product. The reaction is indicated by the blue arrow. The red dashed line show the diffusive boundary layer of product out of the droplet. Purple arrow on the top indicate the direction of the flow.

Figure 4.4A-C reflect the continuous shrinkage in the lateral radius of the droplet from the moment when reactant solution reached the droplets till disappearance in the fourth column.

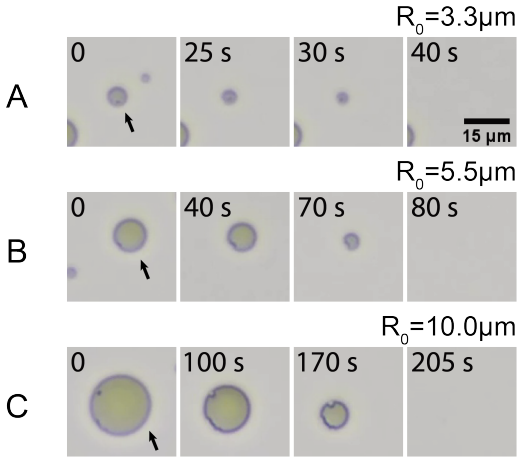

Figure 4.4: Optical images of surface nanodroplets reacting with the alkali solution. The initial radius at $t = 0$ of droplets (pointed by the arrow) in (A)-(C) were $R_0 = 3.3$ μm, 5.5 μm, and 10.0 μm, respectively. The black arrow points to the reacting droplet.

The lateral radius of droplets was analyzed as the function of time and the results are plotted in Figure 4.5A. R_0 represents the initial lateral radius of droplets at t_0. In general, the shrinkage of droplets speeds up as time proceeds. In other words, the

rate of the reaction is dependent on the size of the reacting droplet.

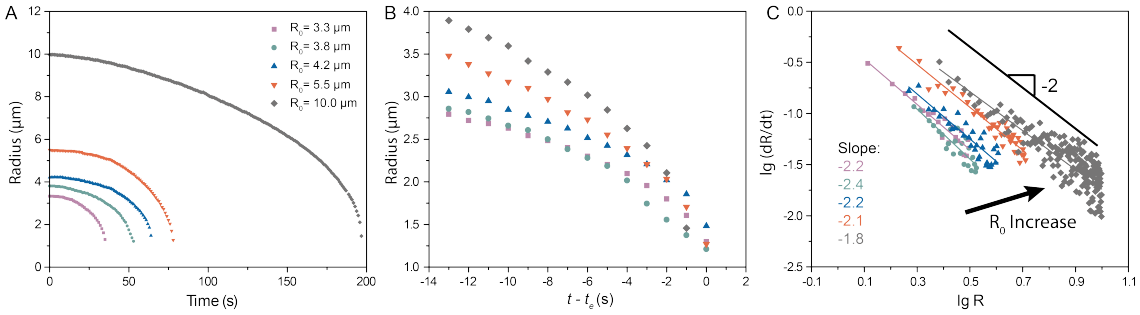

Figure 4.5: (A) Lateral radius R of OA droplets with different initial sizes as a function of time. R_0 represents the initial lateral radius at t_0. Legends in (A) carry the same meaning throughout Figure 4.5. (B) Shrinkage of each droplet in the last 14 seconds when they are larger than 1.2 μm rescaled from (A). (C) Dissolution rate $\dot{R}$ as function of R of droplets with different R_0 values. The coefficient R^2 of the fitting ranges from 0.74 to 0.93. The black solid line represent the result $\dot{R} \propto R^{-2}$ from the scaling analysis. At least three experimental replicates were performed under the same conditions in this section. Overall, 12 curves were obtained to confirm the correlation in Figure 4.5C.

The dissolution curves of droplets near the end were plotted in Figure 4.5B. The time zero here is re-scaled by subtracting t_e from time, where t_e is the last second when the droplet was larger than 1.2 μm in lateral radius. Figure 4.5B reveals that the droplets tend to have similar dissolution rates when they are similar in the instantaneous lateral radius. These results suggest that the instantaneous lateral radius of the reacting droplets plays the major role in determining dissolution rate.

We compared the dissolution rates of the same droplet at different times to understand the effects from the droplet size (i.e., radius) on the surface kinetics quantitatively. The average dissolution rate $\dot{R}$ in each second was determined by calculating the variation of lateral radius R. In Figure 4.5C, the dissolution rates $\dot{R}$ were plotted as function of the instantaneous radius R. All the droplets collapse into the universal scaling with the exponent of -1.8 to -2.2, while the pre-factor varies with the initial radius.

Our results suggest that the droplet dissolution rate was accelerated by reducing the droplet radius R, scaling with R^{-2}. Although entirely different in the mechanism,

this dependence of the dissolution rate on R^{-n} is close to earlier reports in which acceleration in reaction rate was attributed to the thermodynamic variation from chemical adsorption and desorption at the interface [29, 39].

4.3.2 Reaction kinetics of droplets at high surface coverage

Solvent exchange was applied to produce OA droplets with a large number density. The initial surface coverage of OA droplets was fixed at $\approx 25\%$. The probability distribution functions (PDF) of size of OA droplets in Fig 4.6E suggests that the size distributions of droplets were all similar at t_0 in the four groups of experiments. Series of snapshots in Figures 4.6A-D reveals that OA droplets progressively shrank at different flow rate of the reactant solution. It is noteworthy that the droplets did not shrink from t_0, but remained at almost its initial radius for certain time. This period is defined as stage 1, in which the product from upstream droplets transported along the flow hindered the downstream reactions. It is a different trend when compared to the low surface coverage cases, where the hindering effect was relatively weak, and the dissolution starts immediately after the alkali solution entering the field. As expected, the duration of stage 1 was shorter at higher flow rate of the reactant solution.

Figure 4.6F presented the lateral radius of droplets as a function of time after stage 1. Data in Figure 4.6F were extracted from the analysis of the video of Figure 4.6A ($Pe = 15$). After stage 1, dissolution rate of droplets continuously increased until droplets finally disappeared. At stage 2, most upstream droplets were depleted and removed by the flow, and the surface coverage of nearby droplets also decreased. The hindering effect does not play a significant role anymore at stage 2. We also defined a transition stage between stages 1 and 2, in which droplets started to dissolve at an observable rate, while the hindering effect from products was still pronounced.

Since droplets did not shrink much in the first stage, we at first focused on the second stage of the shrinkage. Based on the data marked by the red box in Figure 4.6F, we analyzed the dissolution rate $\dot{R}$ in the second stage. The surface coverage at

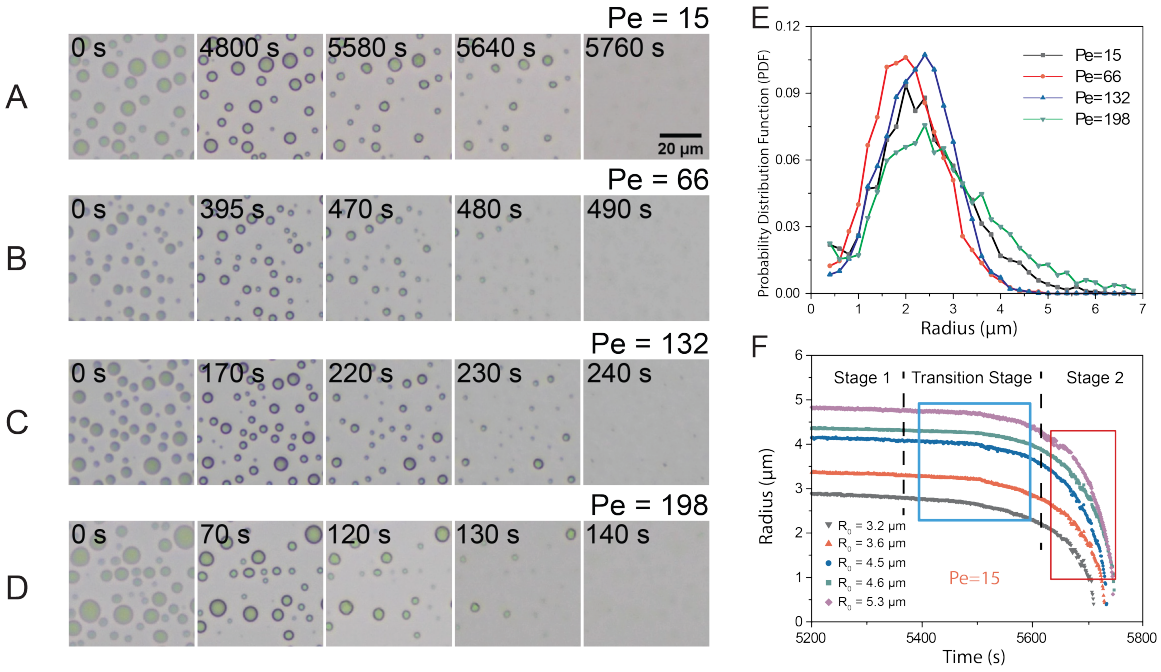

Figure 4.6: (A)-(D) Screenshots of nanodroplets with high surface coverage shrinking in the alkali flow at different flow rates. The flow rates were controlled at 50, 215, 430 and 645 μL/min from (A) to (D), which corresponds to Peclet numbers from 15 through 198. (E) Probability distribution functions (PDF) of droplet base radius after droplet formation. Only droplets with the base radius larger than 0.3 μm are demonstrated in (E). (F) Lateral radius R of droplets with different initial sizes as function of time from $t = 5200$ s to the end of the dissolution. Data in (F) were obtained from the analysis of the video of 4.6(A) ($Pe = 15$). Black dashed lines in (F) divide dissolution stages.

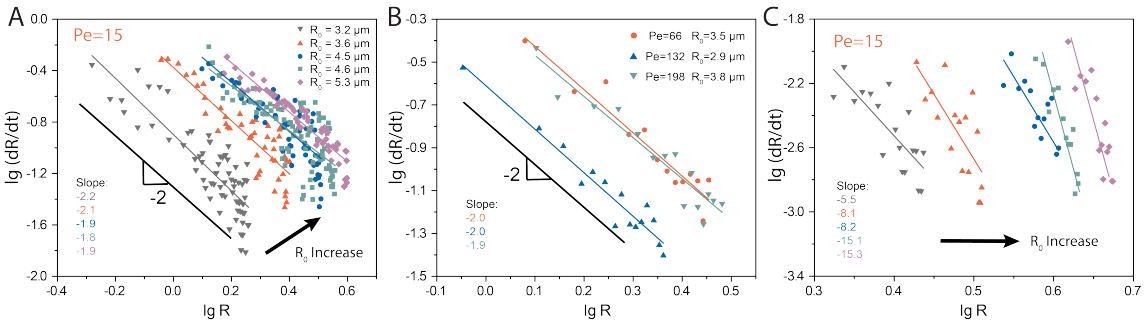

Figure 4.7: (A) Scaling relationship between $\dot{R}$ and R for droplets with different initial sizes in stage 2 ($Pe = 15$). Data in (A) were obtained from the red box in Figure 4.6F. Legends in (A) carry the same meaning in (C). (B) Scaling relationship between $\dot{R}$ and R at the higher Peclet numbers ($Pe = 66$, 132, and 198) in stage 2. The coefficient R^2 of the fitting ranges from 0.49 to 0.93. The black solid lines in (A)&(B) represent the result $\dot{R} \propto R^{-2}$ from the scaling analysis. (C) Scaling relationship between $\dot{R}$ and R for droplets with different initial sizes at the transition stage ($Pe = 15$). Data in (C) were obtained from the blue box in Figure 4.6(F). The coefficients R^2 of the fitting range from 0.55 to 0.79. For each Peclet number, more than 10 droplets were analyzed to establish the correlation in this section.

$t = 5,640$ s was 7.1%. As shown in Figure 4.7A, the dissolution of individual droplets obeys the scaling law $\dot{R} \propto R^{-n}$ with $n = 1.8 - 2.2$, which agrees well with that found for low surface coverage droplet reaction. We also analyzed the higher Peclet numbers data. Figure 4.7B shows the exponent $n = 1.9 - 2.0$ at Pe =66, 132, and 198. Data in Figure 4.7B were extracted from the analysis of the video of Figures 4.6B-D. Only the result of one droplet was presented for each group of Peclet numbers. The data from droplets with different initial sizes at the same Peclet number are presented in Figure 4.8. When the surface coverage is relatively low, the size effect was more pronounced rather than the hindering effect.

We then analyzed the dissolution data in the transition stage (t =5,400 s to 5,600 s, blue box in Figure 4.6C). The surface coverage at $t = 5,400$ s was 14.6%. The droplets shrank slowly, likely due to the hindering effect triggered by the high surface coverage. We calculated the average shrinkage rate every 5 or 10 seconds and obtained the scaling exponents (Figure 4.7C). Compared with the results extracted in stage 2, two general features were: (1) results in transition stage usually have larger scaling

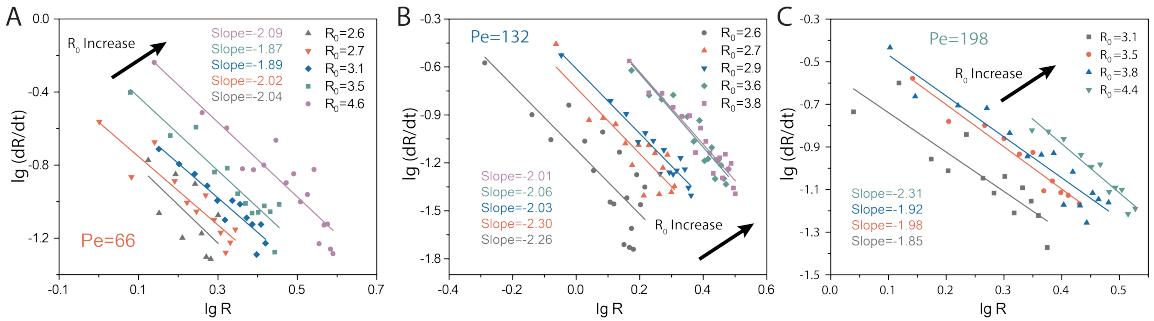

Figure 4.8: Scaling relationship between $\dot{R}$ and R for droplets with different initial sizes: (A) Pe = 66, (B) Pe = 132, (C) Pe = 198.

exponents between $\dot{R}$ and R compared with the stage 2, (2) droplets with larger initial sizes tend to have larger exponents n.

The larger scaling exponents in the transition stage may be explained by the attenuation of the hindering effect. In the transition stage, the upstream droplets were gradually depleted. The concentration of the products in the flow continuously decreased, and thus the hindering effect become weaker. Consequently, the shrinkage rate, $\dot{R}$, increased with time. Besides, due to the low shrinkage rate, the droplet size was reduced little and contributed less to the increasing shrinkage rate. As a result, the scaling exponents became much higher than -2. Besides, droplets with small initial sizes tend to have a large product transportation rate, suggesting that small droplets can immediately finish the transition stage [1]. Thus, the scaling exponent for smaller droplets could be rather close to -2 than their larger counterparts.

4.3.3 Size effect on reaction of binary droplets

To test how the addition of the non-reactive, surface inactive components will influence the biphasic reaction at droplet surface, binary droplets were formed with low surface coverage by film breaking method. Compared with decane, OA is surface active, due to the carboxylic acid group. Figures 4.9A&B are snapshots of binary droplets shrinking in the alkali flow. Assuming that the compositions of droplets were consistent with the compositions in the oil film, the decane ratio of droplets shown in

Figures 4.9A&B were 5% and 10% (v/v). Similar to pure droplet reaction with low surface coverage, binary droplets immediately shrank when alkali entered the field of view. Adding the non-reactive component, droplets did not completely disappear on the substrate at the end in contrast to OA droplets. Non-reactive and insoluble decane were left on the substrate in the form of smaller droplets, as demonstrated by the fourth snapshot in Figures 4.9A&B. 10% decane droplets cause a larger residual droplet when compared to 5% decane binary droplets with the similar initial sizes, as 10% decane binary droplets contain more decane, which made up the main part of the residual droplets.

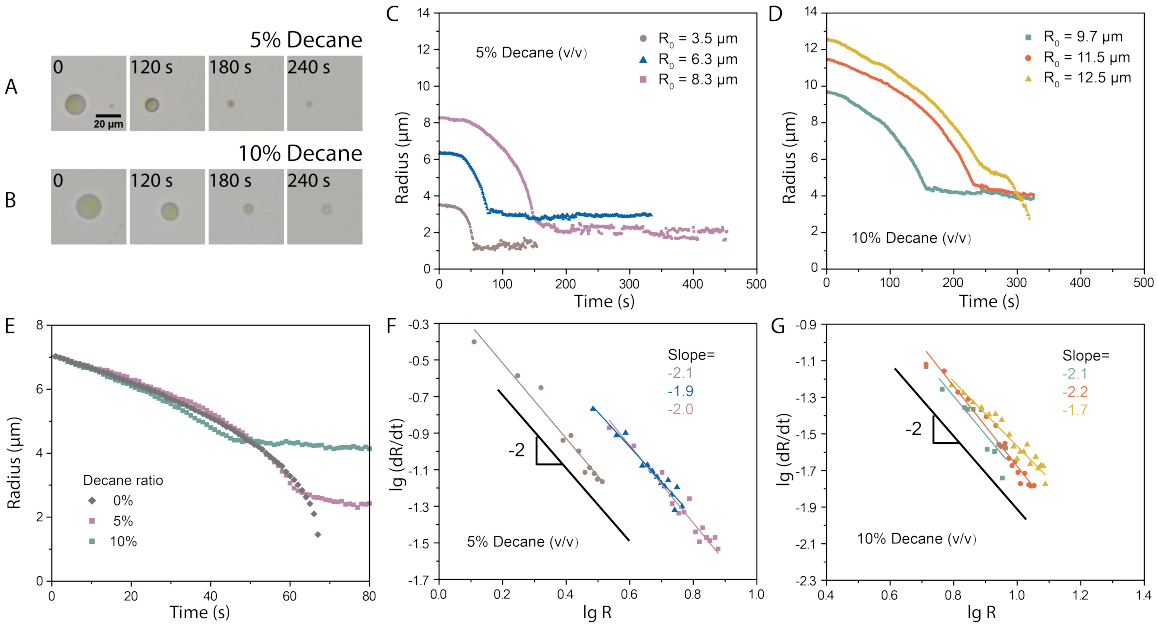

Figure 4.9: (A)&(B) Optical images of decane/OA binary droplets reacting and dissolving in the alkali flow. The volume ratio of decane was 5% in (A) and 10% in (B). The corresponding Peclet number Pe was 10. (C)&(D) Lateral radius R of binary droplets with decane volume ratio 5% and 10% as function of time. Legends in (C)&(D) carry the same meaning throughout Figure 4.9. (E) Shrinkage of droplets of 0% ($R_0 = 10.0$ μm), 5% ($R_0 = 8.3$ μm), and 10% ($R_0 = 9.7$ μm) decane ratio. The time zero is defined as the moment when lateral radius of each droplet decreased to $R = 7.0$ μm. (F)&(G) Dissolution rate $\dot{R}$ calculated every 10 seconds as function of R. Results in (F)&(G) were from the analysis of data in (C)&(D). The coefficient R^2 range from 0.71 to 0.97. The black solid lines in (F)&(G) represent the result $\dot{R} \propto R^{-2}$ from the scaling analysis. For each droplet composition, at least three experimental replicates were performed under the same conditions. Overall, 14 droplets were analyzed to obtain the correlation in Figure 4.9F&G.

Figures 4.9C&D are the lateral radius of binary droplets as function of time. After the alkali reached binary droplets, the dissolution was gradually accelerated with the decreasing radius, and finally stopped when the OA component in binary droplets was run out. Figure 4.9E compared the dissolution process of 5% and 10% decane binary droplets with the pure OA droplet, where the time zero was set as the moment when droplets dissolved to $R = 7.0$ μm. Importantly, the droplets dissolved at the same rate when they have consistent sizes, insensitive to the decane ratios. This result suggests that the ratio of the non-reactive component does not influence the biphasic reaction in surface nanodroplets significantly. We believe that the surface inactive decane tends to stay at the inner part of the binary droplet, while surface-active OA mainly locates at the droplet outer layer. The concentration of OA at the droplet surface and thus reaction rate is not influenced by the decane ratio in droplets. The above results can be compared with Pickering emulsions in which the functionalized particles with high surface activity stay at the droplet surface and occupy the reacting site.

The scaling analysis of the relationship between $\dot{R}$ and R are shown in Figures 4.9F&G. The size effect ($\dot{R} \propto R^{-n}$, $n \sim 2$) can also be found in binary droplets. The addition of non-reactive components does not influence the size effect including the scaling exponent. This result also suggests that the non-reactive decane with low surface activity was hidden in the inner part of the binary droplet. As a result, the -2 exponent can be maintained even the ratio of decane in binary droplets continuously increase as the reaction proceeds.

4.3.4 Binary droplet reactions at high surface coverage

Binary droplets with high surface coverage were formed by solvent exchange and their reaction kinetics was investigated. Figures 4.10B-E display snapshots of binary droplets with different decane compositions formed by solvent exchange, while the snapshots of pure OA (i.e., 0% decane) droplets were arranged in Figure 4.10A for

comparison purposes. The amount of added non-reactive content increases as the concentration of decane increases, and the time needed to finish the dissolution process becomes longer. We note that decane is insoluble and remains on the substrate even after finishing the dissolution process (see the fifth snapshots) as found in the case for binary droplets with low surface coverage.

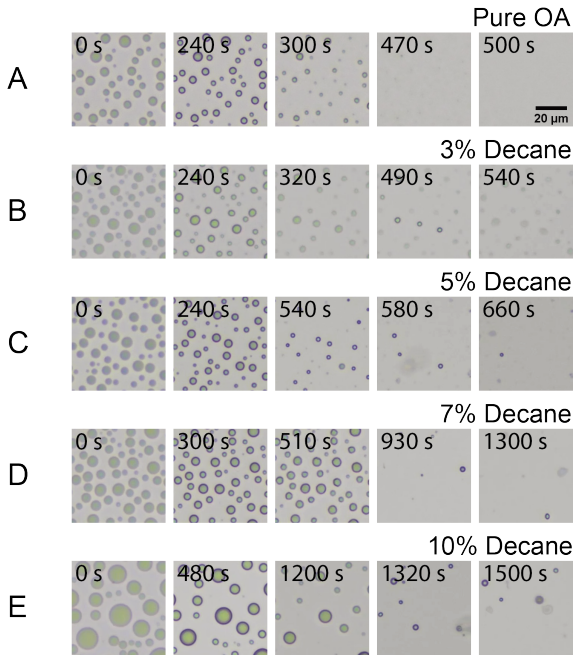

Figure 4.10: (A)-(E) Optical images of nanodroplets with different ratios of OA and decane reacting with the alkali flow. The approximate decane contents in surface droplets were from 0 to 10% in (A) to (E) respectively.

Figure 4.11A shows the probability distribution functions (PDF) of binary droplets with different OA/decane ratio. The initial droplet size distributions are similar to each other, except for the 10% decane group. (n% decane refers to the decane composition in droplets.) In the 10% decane group, the number density of droplets decreased to around 3000, suggesting that some droplets merged and became larger, as confirmed in Figure 4.10E. Consistently, 10% decane group shows a relatively less population of droplets for the smaller lateral radius, while a much greater number of droplets were confirmed for the larger lateral radius, as presented in Figure 4.11A.

With the collective effect from high surface coverage of droplets, the diffusion

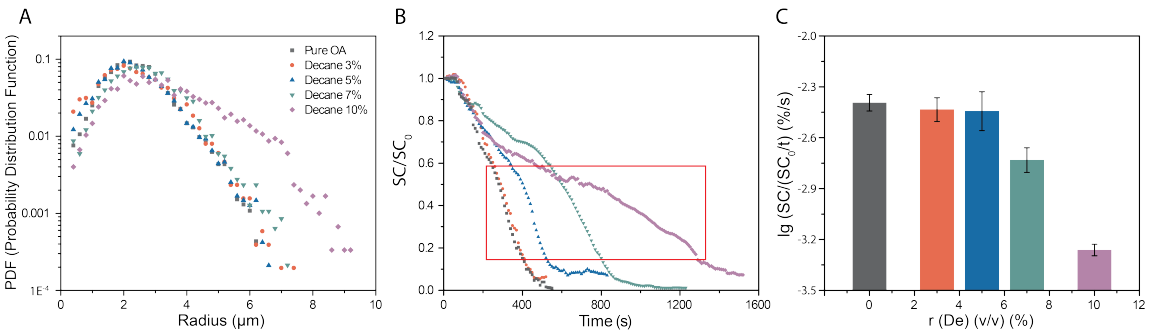

Figure 4.11: (A) Probability distribution functions (PDF) of droplet base radius. Only droplets with the base radius larger than 0.3 μm are demonstrated in (A). (B) At different flow rates, normalized surface coverage SC/SC_0 varied with time. SC_0 is the initial surface coverage. (C) Average dissolution rate at stage 2 in terms of normalized surface coverage (calculated from SC/SC_0 =0.60 to SC/SC_0 =0.15). r is the volume ratio of decane in binary droplets. Error bars in (C) were calculated from three individual runs of experiments.

of a binary droplet became complicated to be quantified without considering the neighbouring droplets. Hence, instead of presenting the lateral radius of a single droplet, we take a large number of droplets in a specific area as the entity to reduce variation from individual droplets surrounded by different neighbours.

The normalized surface coverage SC/SC_0 (normalized by the initial surface coverage after droplet formation) were analyzed quantitatively as a function of time in Figure 4.11B. Binary droplets with the higher volume ratio of decane have different dissolution rate for each concentration, while 3% decane binary droplets were similar to pure droplets.

Figure 4.11C shows the relationship between dissolution rate (see the marked region by the red box in Figure 4.11B) and decane volume ratio in droplets. The vertical and horizontal axes are respectively the normalized surface coverage and the decane volume ratios in droplets, which were estimated with the three-phase diagram. Data in Figure 4.11C were calculated from SC/SC_0=0.15 to SC/SC_0=0.60 (see red box in Figure 4.11B). Notably, the dissolution rate at the fast dissolution stage (stage 2) of pure OA, 3% decane and 5% decane group were similar to each other. The existence of decane does not slow down the reaction rate in these groups significantly.

In contrast, the 7% decane group was a little slower, while the 10% decane group was much slower than the other group. In the 10% decane group, much larger droplet sizes contribute to decelerating dissolution. For the 7% decane group, though the PDF in Figure 4.11A was similar to other groups, we observed a slightly slower reaction when compared to the lower concentrations. It is possibly due to the slightly larger droplet size of 7% decane group (5-7μm) that contributed to lower dissolution rate.

4.3.5 Theoretical analysis and discussion

The scaling of the dissolution of reacting droplets with R^{-n} ($n \sim 2$) is rationalized as below. The biphasic reaction between alkali and OA mainly occurs at the surface of droplets, as the solubility of OA in water is low, and the solubility of alkali in OA droplets is also low. Considering a droplet on the substrate in the shape of a spherical cap, the droplet shrinkage is assumed to be in a constant contact angle (CA) mode for simplicity, i.e., the droplet keeps its contact angle constant all the time [115]. Diffusion-dominated dissolution of the droplet is schematically demonstrated in Figure 4.12.

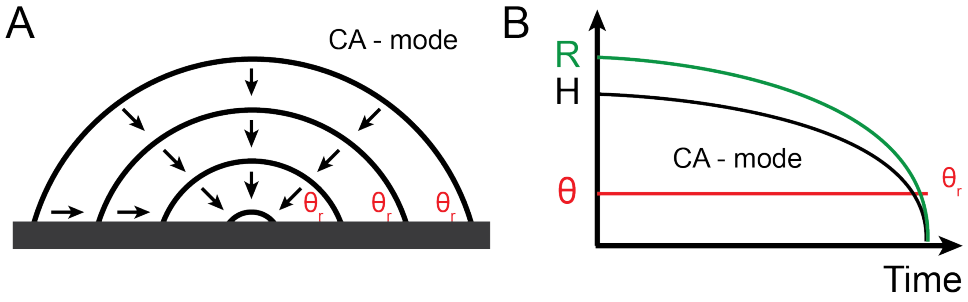

Figure 4.12: (A) Scheme of the diffusion-driven dissolution of a surface nanodroplet dissolving in a constant contact angle (CA) mode. (B) Droplet lateral radius R, contact angle *theta*, and droplet height H of the droplet in (A) as a function of time.

Based on the established transport-reaction model in our previous work [1], the transport of the product from the droplet surface to bulk obeys Prandtl-Blasius-Pohlhausen-type behaviour in a laminar flow. At given time t, the thickness of the boundary layer of the product concentration around the droplet is inversely propor-

tional to the droplet size $R_{(t)}$ [96].

$$\rho R_{(t)}\dot{R} \sim D\sqrt{Pe}c_{pr,sur}. \tag{4.2}$$

$$\dot{R} \propto R_{(t)}^{-1}c_{pr,sur}. \tag{4.3}$$

Here $c_{pr,sur}$ is the concentration of the product at the droplet surface. The product density ρ and the diffusion coefficient D are constants. $R_{(t)}$, and $\dot{R}$ are respectively the lateral radius of the droplet at t and the rate of change in the radius with time. Peclet number (Pe) of the bulk flow is defined as $Pe = Q/(wD)$, where Q and w are the volume flow rate and the channel width.

At given time t, the production rate of product $\dot{m}_{pr}$ can be expressed in terms of the interfacial area $A_{(t)}$ [29, 39, 146].

$$\dot{m}_{pr} \propto A_{(t)} \cdot k \cdot [OA][OH^-]_{sur}. \tag{4.4}$$

k is the reaction rate coefficient.

As OA is insoluble in water, the concentration of OA at the droplet surface is assumed to be constant with time. The concentration of alkali at the droplet surface $[OH]^-_{sur}$ is determined by the Pe-dependent transport and reaction rate coefficient k [1]. The level of $[OA]$, $[OH]^-_{sur}$ or k does not depend on the droplet size. The surface area of the droplet $A_{(t)}$ is $\sim R^2_{(t)}$, hence

$$\dot{m}_{pr} \propto R^2_{(t)} \cdot k \cdot [OA][OH^-]_{sur}. \tag{4.5}$$

The concentration of the product at the droplet surface is mainly balanced by three factors: reaction rate coefficient k, product diffused into the droplet, and by the flow from the droplet. The product diffuses into the droplet and builds up the concentration inside the droplet $c_{pr,in}$. The liquid volume $V_{(t)}$ in the droplet is $V_{(t)} \propto R^3_{(t)}$. Coupling with equation 4.5, the concentration of the product inside the droplet

was given as

$$c_{pr,in} \propto \dot{m}_{pr}/V_{(t)} \propto R_{(t)}^2 \cdot k \cdot [OA][OH^-]_{sur}/R_{(t)}^3 = R_{(t)}^{-1} \cdot k \cdot [OA][OH^-]_{sur}. \quad (4.6)$$

As the droplet size is small with tens to hundreds nanometer in height and the product is soluble in droplet liquid, the concentration of the product at the droplet surface $c_{pr,sur}$ is same as that inside the droplet $c_{pr,in}$.

$$c_{pr,in} \sim c_{pr,sur}. \quad (4.7)$$

From equations 4.3, 4.6, and 4.7 we obtain the scaling law for the droplet dissolution rate $\dot{R}$ as function of droplet size $R_{(t)}$ as

$$\dot{R} \propto R_{(t)}^{-1} c_{pr,sur} \propto R_{(t)}^{-1} \cdot R_{(t)}^{-1} \cdot k \cdot [OA][OH^-]_{sur} = R_{(t)}^{-2} \cdot k \cdot [OA][OH^-]_{sur}. \quad (4.8)$$

Equation 4.8 is in agreement with our experimental results, that the dissolution rate $\dot{R} \propto R^{-2}$.

Our recent work reported the influence of external flow Peclet number on dissolution of reaction droplets [1]. The rate of droplet dissolution scales with $Pe^{3/2}$. Therein the dependence of the reaction rate on the droplet size could be neglected in both experimental and theoretical analysis, as the dissolution rate was represented by the surface coverage, an average over many droplets. In this work, reaction rate is analyzed on an individual droplet level. Together, these two studies provide a comprehensive understanding on the dependence of droplet reaction on droplet size and on the reactant flow.

Enhanced chemical kinetics in small droplets has been frequently reported in literature.[22, 29, 147] However, the exact mechanism for the enhancement depends on the type of reactions and the configuration of the droplets. For flying droplets from atomized spray, all reactants were compartmentalized inside the droplet, in contrast

to our current systems where reactants are in two immiscible phases. Enhanced electron transfer and molecular configuration at the droplet interface led to a low active energy barrier and thus a large rate coefficient k, attributed to the accelerated reaction rate of droplets on-flight.[20, 22] However, the enhanced kinetics in our system was due to the high surface-to-volume ratio of small droplets and size-dependent mass transport of the product, while the intrinsic kinetics of chemical reaction itself (k) remains constant.

For gas-evolution reactions between droplets and a reactant dissolved in a stationary surrounding phase, the gas production rate was reproduced to be also higher in smaller droplets. However, the gas concentration inside droplets is inversely proportional to droplet radius [39, 148], different from $R^n(n \sim -2)$ for droplet dissolution in this work. The reason for a stronger dependence on the droplet size in our reaction is attributed to the influence of the droplet size on the transport of the product to the external flow in equation 4.3, and to the effect of surface-to-volume ratio on the product concentration in droplets as shown in equation 4.6. The shifted balance between chemical reaction and enhanced mass transport contributed to faster overall kinetics of the process. The proposed mechanism can be extended to reactions crossing a flat surface, the reactions take place but are extremely slow, as a result of a much thicker diffusion boundary layer.

The results and analysis based on our model reaction are applicable to other reactions with reactants separated in droplets and in the flow of the immiscible phase where the product transport is the rate-limiting step.

4.4 Conclusions

This work reports the quantitative correlation between the chemical reaction rates and the size of reacting nanodroplets. The model reaction in our study is neutralization between oleic acid droplets on a solid surface and alkali in an external flow. The dissolution of the product results in the shrinkage of the droplet size, which reveals

the reaction rate at the droplet surface in time. The quantitative analysis reveals that the reaction rate increases with the decrease in the droplet size, regardless of the coverage of the droplets on the surface, the flow rate of the reactant solution, or the addition of non-reactive liquid in the droplets. The overall kinetics scales with $\dot{R} \propto R^{-2}$. The scaling law is attributed to faster accumulation of the product in the droplets from the larger surface to volume ratio at smaller droplet size and effect of droplet size on the product transport in the flow.

The finding in this work has advanced the current understanding of reaction kinetics of droplets, complementary to the studies on reactions in flying droplets [21, 23, 24, 144, 149, 150], and in immersed reacting droplets without an external flow [29, 39, 151]. The insights from this work may be valuable for designing and controlling biphasic reactions in droplets systems with a reactant in the external flow.

Chapter 5

Growth Rates of Hydrogen Microbubbles in Reacting Femtoliter Droplets

5.1 Introduction

On-drop chemistry has been increasingly explored for fine chemical production based on biphasic reactions [152], synthesis of novel bio- and nano-materials [14], fast and sensitive chemical analysis [153], and engineering chemorobotic platform [154–156]. Notably, many reactions confined in the droplets have been reported to be faster than on a large scale. The reaction rates may be enhanced by 10^2 to even 10^6 times compared to reactions in the bulk [157–159]. Droplet reactions may also simplify post purification processes for a wide range of biphasic reactions where reactants or products are present in two immiscible fluid phases, such as oil and water or liquid and gas [83, 84, 160, 161]. Microdroplet chemistry is considered to be green and sustainable, enabling efficient chemical conversion for a wide range of reactants under mild reaction conditions or without using metal, heat, or expensive catalyst[162].

The fast chemical kinetics in small droplets is attributed to various interfacial phenomena [163], including molecular configuration, local concentration or partial solvation of reactants, or unusual rate of electron transfer at the gas-water interface [22, 23, 30–32]. Electric potential energy localized at the interface may also alter

the internal chemical equilibrium inside microdroplets [33]. Recently it was proposed that the surface of microdroplets may provide an energetically favourable environment for redox reactions in fast enzymatic protein digestion in microdroplet spray [35]. In another case, reactant accumulation at the droplet surface was attributed to enhancement in the reaction between a droplet containing lipids and a droplet containing lipase [164]. The partial solvation of reactants at the interface may explain the accelerated reaction between microdroplets containing amines and CO_2 where the reaction was only confined at the droplet surface [34].

Beyond significant acceleration in reaction rate, microdroplet reaction enables the spontaneous occurrence of reactions that is thermodynamically unfavourable. The type of reactions ranges from oxidation of water in the air to biomolecules or origin of life in prebiotic earth, for instance, the generation of hydroperoxide [28], reduction of 2,6-dichlorophenolindophenol (DCIP) by ascorbic acid in absence of catalyst [20], and production of ribonucleotides from ribonucleosides [27].

Higher chemical efficiency was reported not only for reacting droplets in the gas phase, but also for reactions between microdroplets and reactants dissolved in the surrounding liquid. An example is Mannich reaction in emulsion droplets [29]. A comprehensive analytic model was developed to explain the fast reaction rate of emulsion droplets [29]. The reaction-adsorption mechanism took into account the reaction equilibrium constant and forward rate constant associated with the concentration difference of the reactants throughout the droplet.

The mass flux between the droplets to the surrounding phase also plays an important role in the droplet reaction kinetics [1, 2]. In this regard, femtoliter droplets immobilized on a solid surface have been used as a model system for the quantitative study of droplet reaction rates. As the three-phase contact line of surface droplets is pinned by the solid surface, these droplets are stable on the substrate as the reactant is supplied in a controlled flow [4, 165, 166]. The volume of surface droplets is conveniently controlled by the solvent exchange method [96]. The enhanced gas production

rate in smaller surface droplets has been revealed recently from the growth rate of hydrogen nanobubbles as the product [39]. In particular, the bubble growth rates scaled with the droplet radius R with a power law R^{-n} with n from 0.7 to 2.4. Literature reported the applications of reacting surface nanodroplets in the fabrication of surface-bound nanomaterials and surface-enhanced Raman spectroscopy (SERS) [77, 167].

As chemical acceleration is mainly attributed to the important impact from physical and chemical properties of the interface, the enhancement may be expected to decay to a certain extent with the distance away from the droplet surface. A remaining question is whether the reaction rate inside the droplets is uniform spatially. In this work, we will focus on the local reaction rate inside femtoliter droplets. The growth rate of hydrogen bubbles from a gas-generating reaction in droplets will be followed by confocal microscopic imaging. In theoretical analysis of the local reaction rate, we take into account the reactant diffusion, chemical reaction equilibrium, and gas consumption by other bubbles coexisting in the droplet. To the best of our knowledge, our experimental results provide direct evidence that the chemical kinetics and mass balance in the reacting microdroplets are not spatially uniform. These findings may help us to better understand the biphasic reaction kinetics of gas evolution reaction of microdroplets and to design and control droplet reaction in nanomaterials fabrication, heterogeneous catalysis, and in-demand hydrogen bubble production.

5.2 Experimental

5.2.1 Chemicals and materials

Methylhydrosiloxane (Sigma Aldrich) was the reactive liquid in the droplets. Octanol ($\geq$95%, Fisher Scientific) was the non-reactive liquid in a binary droplet. Sodium hydroxide (NaOH) ($\geq$97%, Alfa Aesar) acted as the catalyst for the gas-evolution reaction between siloxane droplets and water in the surrounding. All chemicals were

used as received without any further purification. Water (18.2 MΩcm) was purified by a Milli-Q purification unit (Millipore Sigma).

High precision cover glasses (60 mm length, 24 mm width, Azer Scientific) were hydrophobilized with 3-aminopropyl triethoxysilane (APTES) (≥98%, TCI America) and octadecyl trichlorosilane (OTS) (≥95% Fisher Scientific) by following protocols in the literature [128, 168, 169]. Before use, hydrophobized glass substrates were sonicated in water and ethanol successively for 3 minutes and then dried in a stream of air. The surface tension of the droplet liquid $\sigma_{liq-air}$ was tested with the drop shape analyzer (DSA-100, Kruss). The contact angle θ of surface microdroplets on different substrates were constructed from 3D images collected from a scanning laser confocal microscope (Leica Stellaris 5) through 20× objectives (0.60 NA). Table 5.1 and 5.2 list relevant physical properties of droplet liquids and contact angle of surface droplets θ on various types of the substrates. Droplet formation and chemical reactions were conducted at the room temperature of $\sim 21°C$.

Table 5.1: Physical properties of liquids used in droplet formation

Liquid (vol)	$\sigma_{liq-air}$ (mNm^{-1})	Viscosity μ (mPa·s)
Water	69	1
Siloxane	19	$15 \sim 30$
Octanol	21	9

5.2.2 Formation of surface microdroplets of reactive liquid

Surface microdroplets were prepared within a well reactor as sketched in Figure 5.1A. The well reactor consisted of a piece of the glass substrate and a silicone rubber spacer. The well was 14 mm in both length and width, and 3 mm in depth. Surface microdroplets were formed by the standard solvent exchange process where the solution of droplet liquid (Solution A) was displaced by a poor solvent for droplet

Table 5.2: Contact angle of femtoliter droplets on the substrates used in our experiments

Droplet liquid	Substrate	θ (°)
Siloxane	1	$\sim 26(\pm 6)$
Siloxane	2	$\sim 31(\pm 5)$
Siloxane	3	$\sim 68(\pm 9)$
Siloxane + Octanol	3	$\sim 32(\pm 7)$
Siloxane + Octanol	4	$\sim 23(\pm 5)$

liquid (Solution B). In our experiments, Solution A was 1 vol% siloxane in acetone ($\geq$99.5%, Fisher Scientific). Solution B was water.

During the solvent exchange, the well was initially filled with 200 μl of Solution A. Then a micropipette was used to add 200 μl of solution B into the well at a rate of 2 drops per 10 s. Then 200 μl of the liquid was removed from the well by a micropipette at the same rate. Due to the solubility gap of siloxane in acetone and water, siloxane droplets nucleate from oversaturation, both in bulk and on the substrate [96]. Figure 5.1B sketches the formation of surface microdroplets on the substrate. The process of addition-removal of solution B was repeated 4 times till bulk droplets were removed from the well. After bulk droplets were removed, the liquid in the well became clear for bright field imaging. At the completion of the solvent exchange, the liquid in the well was not pure water, but an aqueous solution with a volume of 400 μl contained acetone of $> 6\%$, v/v. The presence of acetone in the surrounding phase was determined by a microvolume ultraviolet-visible (UV-Vis) spectrophotometer (Nanodrop 2000c, Thermo Fisher).

5.2.3 Formation of surface microdroplets of reactive and non-reactive liquids

Binary droplets consisting of octanol and siloxane were prepared on both APTES-coated and OTS-coated substrates. Solution A was 2 vol% octanol and 0.3 vol%

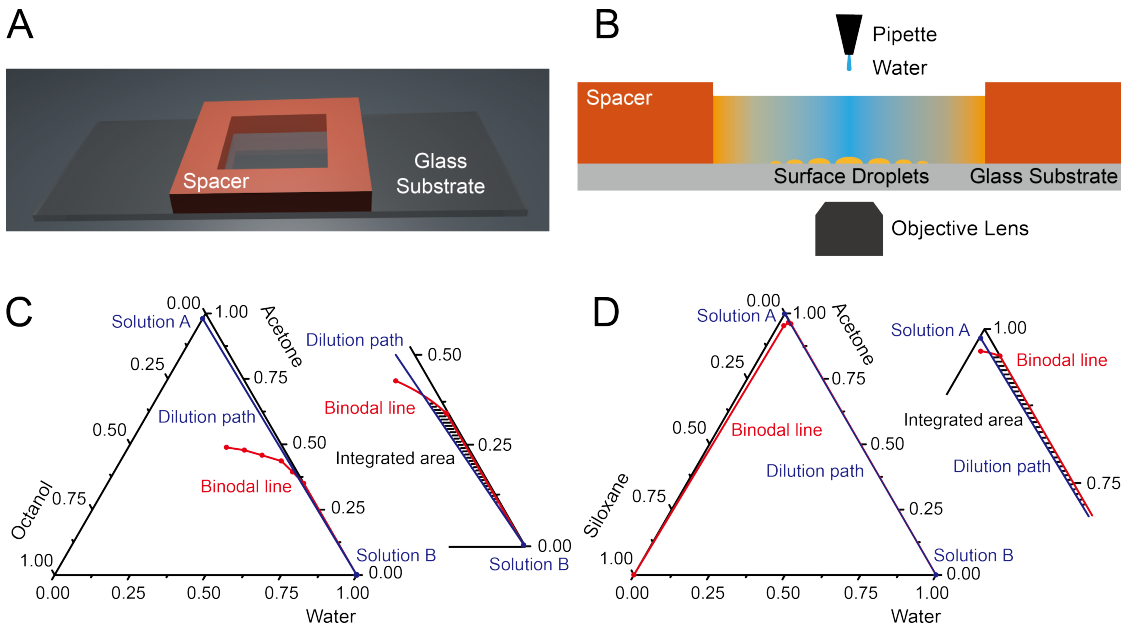

Figure 5.1: (A) The sketch of the well reactor used in our experiments for formation and reaction of droplets. (B) Illustration of preparing surface microdroplets by solvent exchange. (C)&(D) Ternary phase diagrams of (A) Siloxane-acetone-water system and (B) Octanol-acetone-water system. Points labelled as solution A&B are respectively the composition points of solution A&B. Black shaded areas surrounded by binodal lines (red) and dilution paths (blue) represent the oversaturation of each component in the mixing front.

siloxane in acetone solution. A trace amount of fluorescence dye rhodamine 6G (R6G, ~ 5 μM) was added into Solution A for visualization by confocal imaging. Solution B was water. The solvent exchange was performed in the well reactor by following the same procedure as above to form binary droplets on the substrate. By the end of the solvent exchange, the concentration of acetone in the solution inside the well was around 6% (v/v), and the volume of the solution was controlled to be at 400 μl.

The composition of binary droplets was predetermined by the oversaturation level of octanol and siloxane during the solvent exchange [108], which could be approximately estimated according to the difference of dilution path and the binodal curve in the solubility phase diagram. The detailed protocol and the analysis were reported in literature [98, 108]. Ternary phase diagrams of octanol-acetone-water and siloxane-acetone-water were prepared by titration and demonstrated in Figure 5.1C&D. The area surrounded by binodal curves and dilution path in the ternary phase diagram represents the overall oversaturation (octanol:siloxane $\sim$ 4:1).

5.2.4 Tracking microbubbles in reacting droplets

50 μl of 0.24 M NaOH aqueous solution was added into the well by a micropipette to trigger the reaction between siloxane and water. The existence of acetone was confirmed to be necessary for the bubble formation by controlled experiments, in which acetone was almost removed by repeating adding water and removing the mixture from the well 12 times.

Laser scanning confocal microscopes (Leica SP5 and Leica Stellaris 5) through 100$\times$ objectives (1.44 NA/1.49 NA) were employed to track the reaction process in-situ. Bright-field images and confocal images of the bubble formation process were respectively recorded with a transmission detector and a hybrid detector. 488/534 nm laser beams were used to excite the dye R6G incorporated in droplets. The pixel sizes of the videos range from 151 nm to 303 nm. The frame rate was 0.77 fps.

Open source PIMS, scikit, and trackPy package for python, combined with ImageJ,

were applied to analyze the images. Droplets and bubbles in the field of view were processed frame by frame by home-built python code. The base areas of hydrogen bubble a_b and reacting droplet A_b were extracted as a function of time t. Time zero (t_0) was defined as the moment when NaOH solution was added to the well. Distance from the center of the bubble base to the three-phase contact line of the droplet D_b was measured by ImageJ. In most experiments, droplets and bubbles on our homogeneous substrates were assumed to keep the shape of a spherical cap without the strong pinning effect. When calculating the average growth rate of hydrogen bubbles, some bubbles in small droplets ($R_b < 5$ μm), and bubbles after coalescence and collapse were not considered.

5.3 Results and discussion

5.3.1 Theoretic local reaction rate in microdroplets

The chemical reaction of siloxane dehydrocoupling is catalyzed by hydroxide from the aqueous phase (Figure 5.2). At first, hydroxide in bulk attacks silicon atoms of siloxane. Then, hydroxide is reformed by consuming water, and hydrogen is liberated. The oversaturation of the hydrogen product inside the reacting droplet leads to the formation and growth of multiple hydrogen bubbles.

The dimensions of a bubble and a reacting droplet are sketched in Figure 5.2B. Base radius of bubble r and droplet R_b were calculated from the base area of bubble a_b and droplet A_b as $r = (a_b/\pi)^{0.5}$ and $R_b = (A_b/\pi)^{0.5}$. The radius of curvature R_s of the droplet was calculated as $R_s = R_b/sin\theta$. Based on the contact angle of the droplet θ, the base radius R_b, the curvature radius R_s, and the distance from the bubble center to the droplet rim D_b, the shortest distance from the bubble center to the droplet surface D_s can also be calculated by the following equation:

$$D_s = R_s - \sqrt{(R_b - D_b)^2 + R_b^2/tan^2\theta}. \tag{5.1}$$

The reaction in our experiments is irreversible. The rate-limiting step in local gas

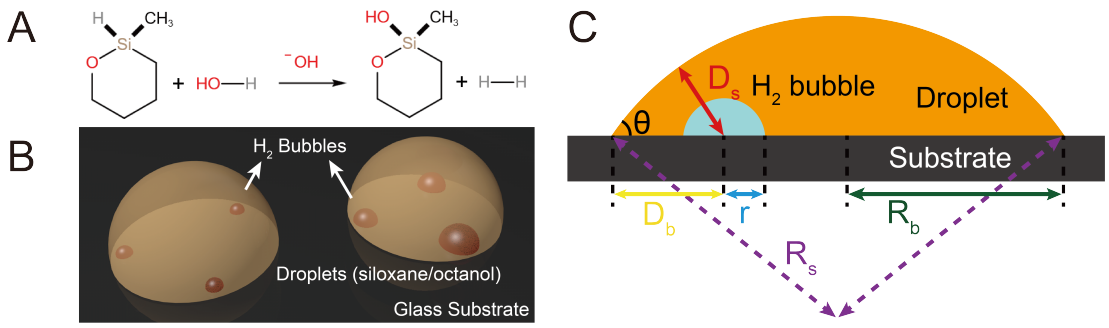

Figure 5.2: (A) The chemical equation of siloxane dehydrocoupling with water. (B) Illustration of hydrogen bubbles formed in droplets. The droplet phase is siloxane or the binary mixture of siloxane and octanol. (C) Base radius of droplet R_b (green) and bubble r (blue), radius of the curvature R_s, contact angle of droplet θ, distance from the bubble center to the droplet rim D_b (yellow) and the droplet surface D_s (red) in the sketch of a surface microdroplet.

production in the droplet is water (the reactant) diffusion into the droplets, a step that determines the location and the rate of the bubbles [170]. Hydrogen produced from the reaction located at the droplet will be discussed in a later section. The reaction with siloxane consumed water and reduced the water concentration in the droplet. The mass balance of water in the droplet consists of the water diffusion and the chemical reaction. To proximate the processes in the droplet, the water concentration profile will be analyzed in the radial direction in a minimal spherical model. The mass balances of water inside the droplet can be given by Fick's law [29]:

$$\partial_t C_w(D_s) = D\nabla^2 C_w(D_s) - k_r C_w(D_s) C_{SiH}. \tag{5.2}$$

∂_t is the time derivative. ∇ is the Nabla operator. D is the diffusion coefficient of the hydrogen in the droplet. $C_w(D_s)$ is the local concentration of water with the distance D_s from the droplet surface. C_{SiH} is the concentrations of siloxane, which can be taken as a constant in the droplet. k_r is the rate constant of the reaction. At the point with distance D_s from the droplet surface, the variation of water concentration $\partial_t C_w(D_s)$ is given by the water diffusion $D\nabla^2 C_w(D_s)$ minus the water consumption by the chemical reaction $k_r C_w(D_s) C_{SiH}$.

Assuming the steady state that water concentration inside the droplet was constant

with time, $\partial_t C_w(D_s)$ was zero and can be neglected in equation 5.2:

$$k_r C_w(D_s) C_{SiH} = D\nabla^2 C_w(D_s). \tag{5.3}$$

Assuming a balanced state that the hydrogen product surrounding the bubble diffuses to the bubble surface and is consumed by the bubble growth, the reaction on the flat substrate surface (boundary condition) can be neglected.

We defined a characteristic diffusion length ϵ as $\sqrt{D/(k_r C_{SiH})}$ to describe the competing effect from water diffusion from the droplet surface and from water consumption by the chemical reaction in the droplet [29]. Solving equation 5.3, we get:

$$C_w(D_s) = C_w(D_s)|_{D_s=0} \frac{R_s \sinh{(R_s - D_s)/\epsilon}}{(R_s - D_s)\sinh{R_s/\epsilon}}. \tag{5.4}$$

Based on equation 5.4, water concentration at a distance D_s to the droplet surface $C_w(D_s)$ is determined by the water concentration nearing the droplet surface $C_w(D_s)|_{D_s=0}$, radius of the droplet curvature R_s, and diffusion length ϵ. From the profile of $C_w(D_s)$ in equation 5.4, the profile of production rate of hydrogen $\dot{m}(D_s)$ throughout the droplet can be given by $\dot{m}(D_s) = k_r C_{SiH} C_w(D_s)$, as:

$$\begin{aligned} \dot{m}(D_s) &= k_r C_{SiH} C_w(D_s)|_{D_s=0} \frac{R_s \sinh{(R_s - D_s)/\epsilon}}{(R_s - D_s)\sinh{R_s/\epsilon}} \\ &= \dot{m}(D_s)|_{D_s=0} \frac{R_s \sinh{(R_s - D_s)/\epsilon}}{(R_s - D_s)\sinh{R_s/\epsilon}}. \end{aligned} \tag{5.5}$$

$\dot{m}(D_s)|_{D_s=0}$ is the theoretical hydrogen production rate nearing the droplet surface. In the above analysis, the profile of hydrogen production rate is obtained along the radial direction inside a spherical droplet. In surface droplets with contact angles much lower than 90°, microbubbles on the substrate are close to the droplet surface than to the center of the sphere. Hence the radial concentration profile from equation 5.5 services a good approximation for the hydrogen supply for microbubbles over the base area of the droplet.

The average bubble growth rate $\dot{r}(D_s)$ can be approximated as proportional to $\dot{m}(D_s)$ in equation 5.5 and can be fit by the same profile:

$$\dot{r}(D_s) = \dot{r}(D_s)|_{D_s=0} \frac{R_s \sinh{(R_s - D_s)/\epsilon}}{(R_s - D_s)\sinh{R_s/\epsilon}}. \tag{5.6}$$

$\dot{r}(D_s)|_{D_s=0}$ is the theoretical average growth rate of the hydrogen bubble nearing the droplet surface.

5.3.2 Growing microbubbles in reacting surface droplet

The contact angle of the reacting droplets constructed from 3D confocal images were respectively $\sim 26°(\pm 6°)$ (Figure 5.3A&B) and $\sim 31°(\pm 5°)$ (Figure 5.3D-F). After introducing NaOH solution into the reactor, microbubbles nucleate throughout reacting droplets. The radius of microbubbles ranges from a few hundred nanometers to several microns. The identity of in-droplet bubbles was verified by varying the focal plane. Screenshots in Figure 5.3A&B show the continuous growth of bubbles inside two large droplets with the base radius R_b of 9.8 μm and 7.5 μm. Figure 5.3D-E show hydrogen bubbles grow in small droplets with R_b less than 4 μm. The number of bubbles is much higher in a larger droplet.

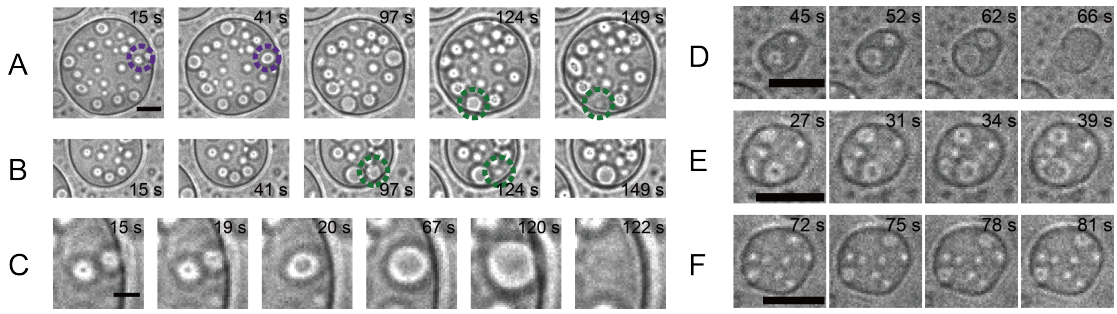

Figure 5.3: (A)&(B) Screenshots of hydrogen bubbles in siloxane droplets with the base radius of 9.8 μm (A) and 7.5 μm (B). Purple circles and green circles denote where bubbles coalesce and collapse. (C) Zoom-in of two bubbles in (A) from coalescence to detachment. (D)-(F) Screenshots of hydrogen bubbles in droplets with the base radius of 1.8 μm (A), 2.2 μm (B), and 2.8 μm (C). The length of scale bars in (A)(B)(D)(E)(F) are 5 μm, and in (C) is 2 μm.

As bubbles grew with time, more of the droplet base area was taken up by bubbles. Two adjacent bubbles may coalesce and merge into a larger bubble. The elliptical morphology of bubbles after coalescence suggests that bubbles are pinned by the substrate due to the slow relaxation in the viscose droplet. For large bubbles with the base radius r larger than 2 μm near the droplet rim, they may collapse and detach

from the substrate. Figure 5.3C enlarges two representative bubbles in Figure 5.3A from coalescence to detachment. The collapse of the bubble near the rim may be due to the rapture of the oil thin film between the bubble and the aqueous phase outside the droplet [39]. More quantitative study of bubble coalescence and bubble detachment on the solid surface was reported in previous work [171].

For multiple bubbles in a droplet, bubbles around the droplet rim grew faster than those near the droplet center. For example, from t =15 s to t =97 s in Figure 5.3A&B, bubbles at the droplet rim became $\sim$ 40% larger in base radius, while bubbles far from the droplet rim remained almost the same size. In Figure 5.4A&B, the base radius of bubbles r was plotted as the function of t. We approximate that bubbles grew linearly and calculate the average growth rate of each bubble by linear fitting. The distance from the bubble center to the droplet surface D_s was also calculated by equation 5.1. Figure 5.4C&D show that the bubble growth rate decreases with the increase in D_s. The experimental data can be well fitted with the theoretic model.

On the APTES-Si substrate where the contact angle of droplets was $\sim 31^\circ(\pm 5^\circ)$, bubbles in seven small droplets with R_b ranging from 1.8 μm to 4.0 μm were followed with time. The average growth rates of bubbles were approximately calculated by linear fitting, and plotted as a function of D_s in Figure 5.4E. Overall the influence from D_s in small droplets was relatively trivial. Figure 5.4F shows that the growth rate of bubbles increased with the decrease in the droplet size.

Table 5.3 summarize the parameters ϵ and $\dot{r}(D_s)|_{D_s=0}$ in the theoretical fittings plotted in Figure 5.4C-E. $\dot{r}(D_s)|_{D_s=0}$ is higher in smaller droplets, consistent with the faster growth rate of bubbles in smaller droplets in the same group of experiments. The enhanced reaction rate in smaller droplets was also found and quantitatively analyzed in our previous results [2, 39]. The accelerated bubble kinetics in smaller droplets was attributed to the faster accumulation of the hydrogen product in smaller droplets with a higher surface-to-volume ratio.

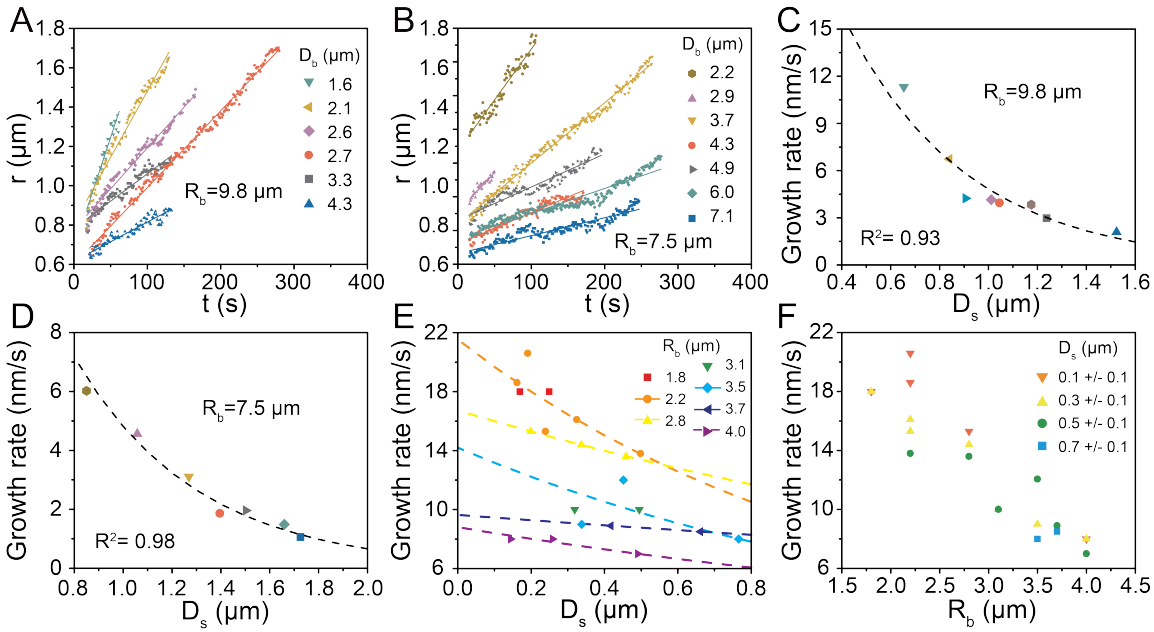

Figure 5.4: (A)&(B) Base radius r of hydrogen bubbles from Figure 5.3A&B as a function of time. (C)&(D) The average growth rate of hydrogen bubbles in (A)&(B) as a function of the distance from the droplet surface to the bubble center D_s. Dashed lines in (C)-(E) are from the fitting of equation 5.6. (E) The average growth rate of hydrogen bubbles as a function of the distance from the bubble to the droplet surface D_s. Bubbles in (E)&(F) are from droplets with the base radius R_b ranging from 1.8 μm to 4.0 μm. (F) The average growth rate of hydrogen bubbles as a function of the base radius of the droplet R_b.

Table 5.3: Fitting parameters ϵ and $\dot{r}(D_s)|_{D_s=0}$ for experimental results from siloxane droplets in Figure 5.4. R_b and R_s are the base radius and curvature radius of the droplet. θ is the contact angle of the droplet. D, k_r, and C_{SiH} are the hydrogen diffusion coefficient in the droplet, rate constant of the reaction, and siloxane concentration in the droplet.

R_b/R_s (μm)	θ (°)	$\epsilon = \sqrt{D/(k_r C_{SiH})}$ (μm)	$\dot{r}(D_s)\|_{D_s=0}$ (nm/s)
9.8/22.4	$\sim 26° \pm 6°$	0.5	34
7.5/17.1	$\sim 26° \pm 6°$	0.5	36
4.0/6.1	$\sim 31° \pm 5°$	1.7	9
3.7/5.6	$\sim 31° \pm 5°$	3.4	10
3.5/5.3	$\sim 31° \pm 5°$	1.2	14
2.8/4.3	$\sim 31° \pm 5°$	1.8	17
2.2/3.4	$\sim 31° \pm 5°$	1.0	22

5.3.3 Bubble formation in high contact angle droplets

Both surface coating and the liquid composition in the droplet were varied to provide three different contact angles in our experiments from 23° to 68°. On an APTES-Si substrate where siloxane droplets were produced with the contact angle of $\sim 68°(\pm 9°)$, bubbles were found to exclusively nucleate at the droplet rim. As shown in Figure 5.5A, a necklace of microbubbles developed around the rim of the droplet in contact with the basic solution. For small droplets with the base radius R_b less than 2 μm, as in Figure 5.5B, only one or two bubbles in most cases can be accommodated in a droplet. Screenshots in Figure 5.5C demonstrates the evolution of bubbles in a representative droplet with $R_b =$ of 12.3 μm.

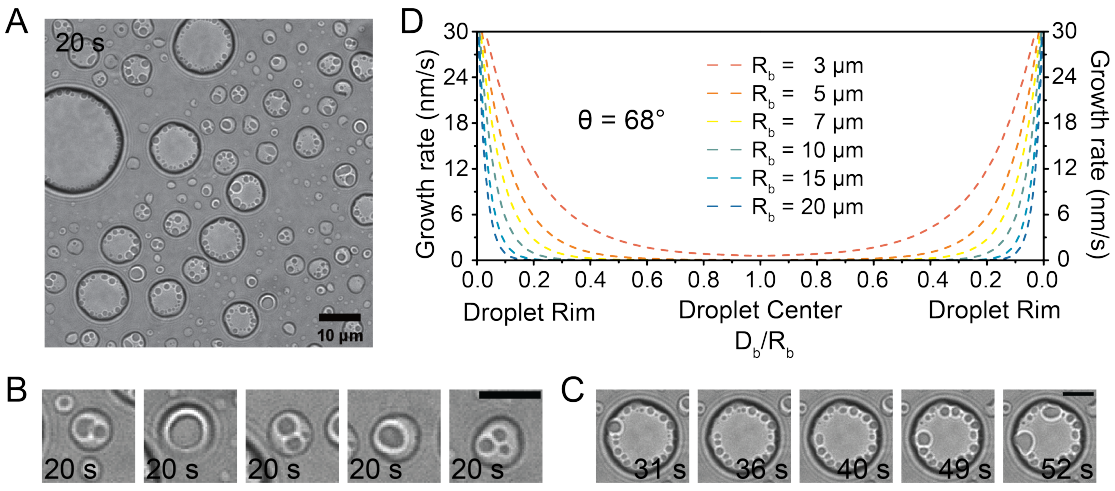

Figure 5.5: (A) Hydrogen bubbles in siloxane droplets with the contact angle of $68°(\pm 9°)$. (B) Zoom-in of small droplets ($R_b < 3$ μm) from (A). (C) Screenshots of hydrogen bubbles grew in a siloxane droplet with the base radius of 12.3 μm. Scale bars in (B)&(C) were 5 μm. (D) Theoretical average growth rate profile of hydrogen bubbles crossing the droplet base. The contact angle θ was taken as 68 °. ϵ and $\dot{m}(D_s)|_{D_s=0}$ were taken as 0.5 μm and 34 nm/s, same the fitting parameters in Figure 5.4C.

From equations 5.1&5.6, $\dot{r}(D_s)$ was approximately estimated as a function of normalized distance to the droplet rim D_b/R_b crossing the droplet base, as shown in Figure 5.5D. The contact angle of droplets was taken as 68°. ϵ and $\dot{r}(D_s)|_{D_s=0}$ were set as 0.5 μm and 34 nm/s, same as the fitting parameters in Figure 5.4C. Apart

from droplet with R_b of 3 μm, $\dot{r}(D_s)$ rapidly decease below 1 nm/s before reaching the droplet center. Taking a droplet with the base radius R_b of 10 μm as the example, $\dot{r}(D_s)$ already decreased to 0.14 nm/s at D_b/R_b of 0.3, suggesting an extremely low water concentration and slow reaction rate at $D_b = 3$ μm. It may take a long time for hydrogen to reach the concentration level for bubbles to nucleate at such a slow reaction rate. The rapid decrease in water concentration inside droplets with high contact angles explains why bubbles only nucleate and grow at the droplet rim.

5.3.4 Growing bubbles in binary droplets

Screenshots in Figure 5.6A&B demonstrate the bubble growth in binary droplets. The contact angle of binary droplets were $32°(\pm 7°)$ in Figure 5.6A and $\sim 23°(\pm 5°)$ in Figure 5.6B. R_b of the binary droplets were 22 μm and 9.0 μm. Similar to bubbles in pure droplets shown in Figure 5.3, bubbles nucleated and grew throughout binary droplets. Figure 5.6C&D respectively demonstrate hydrogen bubbles close to the droplet rim and at the droplet center. The lifetime for a bubble at the droplet rim is usually less than 10 seconds from nucleation to detachment, much shorter than that of inner bubbles. Figure 5.6E&F present sizes of several representative bubbles with different D_b to the droplet rim. Bubbles at the droplet rim grow much faster than bubbles at the droplet center.

Average growth rates of bubbles are plotted as a function of D_s in Figure 5.6G&H. Although data points were scattered in binary droplets, the overall trend was that there was a strong dependence of growth rate on D_s. On the other hand, even the siloxane concentration in binary droplets was lower, the growth rate of bubbles near the droplet rim can go up to $\sim$ 50 nm/s, much faster than bubble growth in pure siloxane droplets. As a result, both bubble coalescence and bubble detachment were more frequent in binary droplets than in pure droplets.

Dashed lines in Figure 5.6G&H are the fittings of experimental results by our theoretic model. Table 5.4 summarize the fitting parameters ϵ and $\dot{r}(D_s)|_{D_s=0}$ of

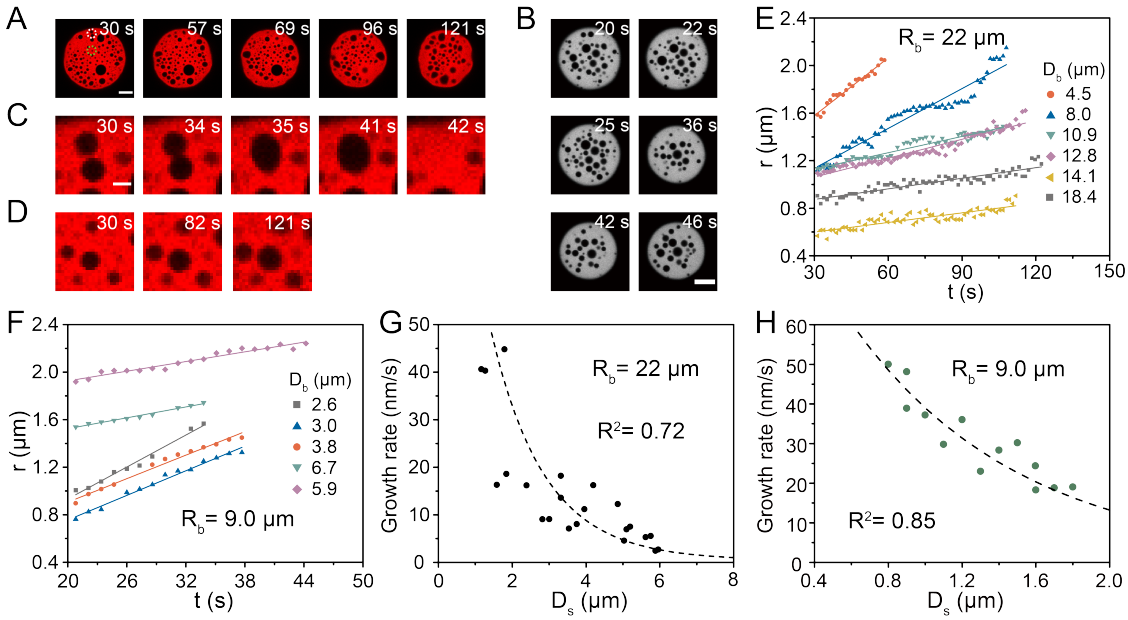

Figure 5.6: (A)&(B) Bubbles grow in a binary droplet on an APTES-Si substrate (A) and an OTS-Si substrate (B). The base radius of the droplet R_b are 22 μm in (A) and 9.0 μm in (B). The contact angle of binary droplets on the substrate were (A) $\sim 32°(\pm 7°)$ and (B) $\sim 23°(\pm 5°)$. The scale bars are (A) 10 μm and (B) 5 μm. (C)&(D) Zoom-in images of hydrogen bubbles at the droplet rim (C) and the droplet center (D). (C)&(D) are taken from the white and green circle in (A). The scale bar for (C)&(D) in (C) was 2 μm. (E)&(F) Base radius r of several representative hydrogen bubbles from (A)&(B) as a function of time. (G)&(H) Average growth rate of hydrogen bubbles from (A)&(B) as a function of distance to the droplet surface D_s. Dashed lines in (G)&(H) are from the fitting of equation 5.6.

binary droplets. Corresponding to experimental results that bubble kinetics in binary droplets was faster than in pure droplets, $\dot{r}(D_s)|_{D_s=0}$ was also found to be higher than that of pure droplets. The accelerated bubble kinetics in binary droplets was probably from the increased water solubility with the addition of polar octanol into the droplets. Higher water concentration in the droplet contributes to a faster chemical reaction rate.

Table 5.4: Fitting parameters ϵ and $\dot{r}(D_s)|_{D_s=0}$ for experimental results from octanol-siloxane binary droplets. R_b and R_s are the base radius and curvature radius of the droplet. θ is the contact angle of the droplet. D, k_r, and C_{SiH} are the hydrogen diffusion coefficient in the droplet, rate constant of the reaction, and siloxane concentration in the droplet.

R_b/R_s (μm)	θ ($^\circ$)	$\epsilon = \sqrt{D/(k_r C_{SiH})}$ (μm)	$\dot{r}(D_s)\|_{D_s=0}$ (nm/s)
22.0/41.5	$\sim 32^\circ \pm 7^\circ$	1.2	143
9.0/23.0	$\sim 23^\circ \pm 5^\circ$	0.8	137
7.4/18.9	$\sim 23^\circ \pm 5^\circ$	0.9	154

5.3.5 Further discussion: On-droplet and in-droplet hydrogen production

The reaction in our experiments can certainly take place on the surface of the droplets, due to abundant siloxane, water and the catalyst in the surrounding. On-droplet hydrogen is expected to be limited in amount. Moreover, the molecules at the interface may react even more readily to react [157–159, 163]. Many reactions that almost do not happen when reactants are located in immiscible phases can occur at the interface. However, the number of interfacial molecules is at least 2 orders of magnitudes less than the number of molecules inside a droplet with a typical size in our experiments [4]. Although the production rate of hydrogen from the interfacial reaction is expected to be faster thanks to the faster reaction rate, the low number of interfacial molecules at any given time limits the total amount of gas production. The hydrogen diffusion in organic liquids is faster than in water, due to the hydrogen bond between hydrogen

with water molecules [172]. It is expected that hydrogen produced in the droplets may reach a certain constant concentration in the droplet at equilibrium with hydrogen dissolved in the surrounding area in a short time, the small dimension of the droplets (especially in the height).

In addition to hydrogen from on-droplet production, the in-droplet production of hydrogen analyzed in our model is attributed to water (carrying the catalyst) diffusing into the droplets. In-droplet water reacts with siloxane to produce hydrogen locally in the droplets. We note that the presence of co-solvent acetone in the system can increase the solubility of water in the droplets and enhance in-droplet hydrogen concentration from the reaction inside the droplets. To a certain extent, even for pure siloxane droplets in absence of acetone, it may be impossible to fully eliminate diffusion of water into reactive droplets as the droplet surface is not impermeable.

A final note is that in-droplet reaction may drive continuous intake of water into droplets, in contrast to the equilibrium from the pure partition where the intake of water is limited by the solubility of water in droplet liquid. The reason is that free water is chemically converted in fast in-droplet reactions, compared to the slow mass transfer of water. The concentration of water may not reach the solubility limit in the droplet. The mechanism is similar to what was reported in the latest work on acid-base reactions, and is the reason why the droplet sensing can achieve very high sensitivity [173, 174].

5.4 Conclusion

In summary, the growth rate of hydrogen microbubbles as the gas product was quantified to report the reaction rate inside the microdroplet. The dependence of bubble growth rate on the location inside the droplets, and on the size, morphology and composition of the droplets all suggest that the reaction rate inside microdroplets may be spatially non-uniform. In our theoretical analysis, diffusion of reactant (water) into the droplets is considered to be the rate-limiting step in bubble growth. The

predicated local gas concentration is in good agreement with the effects from droplet size, substrate wettability and the composition of binary droplets.

Understandings of in-droplet bubble formation may lay a foundation for exploring droplet reactions with enhanced chemical kinetics and generation of gas products. Moreover, nanobubbles encapsulated in surface droplets may lead to a new pathway to functional slippery surfaces to reduce the surface friction [175], porous surface-bound materials by templating nanobubbles [176], or coated bubbles used in biomedical imaging, and therapeutic delivery of oxygen or other pharmaceutical compounds[177, 178].

Chapter 6

Surface nanodroplet-based nanoextraction combined with offline analytic methods for detection and quantification

6.1 Introduction

Reliable detection and analysis of chemicals is crucial in many areas including water pollutant detection [41, 42], air quality monitoring [43, 44], analysis of drugs and pharmaceuticals [45, 46], biological sensing [47, 48], and food quality control [49–51]. To enhance the detection sensitivity, the compounds of interest are often pre-concentrated using an extractant material. Liquid-liquid microextraction has been widely used to achieve this purpose. In a liquid-liquid microextraction, a small volume of non-soluble extractant droplet is exposed to the sample to selectively extract the target chemicals by chemical partitioning [179]. The high surface area-to-volume ratio of the extractant droplet allows efficient mass transfer across the droplet-sample interface [4, 71].

Among various liquid-phase microextraction processes [59, 180–182], dispersive liquid-liquid microextraction (DLLME) is one of the most widely used methods for sample preconcentration owing to its simplicity and high extraction efficiency [59, 60]. In a typical process of DLLME, emulsion droplets are spontaneously formed

upon mixing of a water-immiscible extractant, a dispersive cosolvent, and an aqueous solution of the target analyte [60]. Due to the high partition coefficient of the extractant, target analytes are extracted from the aqueous phase to the extractant droplets. The droplets are separated and collected from the bulk phase and analyzed by sensitive methods such as gas chromatography-mass spectrometry (GC-MS) [51, 67], high-performance liquid chromatography (HPLC) [68, 69], ultraviolet–visible spectroscopy (UV-Vis) [70], and atomic absorption spectrometry [42]. Despite the excellent extraction performance and simplicity, DLLME often uses environmentally harmful extractants such as chlorobenzene, chloroform and carbon tetrachloride, and consumes lots of dispersive solvents, such as methanol and alcohol [60, 183, 184]. Additionally, emulsion droplets need to be separated and collected from the bulk by using separation equipment.

Surface nanodroplets serve as an effective platform to address several drawbacks of liquid-liquid extraction. Surface nanodroplets are femtoliter droplets formed on a solid surface by the solvent exchange method in which a ternary mixture of solvent, antisolvent, and oil (i.e. extractant) is replaced by fresh antisolvent. As the fresh antisolvent replaces the ternary mixture, the oil becomes oversaturated that lead to nucleation and growth of the surface nanodroplets on a target substrate [96]. The solvent exchange method enables controlled formation of the nanodroplets over a large area that has led to applications in various fields such as chemical reaction,[1, 173] chemical analysis,[116] and optics to name but a few.[185]. Recently, the capability of surface nanodroplets to extract target analytes from various samples[77] was leveraged for the quantification of acids in beverages[17, 173] as well as for the detection fluorescent compounds from dense suspensions [80].

However, although the surface nanodroplets are highly efficient for extraction, the fact that they are pinned on a substrate and that the volume of each nanodroplet is on the femtoliter scale make the collection of these nanodroplets extremely challenging by conventional methods such as centrifugation. While in situ methods such as surface-

enhanced Raman spectroscopy (SERS) [77] or optical microscopy [80] can be employed for analysis during extraction, a method to collect the droplets would greatly expand the applicability of surface nanodroplet-based extraction method as it would enable the use of offline analytical techniques such as GC-MS, HPLC, UV-Vis, and others.

In this work, the formation of surface nanodroplets and droplet extraction were performed in a 3-meter hydrophobic capillary tube. After extraction, enough surface nanodroplets (total volume ≥ 2 μL) were collected from the capillary and analyzed by UV-Vis. The extraction performance was evaluated using two common pollutants, e.g. triclosan and chlorpyrifos, and optimized by varying the total volume of the sample solution and for sub-milliliter samples. The process of droplet formation and extraction were sped up by increasing the sample flow rate. The flexibility of the method was also tested by coupling with GC and fluorescence microscopy. The approach reported in our work is environmental friendly, as no harmful or toxic solvent is required and a limited quantity of solvents are needed during the entire process of droplet formation, nanoextraction, and droplet collection. Although the extraction in microfluidic devices is already known and studied extensively, the novelty of our method is stationary nanodroplets immobilized on the inner wall, which allows extraction of an analyte from a large volume of the sample solution and enables highly efficient extraction and enrichment.

6.2 Methodology

6.2.1 Chemicals and materials

Ethanol (≥89%, Fisher Scientific) was used as the cosolvent for droplet formation. 1-octanol (≥99%, Fisher Scientific) was selected as the droplet liquid/extractant. Triclosan (≥98%, TCI America), chlorpyrifos (AR, Sigma Aldrich), and Nile red (≥99%, Acros Organics) were selected as the analytes for droplet extraction. All chemicals were used as received without any further purification. Water (18.2 MΩcm)

was obtained from a Milli-Q purification unit (Millipore Sigma).

Droplet formation and extraction were performed in a 3-meter Teflon capillary tube (Millipore Sigma) with an inner diameter (ID) of 0.8 mm and an outer diameter (OD) of 1.58 mm. Before use, water and ethanol were successively injected into the capillary tube for cleaning. After cleaning, the capillary tube was dried by injecting a stream of air.

6.2.2 Droplet formation and nanoextraction

Droplet formation and Surface nanodroplets were produced on the inner wall of the Teflon capillary by the solvent exchange process. Figure 6.1A sketches the setup in which two shut-off valves and a T-junction were used to connect the tube and the syringe. The valves and T-junction were used to prevent trapping air and guarantee the mixing of two solutions. The solutions were injected into the tube with a constant flow rate by a syringe pump (New Era, NE-1000). When injecting solutions into the tube, only the valve to the tube was open. If the air was trapped during the exchange of the syringes, the valve to the tube was closed and the valve to the waste was opened to remove the air.

During the solvent exchange, a solution of the droplet liquid (Solution A) in the capillary tube was displaced by a water sample with dissolved analytes (Solution B) which should be a poor solvent for the droplet liquid. In our experiments, Solution A was 3.5 vol% octanol in water/ethanol mixture (1:1, v/v). Solution B was the water sample with 0.04 vol% octanol and the dissolved analytes. For samples with chlorpyrifos as Solution B, the solutions also contain 0.05 vol% ethanol. As sketched in Figure 6.1B, octanol surface nanodroplets nucleated out and grew on the inner wall of the capillary due to the solubility gap of octanol in Solution A and Solution B. Figure 6.1C demonstrates an optical image of octanol surface nanodroplets formed on the capillary wall (Nikon H600L, 4× objective lens).

Figure 6.1D illustrates the extraction of analytes from solution B into the octanol

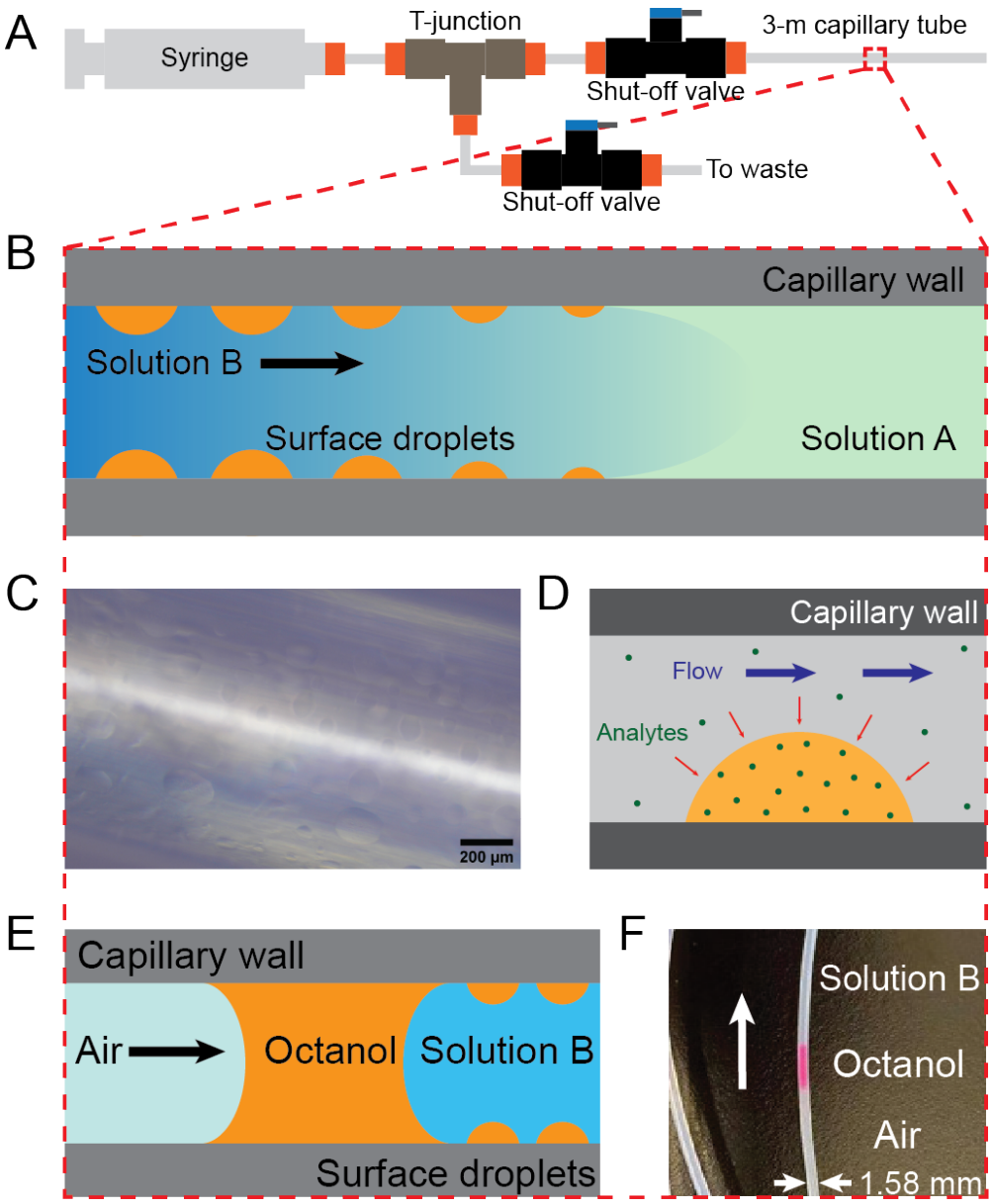

Figure 6.1: (A) Schematic of the experimental setup for droplet formation and extraction. (B) Schematic of the droplet formation on the inner wall of a teflon capillary tube by the solvent exchange process. (C) An optical image of octanol droplets on the inner wall of a capillary tube. (D) A sketch showing the extraction process of analytes into a surface droplet by flowing the sample solution in the capillary tube. (E) Schematic of octanol collected by the capillary force between water and air. (F) The image of octanol collected in the capillary tube.

surface nanodroplet, at the same time as droplet formation by the solvent exchange process was taking place. Due to the pinning effect of surface droplets on the capillary wall, the nanodroplets were stable and could not be removed by the flow of Solution B. After injecting ~ 1.6 mL solution B into the tube, most of the ethanol was removed and the solvent exchange was almost finished that droplets would not grow further. At this point, the injection of sample solution can be stopped or continued for further extraction.

6.2.3 Sample collection and detection

After the extraction of analytes from the sample solution, air was slowly introduced into the capillary tube by the syringe pump. The flow rate of the air was kept at 5 mL/h. Due to the capillary force, octanol droplets with the extracted analytes can be collected between water (i.e. Solution B) and air, as illustrated in Figure 6.1E. Figure 6.1F shows an image of collected octanol between air and water sample. With Nile red extracted from the water sample, the collected octanol appeared in red in the screenshot.

After all of the water sample was pushed out by air, ≥ 2 μL of the octanol sample containing the analytes could be collected for analysis. A microvolume ultraviolet-visible (UV-Vis) spectrophotometer (Nanodrop 2000c, Thermo Fisher) was used for the detection of triclosan and chlorpyrifos. The UV-Vis spectrum of octanol standards containing target analytes was used to establish a calibration curve from Beer-Lambert law:

$$A = \epsilon b C_d. \tag{6.1}$$

ϵ and b are the molar absorptivity of the analytes and the length of the light path (1 mm). C_d is the concentration of the target analyte in extractant droplets. The calibration curve was then used to determine C_d.

Instrumental analysis was also performed on a gas chromatograph/mass spectrometer Agilent 6890 with 5975B MSD for octanol sample with triclosan. The procedure

is based on a previously published method [186]. Briefly, a HP-5MS GC column was used for the separation. The GC/MS injector and the transfer line temperature were set to 280 and 300 °C, respectively. Temperature program was initiated with 75 °C for 1 min, increased to 230 °C at 10 °C, then to280 °C at 20 °C/min, and held for 15 min. The droplet sample was diluted in dichloromethane (DCM) and the sample injection volume was 2uL. The presence of Nile red in octanol was determined by an optical microscope (Nikon H600L, 4× objective lens).

6.3 Results and discussion

6.3.1 Performance of triclosan extraction

As a commonly used antibacterial and antifungal agent [187, 188], triclosan in the water sample was taken as the model compound. The volume flow rate Q and total volume V of the sample solution were 10 mL/h and 1.6 mL.

The UV-Vis absorbance spectrum of collected octanol nanodroplets after extraction of triclosan is shown in Figure 6.2A. The absorbance peak at 283 nm was found to increase with increasing triclosan concentration in the sample. This is consistent with the characteristic triclosan absorbance peak reported in the literature [189]. Figure 6.2B shows a zoomed-in view of the absorbance spectrum from samples with C_w below 10^{-6} M, plotted together with a control group without triclosan. C_w is the analyte concentration in the sample. The characteristic peak for triclosan is still detectable even from the sample with C_w of 10^{-7} M, and can be easily distinguished from a wide background peak spanning between 270 nm and 280 nm present in the control group. Overlap of the background peak and the characteristic peak at the C_w of 10^{-7} M leads to the highest absorbance appearing at 280 nm. C_w below 10^{-7} M leads to indistinguishable absorbance from the background and the analyte. The absorbance at 283 nm (A_{283}) is plotted as the function of C_w in Figure 6.2C. A linear relationship was found between C_w and A_{283}, as demonstrated by the fitting in Figure 6.2C.

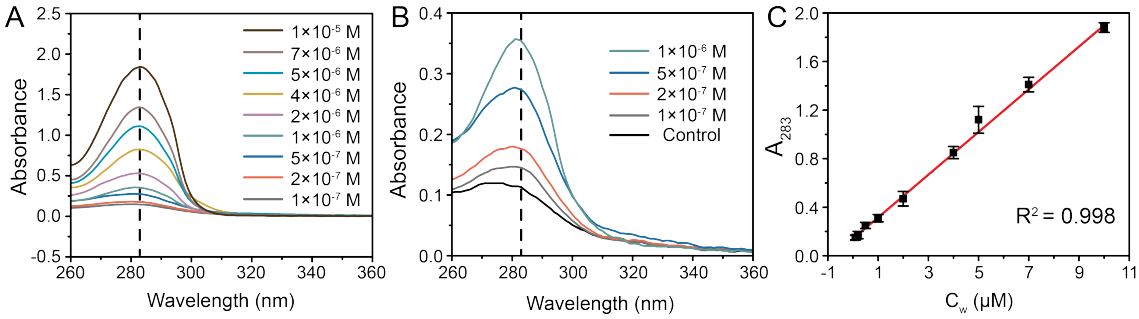

Figure 6.2: (A) UV-Vis absorbance spectrum of collected octanol droplets. The droplets were from samples with analyte concentration C_w of 10^{-5} M to 5×10^{-8} M. Volume flow rate Q and total volume of the sample solution V were 10 mL/h and 1.6 mL. (B) Zoom-in of UV-Vis absorbance in (A). (C) Absorbance at 283 nm A_{283} as the function of C_w. The error bars (standard deviation) are from 3 replicates.

To quantify the concentration of triclosan in the octanol nanodroplets (C_d), the UV-Vis spectrum of triclosan in octanol solutions were obtained as shown in Figure 6.3A. From Beer-Lambert law in Equation 6.1, C_d and A_{283} are linearly correlated as shown in Figure 6.3B. With the linear relationship between C_d and A_{283}, C_d of collected octanol droplets in experiments can be calculated as the function of C_w, as shown in Figure 6.3C. When calculating C_d in the collected droplets, A_{283} contributed from the background was corrected by subtracting A_{283} in the control group. The extraction method was further optimized by varying the sample flow rate and sample volume in the following sections.

The enrichment factor (EF) defined as C_d/C_w was calculated from Figure 6.3C and plotted as a function of C_w in Figure 6.3D. For the sample concentration C_w of 10^{-5} M to 10^{-6} M, the EF fluctuated in a small range from 350 to 410. As the volume of collected octanol was ~ 3 μL for the extraction from the 1.6 mL sample, the recovery of triclosan was estimated to be between 66% and 77%. At the same time, the standard deviation of EF calculated from 3 replicates also increased with the decrease of C_d and became comparable to the average at C_w of 10^{-7} M. The larger error bars at C_w below 5×10^{-7} M contributes to an EF fluctuating in a larger range. The wildly fluctuating EF below C_w of 5×10^{-7} M attributes to the LOD by using

UV-Vis spectroscopy. The quantification of triclosan with extremely low C_w may not be accurate. The consistent EF over a wide range of C_w is key to the quantification of the analyte enriched by nanodroplets.

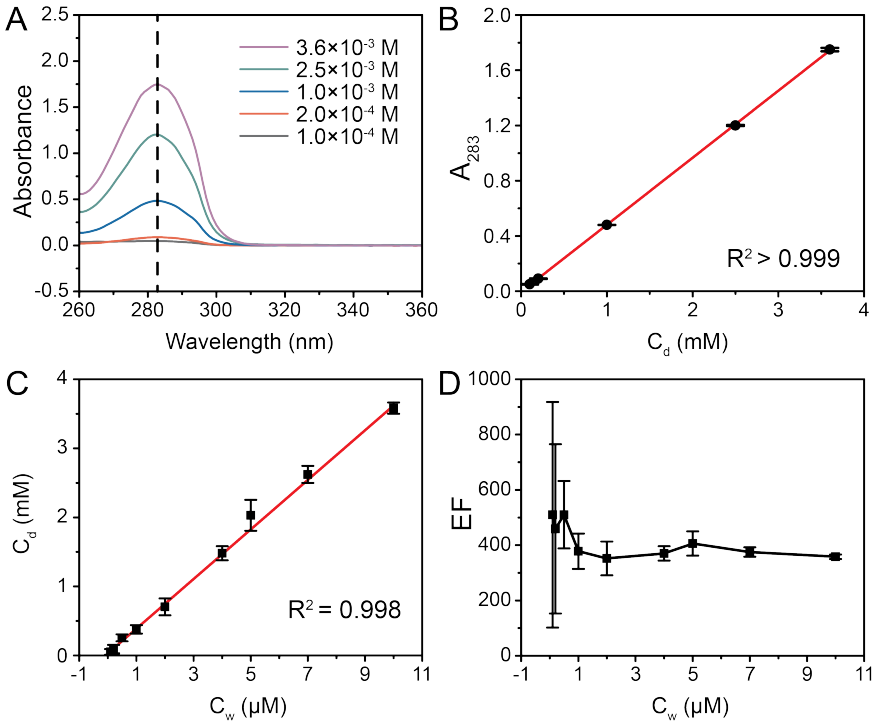

Figure 6.3: (A) UV-Vis absorbance spectrum of triclosan in octanol solutions. The concentration of triclosan in octanol solutions are from 10^{-4} M to 3.6×10^{-3} M. (B) A_{283} as the function of triclosan concentration in octanol droplets C_d. (C) C_d as the function of C_w. (D) Enrichment factor (EF) as the function of C_w.

6.3.2 Effects from volume flow rate Qn the extraction

High reproducibility of the nanodroplet extraction was confirmed at different flow rates of sample solution. A triclosan solution (4×10^{-6} M) with 1.6 mL of volume was used. The flow rate Q of the sample solution was varied from 10 mL/h to 50 mL/h. Figure 6.4A plots the UV-Vis absorbance spectrum of the collected nanodroplets obtained using various flow rates. The characteristic peak of triclosan at 283 nm remained similar as Q increased from 10 mL/h to 50 mL/h. As Figure 6.4B shows, A_{283} only slightly decreases with the increase of Q.

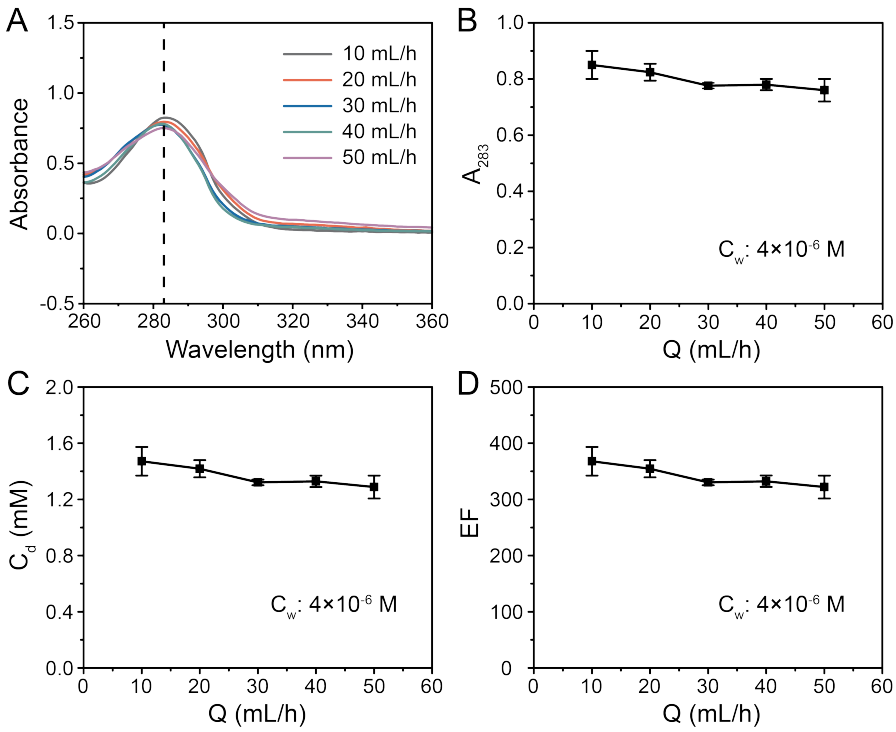

Figure 6.4: (A) UV-Vis absorbance spectrum of collected octanol droplets. The droplets were from extractions with Q from 10 mL/h to 50 mL/h. C_w and V of the samples were 4×10^{-6} M and 1.6 mL. (B) A_{283} as the function of Q. (C) C_d as the function of C_w. (D) EF as the function of C_w.

From results of standard solutions in Figure 6.3A&B, C_d and EF were estimated and plotted as the functions of Q in Figure 6.4C&D. The influence from Q on extraction performance are found to be negligible. Thus, increasing Q can be an effective method to speed up the extraction process without much compromise of the extraction performance. Take the extraction from Q = 10 mL/h and Q = 50 mL/h for instance, the time spent for nanodroplet formation and extraction was reduced from $\sim$ 10 min to $\sim$ 2 min, while A_{283} and EF only decreased $\sim$ 13%.

The independence of enrichment factor on flow rate is related to the consistent droplet sizes in the capillary tube. In a previously published work, the size distribution of surface nanodroplets formed by the solvent exchange was also found to be irrelevant to the flow rate in the capillary [80]. This is in contrast to results on a flat substrate in a flow chamber, in which droplets tend to be larger at a higher flow rate [96]. The geometry confinement in the capillary blocks the effect from the external flow on the mass transfer of the surface droplets, which contributes to the trivial dependence of the extraction performance on the flow rate [80].

6.3.3 Effects from sample volume Vn the extraction

The extraction performance was further studied by varying the sample volume (V). The sample flow rate (Q) and C_w were kept at 10 mL/h and 1×10^{-6} M. After injecting 1.6 mL of triclosan sample solution, only water can be collected at the outlet. All ethanol was removed from the capillary, so that droplet formation stopped. The extraction performance was tested from samples with V up to 10 mL, in which extraction continued after droplet formation. A sample with V of 0.8 mL was also tested, in which the extraction was finished before all ethanol was removed from the capillary. The UV-Vis spectrum of the collected droplets is plotted in Figure 6.5A, reflecting a higher peak with the increase of the sample volume V. Figure 5B shows A283 monotonically increases with V.

From results in Figure 6.5B, C_d and EF were calculated and plotted as the functions

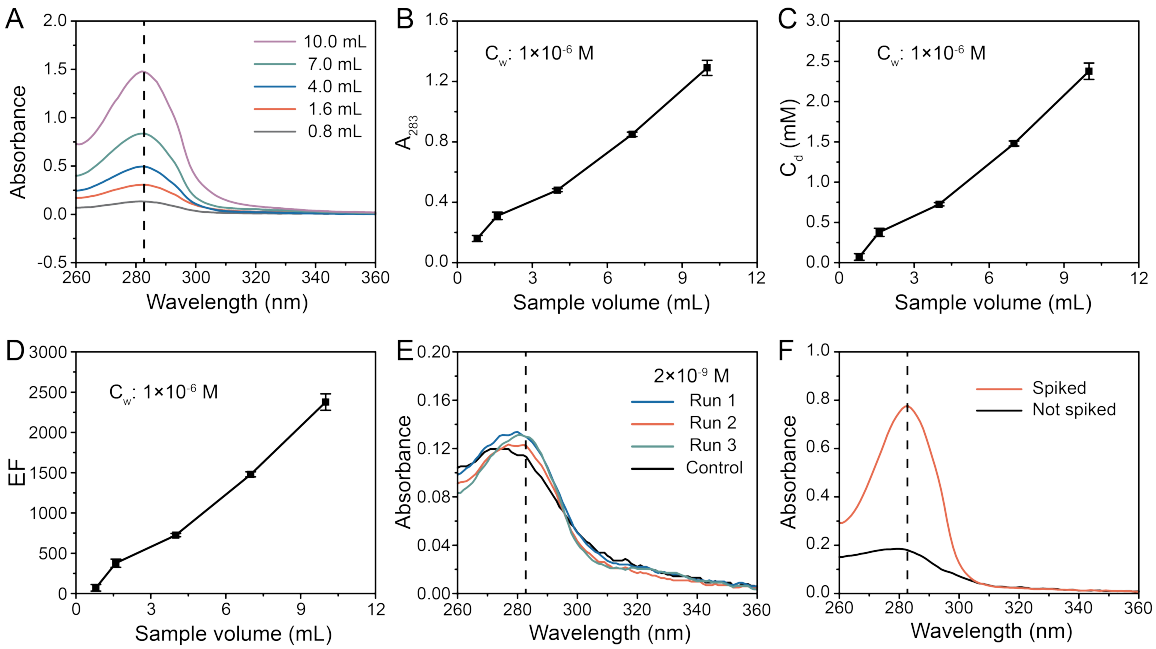

Figure 6.5: (A) UV-Vis absorbance spectrum of collected octanol droplets. The droplets were from extractions with V from 0.8 mL/h to 10 mL/h. Q and C_w were 10 mL/h and 1×10^{-6} M. (B) A_{283} as the function of V. (C) C_d as the function of C_w. (D) EF as the function of C_w. (E) UV-Vis spectrum of droplets extracting 100 mL sample with C_w of 2×10^{-9} M. (F) UV-Vis spectrum of droplets extracting river water (North Saskatchewan River, Edmonton) spiked with $10^{-}6$ M triclosan. Q and V were 30 mL/h and 7 mL.

of C_w in Figures 6.5C&D. Increasing V clearly enhanced the extraction performance reflected by the increase in EF from $\sim$ 400 to $\sim$ 2400 when V increased from 1.6 mL to 10 mL. As only $\sim$ 2 μL octanol were collected at V = 10 mL extraction, the recovery of triclosan was estimated to be $\sim$ 48%. Moreover, signals from a low sample volume of V = 0.8 mL suggest that the droplet extraction in the capillary can also be applied to sub-microliter samples that are not sufficient to finish the solvent exchange. As EF calculated from our experiments is much smaller than the partition coefficient of triclosan between octanal and water (pK_{ow}=4.76), C_d in droplets has not reached equilibrium with C_w in the sample solution even at the highest EF of 2400. Triclosan can be continuously extracted from the sample flow if higher volume is used.

100-mL samples with lower C_w were tested to further enhance the LOD of the detection. As droplets slowly dissolved in the sample flow, we increased the octanol volume ratio in Solution A to 4 vol%, to prevent inaccurate results from the insufficient octanol droplets. As in Figure 6.5E, the LOD was found to be 2×10^{-9} M ($\sim$ 0.58 μg/L), which is comparable to previously published works listed in Table 6.1. We did not further increase the sample volume to improve the extraction performance, as a small enhancement consumes much more sample and extraction time. Additionally, the droplet dissolution from a higher sample volume makes it difficult to collect enough droplets or get reliable results.

It is worth noting that, the standard deviation of C_d and EF calculated from 3 replicates was found to be comparable to the average when C_d is low. The large deviation prevents the sensitive detection and precise quantification of samples at a lower concentration C_w. Based on results from standard solutions in Figure 6.3A&B, the measurement of the equipment did not account for the large deviation of A_{283}. Moreover, as the scale of deviation did not increase monotonically with C_w and C_d, the real concentration of triclosan in droplets C_d were not the only contributor of the deviation of A_{283}. The background also contributed to the large deviation of C_d

Table 6.1: Comparison of the proposed method with other methods

Analyte	Extraction method	LOD (μg/L)	References
Triclosan	IL/IL-DLLME-HPLC-MS/MS	0.23-0.35	[190]
Triclosan	SSME-UV	0.28	[191]
Triclosan	DLLME-SFO	0.1	[192]
Triclosan	SLLME-UV	0.58	This work
Chlorpyrifos	WE-DLLME-GCFID	0.92	[193]
Chlorpyrifos	LLME-HPLC-UV	0.1-0.35	[194]
Chlorpyrifos	SLLME-UV	1.05	This work

IL: ionic liquid; SSME: supramolecular microextraction; UV: ultraviolet; SFO: solidification of floating organic droplet; SLLME: surface nanodroplet-based liquid-liquid microextraction; WE: water emulsion; GCFID: gas chromatography flame ionisation detector

and EF in results. An additional control group with $V = 10$ mL was tested, showing A_{283} from the background is not relevant to V. The background peak at 283 nm was not from contaminants in the sample solution. Figure S1 in supporting materials compares the UV-Vis spectrum from control groups with $V = 1.6$ mL and $V = 10$ mL. A_{283} from the control group can be applied for the correction of C_d in experiments with different V.

The droplet extraction was also performed with river water (North Saskatchewan River, Edmonton) spiked with 10^{-6} M triclosan. Q and V were kept at 30 mL/h and 7 mL. Figure 6.5F compares the UV-Vis absorbance of collected octanol droplets from spiked river sample and controlled river sample.

6.3.4 Performance of chlorpyrifos extraction

The organophosphate pesticide chlorpyrifos was taken as the second model compound for droplet extraction in the capillary [195–197]. The flow rate Q and sample volume V were 30 mL/h and 8 mL, respectively. The concentration of chlorpyrifos in samples C_w was from 10^{-6} M to 2×10^{-8} M. Figure 6.6A shows the UV-Vis spectrums of collected nanodroplets, in which the peaks at 230 nm and 292 nm were identified as

characteristic peaks of chlorpyrifos for quantitative analysis. The absorbances at 230 nm (A_{230}) and at 292 nm (A_{292}) are plotted as functions of C_w in Figure 6.6B, which are found to increase monotonically with C_w. Similar to the results in Figure 6.2B, superposition of the absorbance from the background and chlorpyrifos at a low C_w leads to the highest absorbance moving to a lower wavelength, both for 230 nm and 292 nm. Taking the peak at 292 nm as an example, the highest absorbance shifted to 288 nm in the group of $C_w = 10^{-7}$ M and to 286 nm in the group of $C_w = 2{\times}10^{-7}$ M. Further reducing C_w may contribute to indistinguishable absorbance from the background and the analyte. The LOD ($2{\times}10^{-8}$ M) is one order magnitude higher than the LOD of DLLME coupled with HPLC-UV ($\sim 10^{-9}$ M) in literature [194].

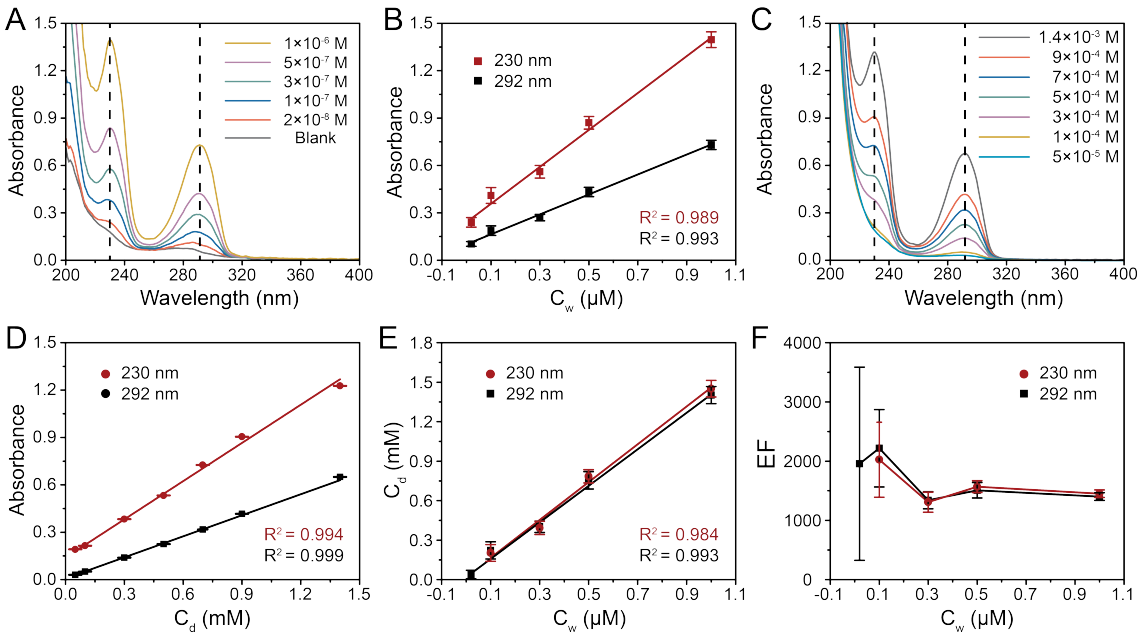

Figure 6.6: (A) UV-Vis absorbance spectrum of collected octanol droplets. The concentrations of chlorpyrifos in samples were from $2{\times}10^{-8}$ M to 10^{-6} M. Q and V were 30 mL/h and 8 mL. (B) A_{230} and A_{292} as the functions of C_w. (C) UV-Vis absorbance spectrum of chlorpyrifos in octanol solutions. The concentration of triclosan in the standard solutions is from $5{\times}10^{-5}$ M to $1.4{\times}10^{-3}$ M. (D) A_{230} and A_{292} as the functions of C_d. (E) C_d as the function of C_w. C_d and EF calculated from A_{230} at C_w of $2{\times}10^{-8}$ were not shown in (E)&(F), as they were calculated as negative after correction with results from the control group. (F) EF as the function of C_w. Red and black dots in (E)&(F) were respectively calculated from results of 230 nm and 292 nm.

Figure 6.6C shows the UV-Vis spectrum of chlorpyrifos in octanol solutions with C_d from 5×10^{-5} M to 1.4×10^{-3} M. From the spectrum of standard solutions, A_{230} and A_{292} were plotted as the functions of C_d in Figure 6.6D. From Beer-Lambert law in Equation 6.1, C_d and EF were respectively calculated from results of A_{230} and A_{292}, and plotted in Figure 6.6E&F. Similar to results in Figure 6.3D, the enrichment factor fluctuated in a small range from 1300 to 1600 at a high C_w above 3×10^{-7} M. When C_w decreased below 10^{-7} M, the enrichment factor fluctuate in a larger range as a result of lower accuracy. The low accuracy at a low C_w was reflected by large error bars in Figure 6.6F. Moreover, results from A_{230} and A_{292} in Figure 6.6E&F are similar to each other, except for the LOD group. The similar results calculated from two wavelengths suggest that the quantitative analysis at a higher C_w is reliable and accurate. The recovery of triclosan was estimated to be between 33% and 40%.

The extraction was performed with 80-mL samples to enhance the LOD of the detection. The octanol volume ratio in Solution A was increased to 4 vol%. Solution B was saturated with octanol before spiked with chlorpyrifos. As in Figure 6.7A, the LOD was enhanced to 3×10^{-9} M (~ 1.05 μg/L), which is comparable to previously published works listed in Table 6.1. The combinative extraction of triclosan and chlorpyrifos was performed by spiking Solution B with two model compounds both at C_w of 10^{-6} M. The sample volume V and the volume flow rate Q were 7 mL and 30 mL/h. In Figure 6.7B, the UV-Vis absorbance of the combinative extraction was compared with the spectrums from single-component extraction. The combination of the characteristic peaks of triclosan at 283 nm and chlorpyrifos at 292 nm leads to a wide peak at 287 nm, demonstrating that multi-components from the sample can be extracted at the same time.

6.3.5 GC-MS and fluorescence analysis of the collected drop

Nanoextraction by surface droplets can be applied in tandem with many common analytic tools for sensitive detection. The extraction of triclosan from water samples

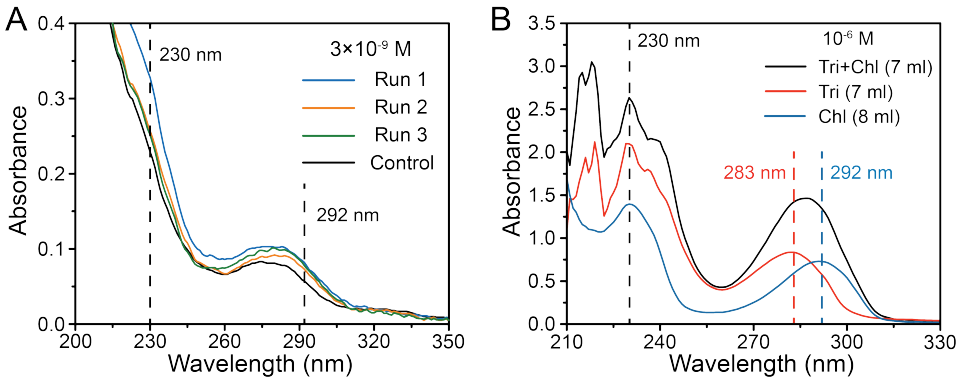

Figure 6.7: (A) UV-Vis spectrum of droplets extracting 80 mL sample with chlorpyrifos of 3×10^{-9} M. (B) Comparing UV-Vis spectrums from the combinative extraction of triclosan and chlorpyrifos and single-component extraction.

(7×10^{-6} M) was also confirmed by coupling with GC-MS. The peak appeared at 16.9 min in Figure 6.8A was identified to be triclosan.

As the final example, a fluorescent dye, Nile red was extracted from a pure water sample and a river water sample. C_w, Q, and V of the sample were 10^{-6} M, 30 mL/h, and 8 mL, respectively. After extraction, a ≥ 2 μL octanol droplet was collected, as in Figure 6.8B&C. An optical microscope with excitation lasers was used to test the fluorescent intensity of the droplet. As shown by the screenshot in Figure 6.8B&C, the maximum light intensity I_{max} of the drops were ~ 110 and ~ 100.

As a control, the same extraction process was performed for pure water (without Nile red). The fluorescence intensity of the collected octanol drop in the control (Figure 6.8C) was less than 8. Therefore, the light intensity of ~ 110 was mainly attributed to the extracted dye. Figure 6.8D show a drop of the water sample with C_w of 10^{-6} M. The fluorescence intensity of the drop was less than 6. The extraction by surface droplets in the capillary tubes can also be used for the detection of fluorescent dyes in water samples.

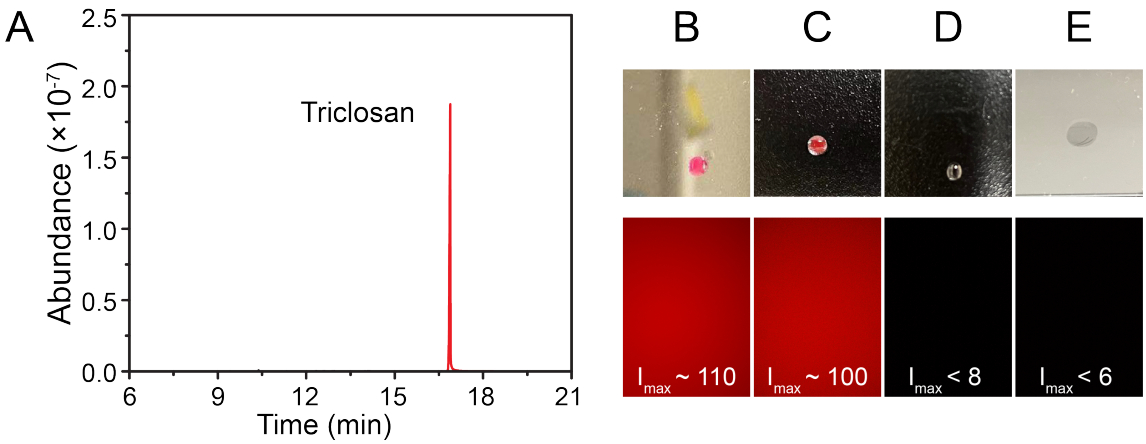

Figure 6.8: (A) GC results of the triclosan extracted by octanol droplets. (B)-(D) One drop (≥ 2 μL) of octanol collected from the extraction of (B) a pure water sample with the Nile red (10^{-6} M), (C) a river water sample with the Nile red (10^{-6} M), (D) a pure water sample without the Nile red, and their images from a fluorescence microscope. (E) One drop of pure water sample with the Nile red (10^{-6} M) and the image from a fluorescence microscope.

6.4 Conclusion

In summary, we demonstrated a cost-saving extraction approach for concentrating and detecting trace amounts of chemical compounds using octanol surface nanodroplets formed inside a long capillary tube. The nanodroplets were produced by solvent exchange using the sample solution as the second fluid. After extraction, nanodroplets could be collected by blowing a gentle stream of air. Due to the small volume and pinning effect, extraction based on surface nanodroplets in previous literature was limited to only a few online analytical techniques such as SERS and fluorescence microscope with limited model compounds. The collection of enough nanodroplets from a long capillary in this work enables offline analysis such as UV-Vis and GC-MS.

The collected nanodroplets were analyzed by UV-vis spectrometry, which revealed a limit of detection of $\sim 10^{-9}$ M and a linear range above 2×10^{-7} M for two representative micropollutants, triclosan and chlorpyrifos, in water samples. Introducing the sample solution with a higher flow rate Q was found to speed up the process of droplet formation and extraction without compromising the extraction perfor-

mance. Nanoextraction in the capillary was also confirmed to be compatible with other common analytical techniques including GC-MS and fluorescence microscopy. The method shown here is powerful for rapid extraction, quantification, and sensitive detection of a wide range of analytes in tandem with offline analytic instruments.

Chapter 7

Conclusions and Future Work

7.1 Conclusions

This thesis presents the kinetics of the biphasic reaction and mass transfer between reacting surface nanodroplets and reactants from the surrounding bulk flow, gas generating reaction and bubble formation within reacting surface nanodroplets, and nanoextraction and sensitive detection by surface nanodroplets.

An experimental method was developed that the surface nanodroplets pinned on the solid surface were followed by microscopy during the reaction. By following the evolution of droplet morphology and droplet size, the reaction kinetics and mass transfer inside or out of the droplet can be reflected by tuning the conditions such as external flow rate, droplet size droplet composition, and substrate wettability. The effects of the factors above can be easily evaluated based on our achieved research progress on surface nanodroplets. With the efficient interface-crossing mass transfer and the pinning effect, this setup can also be an ideal template for liquid-liquid extraction from a sample flow.

By following the neutralization between acidic surface nanodroplets and alkali from an external flow, the effect of the external flow conditions on the reaction kinetics was evaluated in Chapter 3. The reaction rate is measured by droplet shrinkage as the product is removed from the droplets by the flow. We found that the droplet reaction was faster at higher flow rates. Predicted by our theoretical model and confirmed by

the experimental results, the reaction rate scales with $\sim Pe^{1.5}$, in good agreement with our experimental results. The accelerated reaction kinetics was attributed to the enhanced mass transfer of the reactant and the product in a faster flow. The findings above addressed our objective to quantitatively understand the effects of external flow conditions on the kinetics of droplet reaction.

Moreover, the effects of the droplet size and the droplet composition on the droplet reaction were tested by following the same model reaction in Chapter 4. Followed by an optical microscope, the reaction rate was found to be faster in smaller droplets, scales with $\sim R^{-2}$. The faster reaction rate in smaller droplets was attributed to the faster product accumulation in droplets with higher surface-to-volume ratios, and the product diffusion in the Prandtl-Blasius boundary layer. Additionally, the effects of droplet composition on droplet reactions were performed by adding non-reactive components into the droplets, which was found to be relevant to the surface activity and polarity of the non-reactant. The above findings address our objective to quantitatively study the effects of droplet size and droplet compositions on the droplet reaction.

In Chapter 5, we further investigated the local kinetics of in-drop hydrogen generating reaction by tracing the gaseous product-induced bubble formation inside surface nanodroplets. Measured online by high-resolution confocal microscopic images, the dependence of bubble growth rate on the location inside the droplets, and on the size, morphology and composition of the droplets, all suggest that the reaction rate inside microdroplets may be spatially non-uniform. Based on our theoretical model, diffusion of reactant (water) into the droplet is considered to be the rate-limiting step, which was balanced by the reaction inside the droplet. The predicated reaction rate is in good agreement with the effects of droplet size, substrate wettability and the composition of binary droplets. These findings addressed our objective to understand the formation and growth of surface bubbles triggered by the droplet reaction and involved reaction kinetics and mass transfer.

Taking the advantages of the pinning effect and efficient mass transfer of surface nanodroplets, we also demonstrated a cost-saving and versatile extraction approach for concentrating and detecting chemical compounds by coupling various offline analytical techniques. Surface nanodroplets of octanol were produced on the inner wall of a long capillary tube to extract analytes from the sample flow. After extraction, nanodroplets can be collected by blowing a gentle stream of air. The collected nanodroplets were analyzed by UV-vis spectrometry, which revealed a limit of detection of $\sim 10^{-9}$ M and a linear range above 2×10^{-7} M for two representative micropollutants, triclosan and chlorpyrifos, in water samples. The extraction performance and extraction efficiency can be flexibly adjusted by varying the sample volume and sample flow rate. The versatility of the method was confirmed by coupling the method with several offline analytical techniques including UV-Vis, GC-MS, and fluorescence microscopy. The above results addressed our objective to develop the surface nanodroplet as a template for liquid-liquid extraction with versatility and simplified procedures.

Our results advanced the current understanding of droplet reaction kinetics and involved mechanisms of mass transfer. The understanding in this thesis paves the way for designing and controlling biphasic reactions in a broad range of applications, such as droplet-based sensing, heterogeneous catalysis or polymer particle synthesis. Moreover, the excellent properties of surface nanodroplets, such as the pinning effect and efficient interface-crossing mass transfer, enable the detection of trace compounds by permitting fast, reliable extraction and collection of the extractant nanodroplets for offline analysis.

7.2 Future Research

Though great efforts have been conducted in the principles and applications of functional surface nanodroplets in many fields, the developed experimental method and findings enable further research. The topics listed below may be valuable for further research.

(1) At present, our study on the reaction kinetics in surface nanodroplets is limited to the model systems, such as a simple neutralization between organic acid and hydroxide ions. The study on reaction kinetics can be expanded to various types of reactions by employing our experimental setup in Chapters 3&4. For example, the kinetics of catalytic systems with functionalized nanoparticles absorbed on the droplet surface can be further explored. The exploration of various types of droplet reactions may expand our understanding and pave the way for designing and controlling droplet reactions for real applications.

(2) The experimental setup in this thesis and the well-established platform of surface nanodroplets reacting in a reactant flow in Chapters 3&4 may pave the way for the controllable production of porous nanomaterials based on surface nanodroplets. It would be interesting to study if we can control the structure, size, and other physical and chemical properties of nanomaterials by tunning the flow rate and flow geometry, substrate wettability and roughness, droplet size and morphology, and droplet compositions.

(3) The production of hydrogen bubbles in reacting surface nanodroplets can be further enhanced by adding nucleophiles into the droplets, which potentially pave the way for in-demand hydrogen bubble production. Additionally, bubbles encapsulated in the droplets were previously reported to enhance fluorescence detection in droplet extraction. Preparing reactive surface nanodroplets with encapsulated bubbles from the reaction may enhance the performance of the chemical detection.

(4) Surface nanodroplet-based extraction and detection can be further enhanced by applying various extractants for higher flexibility. For example, by using an extractant insoluble in water, we can apply a larger sample volume to achieve a higher extraction performance nearing the partition coefficient. Besides, the sensitivity by coupling with GC-MS and fluorescence microscopy was not fully discovered. Other analytical instruments, such as SERS, can also be coupled with the surface droplet nanoextraction for higher sensitivity or accuracy of the detection.

Bibliography

[1] Z. Li, A. Kiyama, H. Zeng, D. Lohse, and X. Zhang, "Speeding up biphasic reactions with surface nanodroplets," *Lab on a Chip*, vol. 20, no. 16, pp. 2965–2974, 2020.

[2] Z. Li, A. Kiyama, H. Zeng, and X. Zhang, "Size effect on the reaction rate of surface nanodroplets," *The Journal of Physical Chemistry C*, vol. 125, no. 28, pp. 15 324–15 334, 2021.

[3] Z. Li, H. Zeng, and X. Zhang, "Growth rates of hydrogen microbubbles in reacting femtoliter droplets," *Langmuir*, vol. 38, no. 21, pp. 6638–6646, 2022.

[4] D. Lohse and X. Zhang, "Surface nanobubbles and nanodroplets," *Reviews of Modern Physics*, vol. 87, no. 3, p. 981, 2015.

[5] A. R. Thiam, R. V. Farese Jr, and T. C. Walther, "The biophysics and cell biology of lipid droplets," *Nature Reviews Molecular Cell Biology*, vol. 14, no. 12, pp. 775–786, 2013.

[6] X. Li, Y. Mao, K. Leng, G. Ye, Y. Sun, and W. Xu, "Enhancement of oxidative desulfurization performance over amorphous titania by doping mil-101 (cr)," *Microporous and Mesoporous Materials*, vol. 254, pp. 114–120, 2017.

[7] Z. Liu, J. Y. Lee, M. Han, W. Chen, and L. M. Gan, "Synthesis and characterization of ptru/c catalysts from microemulsions and emulsions," *Journal of Materials Chemistry*, vol. 12, no. 8, pp. 2453–2458, 2002.

[8] Z. Lin, Z. Zhang, Y. Li, and Y. Deng, "Magnetic nano-fe3o4 stabilized pickering emulsion liquid membrane for selective extraction and separation," *Chemical Engineering Journal*, vol. 288, pp. 305–311, 2016.

[9] M. Okubo, A. Yamada, and T. Matsumoto, "Estimation of morphology of composite polymer emulsion particles by the soap titration method," *Journal of Polymer Science: Polymer Chemistry Edition*, vol. 18, no. 11, pp. 3219–3228, 1980.

[10] L. Wang *et al.*, "Autonomic behaviors in lipase-active oil droplets," *Angewandte Chemie*, vol. 131, no. 4, pp. 1079–1083, 2019.

[11] J. Qian, G. F. Arends, and X. Zhang, "Surface nanodroplets: Formation, dissolution, and applications," *Langmuir*, vol. 35, no. 39, pp. 12 583–12 596, 2019.

[12] R. M. Bain, S. Sathyamoorthi, and R. N. Zare, ""on-droplet" chemistry: The cycloaddition of diethyl azodicarboxylate and quadricyclane," *Angewandte Chemie*, vol. 129, no. 47, pp. 15 279–15 283, 2017.

[13] B. T. Kelly, J.-C. Baret, V. Taly, and A. D. Griffiths, "Miniaturizing chemistry and biology in microdroplets," *Chemical Communications*, no. 18, pp. 1773–1788, 2007.

[14] J. B. Kim, S. Y. Lee, N. G. Min, S. Y. Lee, and S.-H. Kim, "Plasmonic janus microspheres created from pickering emulsion drops," *Advanced Materials*, vol. 32, no. 26, p. 2 001 384, 2020.

[15] K. Chen, Y. Qian, C. Wang, D. Yang, X. Qiu, and B. P. Binks, "Tumor microenvironment-responsive, high internal phase pickering emulsions stabilized by lignin/chitosan oligosaccharide particles for synergistic cancer therapy," *Journal of Colloid and Interface Science*, 2021.

[16] D.-K. Kang, M. M. Ali, K. Zhang, E. J. Pone, and W. Zhao, "Droplet microfluidics for single-molecule and single-cell analysis in cancer research, diagnosis and therapy," *TrAC Trends in Analytical Chemistry*, vol. 58, pp. 145–153, 2014.

[17] Z. Wei, M. Li, H. Zeng, and X. Zhang, "Integrated nanoextraction and colorimetric reactions in surface nanodroplets for combinative analysis," *Analytical Chemistry*, vol. 92, no. 18, pp. 12 442–12 450, 2020.

[18] T. F. Tadros, *Emulsions*. De Gruyter, 2016.

[19] S. Banerjee, F. Liu, D. M. Sanchez, T. J. Martínez, and R. N. Zare, "Pomeranz–fritsch synthesis of isoquinoline: Gas-phase collisional activation opens additional reaction pathways," *Journal of the American Chemical Society*, vol. 139, no. 41, pp. 14 352–14 355, 2017.

[20] J. K. Lee, S. Kim, H. G. Nam, and R. N. Zare, "Microdroplet fusion mass spectrometry for fast reaction kinetics," *Proceedings of the National Academy of Sciences*, vol. 112, no. 13, pp. 3898–3903, 2015.

[21] R. M. Bain, C. J. Pulliam, F. Thery, and R. G. Cooks, "Accelerated chemical reactions and organic synthesis in leidenfrost droplets," *Angewandte Chemie International Edition*, vol. 55, no. 35, pp. 10 478–10 482, 2016.

[22] I. Nam, J. K. Lee, H. G. Nam, and R. N. Zare, "Abiotic production of sugar phosphates and uridine ribonucleoside in aqueous microdroplets," *Proceedings of the National Academy of Sciences*, vol. 114, no. 47, pp. 12 396–12 400, 2017.

[23] I. Nam, H. G. Nam, and R. N. Zare, "Abiotic synthesis of purine and pyrimidine ribonucleosides in aqueous microdroplets," *Proceedings of the National Academy of Sciences*, vol. 115, no. 1, pp. 36–40, 2018.

[24] Y.-H. Lai, S. Sathyamoorthi, R. M. Bain, and R. N. Zare, "Microdroplets accelerate ring opening of epoxides," *Journal of The American Society for Mass Spectrometry*, vol. 29, no. 5, pp. 1036–1043, 2018.

[25] P. L. Urban, "Compartmentalised chemistry: From studies on the origin of life to engineered biochemical systems," *New Journal of Chemistry*, vol. 38, no. 11, pp. 5135–5141, 2014.

[26] V. Vaida, "Prebiotic phosphorylation enabled by microdroplets," *Proceedings of the National Academy of Sciences*, vol. 114, no. 47, pp. 12 359–12 361, 2017.

[27] Y. Ju *et al.*, "Aqueous-microdroplet-driven abiotic synthesis of ribonucleotides," *The Journal of Physical Chemistry Letters*, vol. 13, pp. 567–573, 2022.

[28] J. K. Lee *et al.*, "Condensing water vapor to droplets generates hydrogen peroxide," *Proceedings of the National Academy of Sciences*, vol. 117, no. 49, pp. 30 934–30 941, 2020.

[29] A. Fallah-Araghi *et al.*, "Enhanced chemical synthesis at soft interfaces: A universal reaction-adsorption mechanism in microcompartments," *Physical Review Letters*, vol. 112, no. 2, p. 028 301, 2014.

[30] K. Nakatani, T. Suto, M. Wakabayashi, H.-B. Kim, and N. Kitamura, "Direct analyses of an electrochemically induced dye formation reaction across a single-microdroplet/water interface," *The Journal of Physical Chemistry*, vol. 99, no. 13, pp. 4745–4749, 1995.

[31] K. Nakatani, K. Chikama, H.-B. Kim, and N. Kitamura, "Droplet-size dependence of the electron transfer rate across the single-microdroplet/water interface," *Chemical Physics Letters*, vol. 237, no. 1-2, pp. 133–136, 1995.

[32] K. Nakatani, M. Wakabayashi, K. Chikama, and N. Kitamura, "Electrochemical studies on mass transfer of ferrocene derivatives across a single-nitrobenzene-microdroplet/water interface," *The Journal of Physical Chemistry*, vol. 100, no. 16, pp. 6749–6754, 1996.

[33] C. F. Chamberlayne and R. N. Zare, "Microdroplets can act as electrochemical cells," *The Journal of Chemical Physics*, 2022.

[34] K.-H. Huang, Z. Wei, and R. G. Cooks, "Accelerated reactions of amines with carbon dioxide driven by superacid at the microdroplet interface," *Chemical Science*, vol. 12, no. 6, pp. 2242–2250, 2021.

[35] X. Zhong, H. Chen, and R. N. Zare, "Ultrafast enzymatic digestion of proteins by microdroplet mass spectrometry," *Nature communications*, vol. 11, no. 1, pp. 1–9, 2020.

[36] H. Xiong, J. K. Lee, R. N. Zare, and W. Min, "Strong electric field observed at the interface of aqueous microdroplets," *The Journal of Physical Chemistry Letters*, vol. 11, no. 17, pp. 7423–7428, 2020.

[37] H. Xiong, J. K. Lee, R. N. Zare, and W. Min, "Strong concentration enhancement of molecules at the interface of aqueous microdroplets," *The Journal of Physical Chemistry B*, vol. 124, no. 44, pp. 9938–9944, 2020.

[38] M. F. Toney *et al.*, "Voltage-dependent ordering of water molecules at an electrode–electrolyte interface," *Nature*, vol. 368, no. 6470, pp. 444–446, 1994.

[39] B. P. Dyett and X. Zhang, "Accelerated formation of h2 nanobubbles from a surface nanodroplet reaction," *ACS nano*, vol. 14, no. 9, pp. 10 944–10 953, 2020.

[40] D. N. Mortensen and E. R. Williams, "Theta-glass capillaries in electrospray ionization: Rapid mixing and short droplet lifetimes," *Analytical chemistry*, vol. 86, no. 18, pp. 9315–9321, 2014.

[41] N. Ingle *et al.*, "A chemiresistive gas sensor for sensitive detection of so2 employing ni-mof modified–oh-swnts and–oh-mwnts," *Applied Physics A*, vol. 127, no. 2, pp. 1–10, 2021.

[42] P. Chaikhan, Y. Udnan, R. J. Ampiah-Bonney, and W. C. Chaiyasith, "Air-assisted solvent terminated dispersive liquid–liquid microextraction (aa-st-dllme) for the determination of lead in water and beverage samples by graphite furnace atomic absorption spectrometry," *Microchemical Journal*, vol. 162, p. 105 828, 2021.

[43] Q. T. Lê *et al.*, "Nanostructured raman substrates for the sensitive detection of submicrometer-sized plastic pollutants in water," *Journal of Hazardous Materials*, vol. 402, p. 123 499, 2021.

[44] A. R. Malby, J. D. Whyatt, and R. J. Timmis, "Conditional extraction of air-pollutant source signals from air-quality monitoring," *Atmospheric Environment*, vol. 74, pp. 112–122, 2013.

[45] K. Mao, Z. Yang, H. Zhang, X. Li, and J. M. Cooper, "Based nanosensors to evaluate community-wide illicit drug use for wastewater-based epidemiology," *Water Research*, vol. 189, p. 116 559, 2021.

[46] F. Hansen, E. L. Oiestad, and S. Pedersen-Bjergaard, "Bioanalysis of pharmaceuticals using liquid-phase microextraction combined with liquid chromatography–mass spectrometry," *Journal of Pharmaceutical and Biomedical Analysis*, vol. 189, p. 113 446, 2020.

[47] K. Wang *et al.*, "Synthesis of diboronic acid-based fluorescent probes for the sensitive detection of glucose in aqueous media and biological matrices," *ACS sensors*, vol. 6, no. 4, pp. 1543–1551, 2021.

[48] S. Pal, T. K. Ghosh, R. Ghosh, S. Mondal, and P. Ghosh, "Recent advances in recognition, sensing and extraction of phosphates: 2015 onwards," *Coordination Chemistry Reviews*, vol. 405, p. 213 128, 2020.

[49] Y. Zhang, X. Zhang, and B. Jiao, "Determination of ten pyrethroids in various fruit juices: Comparison of dispersive liquid–liquid microextraction sample preparation and quechers method combined with dispersive liquid–liquid microextraction," *Food Chemistry*, vol. 159, pp. 367–373, 2014.

[50] L. Huang, D.-W. Sun, H. Pu, and Q. Wei, "Development of nanozymes for food quality and safety detection: Principles and recent applications," *Comprehensive Reviews in Food Science and Food Safety*, vol. 18, no. 5, pp. 1496–1513, 2019.

[51] A. Szarka, K. Búčiková, I. Kostić, and S. Hrouzková, "Development of a multiresidue quechers–dllme—fast gc–ms method for determination of selected pesticides in yogurt samples," *Food Analytical Methods*, vol. 13, no. 10, pp. 1829–1841, 2020.

[52] Z. Berk, *Food process engineering and technology*. Academic press, 2018.

[53] C. Hanson, "Recent advances in liquid-liquid extraction," 2013.

[54] E Psillakis and N Kalogerakis, "Developments in single-drop microextraction," *TrAC Trends in Analytical Chemistry*, vol. 21, no. 1, pp. 54–64, 2002.

[55] N Cabaleiro, I De La Calle, C Bendicho, and I Lavilla, "Current trends in liquid–liquid and solid–liquid extraction for cosmetic analysis: A review," *Analytical Methods*, vol. 5, no. 2, pp. 323–340, 2013.

[56] L. Guo, N. binte Nawi, and H. K. Lee, "Fully automated headspace bubble-in-drop microextraction," *Analytical chemistry*, vol. 88, no. 17, pp. 8409–8414, 2016.

[57] Y He and H. K. Lee, "Liquid-phase microextraction in a single drop of organic solvent by using a conventional microsyringe," *Analytical Chemistry*, vol. 69, no. 22, pp. 4634–4640, 1997.

[58] W. Liu and H. K. Lee, "Continuous-flow microextraction exceeding1000-fold concentration of dilute analytes," *Analytical chemistry*, vol. 72, no. 18, pp. 4462–4467, 2000.

[59] M. Rezaee, Y. Assadi, M.-R. M. Hosseini, E. Aghaee, F. Ahmadi, and S. Berijani, "Determination of organic compounds in water using dispersive liquid–liquid microextraction," *Journal of Chromatography a*, vol. 1116, no. 1-2, pp. 1–9, 2006.

[60] M.-I. Leong, M.-R. Fuh, and S.-D. Huang, "Beyond dispersive liquid–liquid microextraction," *Journal of Chromatography a*, vol. 1335, pp. 2–14, 2014.

[61] S. A. Vitale and J. L. Katz, "Liquid droplet dispersions formed by homogeneous liquid- liquid nucleation:"the ouzo effect"," *Langmuir*, vol. 19, no. 10, pp. 4105–4110, 2003.

[62] W.-C. Tsai and S.-D. Huang, "Dispersive liquid–liquid microextraction with little solvent consumption combined with gas chromatography–mass spectrometry for the pretreatment of organochlorine pesticides in aqueous samples," *Journal of Chromatography A*, vol. 1216, no. 27, pp. 5171–5175, 2009.

[63] J. Regueiro, M. Llompart, C. Garcia-Jares, J. C. Garcia-Monteagudo, and R. Cela, "Ultrasound-assisted emulsification–microextraction of emergent contaminants and pesticides in environmental waters," *Journal of Chromatography A*, vol. 1190, no. 1-2, pp. 27–38, 2008.

[64] E. Yiantzi, E. Psillakis, K. Tyrovola, and N. Kalogerakis, "Vortex-assisted liquid–liquid microextraction of octylphenol, nonylphenol and bisphenol-a," *Talanta*, vol. 80, no. 5, pp. 2057–2062, 2010.

[65] X.-Z. Hu, J.-H. Wu, and Y.-Q. Feng, "Molecular complex-based dispersive liquid–liquid microextraction: Analysis of polar compounds in aqueous solution," *Journal of Chromatography A*, vol. 1217, no. 45, pp. 7010–7016, 2010.

[66] Y. Xiao and H. Zhang, "Homogeneous ionic liquid microextraction of the active constituents from fruits of schisandra chinensis and schisandra sphenanthera," *Analytica chimica acta*, vol. 712, pp. 78–84, 2012.

[67] C Almeida, J. Fernandes, and S. Cunha, "A novel dispersive liquid–liquid microextraction (dllme) gas chromatography-mass spectrometry (gc–ms) method for the determination of eighteen biogenic amines in beer," *Food Control*, vol. 25, no. 1, pp. 380–388, 2012.

[68] S. Khodadoust and M. Hadjmohammadi, "Determination of n-methylcarbamate insecticides in water samples using dispersive liquid–liquid microextraction and hplc with the aid of experimental design and desirability function," *Analytica chimica acta*, vol. 699, no. 1, pp. 113–119, 2011.

[69] P. Jovanov *et al.*, "Development of multiresidue dllme and quechers based lc–ms/ms method for determination of selected neonicotinoid insecticides in honey liqueur," *Food research international*, vol. 55, pp. 11–19, 2014.

[70] A. Gong and X. Zhu, "Miniaturized ionic liquid dispersive liquid–liquid microextraction in a coupled-syringe system combined with uv for extraction and determination of danazol in danazol capsule and mice serum," *Spectrochimica Acta Part A: Molecular and Biomolecular Spectroscopy*, vol. 159, pp. 163–168, 2016.

[71] D. Lohse and X. Zhang, "Physicochemical hydrodynamics of droplets out of equilibrium," *Nature Reviews Physics*, vol. 2, no. 8, pp. 426–443, 2020.

[72] X. H. Zhang and W. Ducker, "Interfacial oil droplets," *Langmuir*, vol. 24, no. 1, pp. 110–115, 2008.

[73] Y. Liu and X. Zhang, "Nanobubble stability induced by contact line pinning," *The Journal of chemical physics*, vol. 138, no. 1, p. 014 706, 2013.

[74] Y. Liu, J. Wang, X. Zhang, and W. Wang, "Contact line pinning and the relationship between nanobubbles and substrates," *The Journal of chemical physics*, vol. 140, no. 5, p. 054 705, 2014.

[75] D. Lohse, X. Zhang, *et al.*, "Pinning and gas oversaturation imply stable single surface nanobubbles," *Physical Review E*, vol. 91, no. 3, p. 031 003, 2015.

[76] J. D. Smith *et al.*, "Droplet mobility on lubricant-impregnated surfaces," *Soft Matter*, vol. 9, no. 6, pp. 1772–1780, 2013.

[77] M. Li, B. Dyett, H. Yu, V. Bansal, and X. Zhang, "Functional femtoliter droplets for ultrafast nanoextraction and supersensitive online microanalysis," *Small*, vol. 15, no. 1, p. 1 804 683, 2019.

[78] M. Li, R. Cao, B. Dyett, and X. Zhang, "Encapsulated nanodroplets for enhanced fluorescence detection by nano-extraction," *Small*, vol. 16, no. 47, p. 2 004 162, 2020.

[79] J. Qian *et al.*, "One-step nanoextraction and ultrafast microanalysis based on nanodroplet formation in an evaporating ternary liquid microfilm," *Advanced Materials Technologies*, vol. 5, no. 2, p. 1 900 740, 2020.

[80] J. B. You, D. Lohse, and X. Zhang, "Surface nanodroplet-based nanoextraction from sub-milliliter volumes of dense suspensions," *Lab on a Chip*, 2021.

[81] J. Y. Lee *et al.*, "Near-field focusing and magnification through self-assembled nanoscale spherical lenses," *Nature*, vol. 460, no. 7254, pp. 498–501, 2009.

[82] Z. Wang *et al.*, "Optical virtual imaging at 50 nm lateral resolution with a white-light nanoscope," *Nature communications*, vol. 2, no. 1, pp. 1–6, 2011.

[83] H. Yang, L. Fu, L. Wei, J. Liang, and B. P. Binks, "Compartmentalization of incompatible reagents within pickering emulsion droplets for one-pot cascade reactions," *Journal of the American Chemical Society*, vol. 137, no. 3, pp. 1362–1371, 2015.

[84] M. Zhang, L. Wei, H. Chen, Z. Du, B. P. Binks, and H. Yang, "Compartmentalized droplets for continuous flow liquid–liquid interface catalysis," *Journal of the American Chemical Society*, vol. 138, no. 32, pp. 10 173–10 183, 2016.

[85] H. Sirringhaus *et al.*, "High-resolution inkjet printing of all-polymer transistor circuits," *Science*, vol. 290, no. 5499, pp. 2123–2126, 2000.

[86] L. Wu *et al.*, "Printing patterned fine 3d structures by manipulating the three phase contact line," *Advanced Functional Materials*, vol. 25, no. 15, pp. 2237–2242, 2015.

[87] F. Ganachaud and J. L. Katz, "Nanoparticles and nanocapsules created using the ouzo effect: Spontaneous emulsification as an alternative to ultrasonic and high-shear devices," *ChemPhysChem*, vol. 6, no. 2, pp. 209–216, 2005.

[88] S. Prévost, S. Krickl, S. Marcelja, W. Kunz, T. Zemb, and I. Grillo, "Spontaneous ouzo emulsions coexist with pre-ouzo ultraflexible microemulsions," *Langmuir*, vol. 37, no. 13, pp. 3817–3827, 2021.

[89] C. Goubault *et al.*, "The ouzo effect: A tool to elaborate high-payload nanocapsules," *Journal of Controlled Release*, vol. 324, pp. 430–439, 2020.

[90] V. C. F. Mosqueira, P. Legrand, H. Pinto-Alphandary, F. Puisieux, and G. Barratt, "Poly (d, l-lactide) nanocapsules prepared by a solvent displacement process: Influence of the composition on physicochemical and structural properties," *Journal of pharmaceutical sciences*, vol. 89, no. 5, pp. 614–626, 2000.

[91] A. Ma, J. Xu, and H. Xu, "Impact of spontaneously adsorbed hydroxide ions on emulsification via solvent shifting," *The Journal of Physical Chemistry C*, vol. 118, no. 40, pp. 23 175–23 180, 2014.

[92] R Bodmeier, H Chen, P Tyle, and P Jarosz, "Spontaneous formation of drug-containing acrylic nanoparticles," *Journal of microencapsulation*, vol. 8, no. 2, pp. 161–170, 1991.

[93] E. Lepeltier, C. Bourgaux, and P. Couvreur, "Nanoprecipitation and the "ouzo effect": Application to drug delivery devices," *Advanced drug delivery reviews*, vol. 71, pp. 86–97, 2014.

[94] J. Aubry, F. Ganachaud, J.-P. Cohen Addad, and B. Cabane, "Nanoprecipitation of polymethylmethacrylate by solvent shifting: 1. boundaries," *Langmuir*, vol. 25, no. 4, pp. 1970–1979, 2009.

[95] X. H. Zhang and W. Ducker, "Formation of interfacial nanodroplets through changes in solvent quality," *Langmuir*, vol. 23, no. 25, pp. 12 478–12 480, 2007.

[96] X. Zhang *et al.*, "Formation of surface nanodroplets under controlled flow conditions," *Proceedings of the National Academy of Sciences*, vol. 112, no. 30, pp. 9253–9257, 2015.

[97] Z. Lu, H. Xu, H. Zeng, and X. Zhang, "Solvent effects on the formation of surface nanodroplets by solvent exchange," *Langmuir*, vol. 31, no. 44, pp. 12 120–12 125, 2015.

[98] Z. Lu, S. Peng, and X. Zhang, "Influence of solution composition on the formation of surface nanodroplets by solvent exchange," *Langmuir*, vol. 32, no. 7, pp. 1700–1706, 2016.

[99] C. Xu, S. Peng, G. G. Qiao, V. Gutowski, D. Lohse, and X. Zhang, "Nanobubble formation on a warmer substrate," *Soft Matter*, vol. 10, no. 39, pp. 7857–7864, 2014.

[100] A. Brotchie and X. H. Zhang, "Response of interfacial nanobubbles to ultrasound irradiation," *Soft Matter*, vol. 7, no. 1, pp. 265–269, 2011.

[101] B. Dyett, A. Kiyama, M. Rump, Y. Tagawa, D. Lohse, and X. Zhang, "Growth dynamics of surface nanodroplets during solvent exchange at varying flow rates," *Soft matter*, vol. 14, no. 25, pp. 5197–5204, 2018.

[102] G. Taylor, "Dispersion of a solute in a solvent under laminar conditions," *Proc. R. Soc. London, Ser. A*, vol. 219, pp. 186–203, 1953.

[103] G. I. Taylor, "Dispersion of soluble matter in solvent flowing slowly through a tube," *Proceedings of the Royal Society of London. Series A. Mathematical and Physical Sciences*, vol. 219, no. 1137, pp. 186–203, 1953.

[104] R. Aris, "On the dispersion of a solute in a fluid flowing through a tube," *Proceedings of the Royal Society of London. Series A. Mathematical and Physical Sciences*, vol. 235, no. 1200, pp. 67–77, 1956.

[105] R. Aris, "On the dispersion of a solute by diffusion, convection and exchange between phases," *Proceedings of the Royal Society of London. Series A. Mathematical and Physical Sciences*, vol. 252, no. 1271, pp. 538–550, 1959.

[106] H. Yu, S. Maheshwari, J. Zhu, D. Lohse, and X. Zhang, "Formation of surface nanodroplets facing a structured microchannel wall," *Lab on a Chip*, vol. 17, no. 8, pp. 1496–1504, 2017.

[107] H. Yu, Z. Lu, D. Lohse, and X. Zhang, "Gravitational effect on the formation of surface nanodroplets," *Langmuir*, vol. 31, no. 46, pp. 12 628–12 634, 2015.

[108] M. Li, L. Bao, H. Yu, and X. Zhang, "Formation of multicomponent surface nanodroplets by solvent exchange," *The Journal of Physical Chemistry C*, vol. 122, no. 15, pp. 8647–8654, 2018.

[109] C. Xu *et al.*, "Collective interactions in the nucleation and growth of surface droplets," *Soft Matter*, vol. 13, no. 5, pp. 937–944, 2017.

[110] L. Bao, A. R. Rezk, L. Y. Yeo, and X. Zhang, "Highly ordered arrays of femtoliter surface droplets," *small*, vol. 11, no. 37, pp. 4850–4855, 2015.

[111] L. Bao, Z. Werbiuk, D. Lohse, and X. Zhang, "Controlling the growth modes of femtoliter sessile droplets nucleating on chemically patterned surfaces," *The journal of physical chemistry letters*, vol. 7, no. 6, pp. 1055–1059, 2016.

[112] S. Peng, D. Lohse, and X. Zhang, "Spontaneous pattern formation of surface nanodroplets from competitive growth," *ACS Nano*, vol. 9, no. 12, pp. 11 916–11 923, 2015.

[113] B. Dyett, H. Hao, D. Lohse, and X. Zhang, "Coalescence driven self-organization of growing nanodroplets around a microcap," *Soft matter*, vol. 14, no. 14, pp. 2628–2637, 2018.

[114] H. Yu, M. Rump, S. Maheshwari, L. Bao, and X. Zhang, "Growth of nanodroplets on a still microfiber under flow conditions," *Physical chemistry chemical physics*, vol. 20, no. 27, pp. 18 252–18 261, 2018.

[115] X. Zhang *et al.*, "Mixed mode of dissolving immersed nanodroplets at a solid–water interface," *Soft Matter*, vol. 11, no. 10, pp. 1889–1900, 2015.

[116] M. Li, B. Dyett, and X. Zhang, "Automated femtoliter droplet-based determination of oil–water partition coefficient," *Analytical chemistry*, vol. 91, no. 16, pp. 10 371–10 375, 2019.

[117] W. Wang, C. Yang, and C. M. Li, "Efficient on-demand compound droplet formation: From microfluidics to microdroplets as miniaturized laboratories," *Small*, vol. 5, no. 10, pp. 1149–1152, 2009.

[118] W. Feng, E. Ueda, and P. A. Levkin, "Droplet microarrays: From surface patterning to high-throughput applications," *Advanced Materials*, vol. 30, no. 20, p. 1 706 111, 2018.

[119] M. Guardingo, F. Busqué, and D. Ruiz-Molina, "Reactions in ultra-small droplets by tip-assisted chemistry," *Chemical Communications*, vol. 52, no. 78, pp. 11 617–11 626, 2016.

[120] X. Yan, R. M. Bain, and R. G. Cooks, "Organic reactions in microdroplets: Reaction acceleration revealed by mass spectrometry," *Angewandte Chemie International Edition*, vol. 55, no. 42, pp. 12 960–12 972, 2016.

[121] J. K. Lee, S. Banerjee, H. G. Nam, and R. N. Zare, "Acceleration of reaction in charged microdroplets," *Quarterly Reviews of Biophysics*, vol. 48, no. 4, pp. 437–444, 2015.

[122] Z. Wei, M. Wleklinski, C. Ferreira, and R. G. Cooks, "Reaction acceleration in thin films with continuous product deposition for organic synthesis," *Angewandte Chemie*, vol. 129, no. 32, pp. 9514–9518, 2017.

[123] E. C. Griffith and V. Vaida, "In situ observation of peptide bond formation at the water–air interface," *Proceedings of the National Academy of Sciences*, vol. 109, no. 39, pp. 15 697–15 701, 2012.

[124] B. P. Wiebenga-Sanford, J. DiVerdi, C. D. Rithner, and N. E. Levinger, "Nanoconfinement's dramatic impact on proton exchange between glucose and water," *The Journal of Physical Chemistry Letters*, vol. 7, no. 22, pp. 4597–4601, 2016.

[125] J. K. Lee, D. Samanta, H. G. Nam, and R. N. Zare, "Spontaneous formation of gold nanostructures in aqueous microdroplets," *Nature Communications*, vol. 9, no. 1, p. 1562, 2018.

[126] B. Carroll and C. Hidrovo, "Experimental investigation of inertial mixing in colliding droplets," *Heat Transfer Engineering*, vol. 34, no. 2-3, pp. 120–130, 2013.

[127] L. Bao *et al.*, "Flow-induced dissolution of femtoliter surface droplet arrays," *Lab on a Chip*, vol. 18, no. 7, pp. 1066–1074, 2018.

[128] M. Lessel *et al.*, "Self-assembled silane monolayers: An efficient step-by-step recipe for high-quality, low energy surfaces," *Surface and Interface Analysis*, vol. 47, no. 5, pp. 557–564, 2015.

[129] I. Langmuir and V. J. Schaefer, "Composition of fatty acid films on water containing calcium or barium salts," *Journal of the American Chemical Society*, vol. 58, no. 2, pp. 284–287, 1936.

[130] J. Zhang, C. Yang, and Z.-S. Mao, "Mass and heat transfer from or to a single sphere in simple extensional creeping flow," *AIChE Journal*, vol. 58, no. 10, pp. 3214–3223, 2012.

[131] A. Mustafa *et al.*, "Enhanced dissolution of liquid microdroplets in the extensional creeping flow of a hydrodynamic trap," *Langmuir*, vol. 32, no. 37, pp. 9460–9467, 2016.

[132] X. Wang *et al.*, "Ionophore-based biphasic chemical sensing in droplet microfluidics," *Angewandte Chemie*, vol. 131, no. 24, pp. 8176–8180, 2019.

[133] D. A. Holland-Moritz *et al.*, "Mass activated droplet sorting (mads) enables high-throughput screening of enzymatic reactions at nanoliter scale," *Angewandte Chemie International Edition*, vol. 59, no. 11, pp. 4470–4477, 2020.

[134] F. Zhang *et al.*, "Pickering emulsions stabilized by a metal–organic framework (mof) and graphene oxide (go) for producing mof/go composites," *Soft Matter*, vol. 13, no. 40, pp. 7365–7370, 2017.

[135] D. Liu *et al.*, "Surfactant assembly within pickering emulsion droplets for fabrication of interior-structured mesoporous carbon microspheres," *Angewandte Chemie*, vol. 130, no. 34, pp. 11 065–11 070, 2018.

[136] Z. Wang, T. Qiu, L. Guo, J. Ye, L. He, and X. Li, "Polymerization induced shaping of pickering emulsion droplets: From simple hollow microspheres to molecularly imprinted multicore microrattles," *Chemical Engineering Journal*, vol. 332, pp. 409–418, 2018.

[137] A. C. Chinyerenwa *et al.*, "Structure and thermal properties of porous polylactic acid membranes prepared via phase inversion induced by hot water droplets," *Polymer*, vol. 141, pp. 62–69, 2018.

[138] S. Tu, Y. Zhao, H. Tan, H. Yu, X. Zhu, and H. Wang, "Ultralight silica foams with a hierarchical pore structure via a surfactant-free high internal phase emulsion process," *Langmuir*, vol. 34, no. 35, pp. 10 381–10 388, 2018.

[139] E. Su *et al.*, "Highly stable and thermo-responsive gel foams by synergistically combining glycyrrhizic acid nanofibrils and cellulose nanocrystals," *Journal of Colloid and Interface Science*, 2020.

[140] P. Kanitthamniyom and Y. Zhang, "Magnetic digital microfluidics on a bioinspired surface for point-of-care diagnostics of infectious disease," *Electrophoresis*, vol. 40, no. 8, pp. 1178–1185, 2019.

[141] M. J. Rothrock, K. L. Hiett, B. H. Kiepper, K. Ingram, A. Hinton, *et al.*, "Quantification of zoonotic bacterial pathogens within commercial poultry processing water samples using droplet digital pcr," *Advances in Microbiology*, vol. 3, no. 05, p. 403, 2013.

[142] L. Baraban *et al.*, "Millifluidic droplet analyser for microbiology," *Lab on a Chip*, vol. 11, no. 23, pp. 4057–4062, 2011.

[143] G. Baffou, J. Polleux, H. Rigneault, and S. Monneret, "Super-heating and micro-bubble generation around plasmonic nanoparticles under cw illumination," *The Journal of Physical Chemistry C*, vol. 118, no. 9, pp. 4890–4898, 2014.

[144] B. M. Marsh, K. Iyer, and R. G. Cooks, "Reaction acceleration in electrospray droplets: Size, distance, and surfactant effects," *Journal of The American Society for Mass Spectrometry*, vol. 30, no. 10, pp. 2022–2030, 2019.

[145] B. Dyett, Q. Zhang, Q. Xu, X. Wang, and X. Zhang, "Extraordinary focusing effect of surface nanolenses in total internal reflection mode," *ACS Central Science*, vol. 4, no. 11, pp. 1511–1519, 2018.

[146] S. Mondal, S. Acharya, R. Biswas, B. Bagchi, and R. N. Zare, "Enhancement of reaction rate in small-sized droplets: A combined analytical and simulation study," *The Journal of Chemical Physics*, vol. 148, no. 24, p. 244 704, 2018.

[147] A. J. Ingram, C. L. Boeser, and R. N. Zare, "Going beyond electrospray: Mass spectrometric studies of chemical reactions in and on liquids," *Chemical science*, vol. 7, no. 1, pp. 39–55, 2016.

[148] B. P. Dyett, M. Li, H. Zhao, and X. Zhang, "Plasmonic nanobubbles in "armored" surface nanodroplets," *The Journal of Physical Chemistry C*, vol. 123, no. 49, pp. 29 866–29 874, 2019.

[149] J. K. Lee, D. Samanta, H. G. Nam, and R. N. Zare, "Micrometer-sized water droplets induce spontaneous reduction," *Journal of the American Chemical Society*, vol. 141, no. 27, pp. 10 585–10 589, 2019.

[150] Z. Wei, Y. Li, R. G. Cooks, and X. Yan, "Accelerated reaction kinetics in microdroplets: Overview and recent developments," *Annual Review of Physical Chemistry*, vol. 71, pp. 31–51, 2020.

[151] S. Narayan, J. Muldoon, M. Finn, V. V. Fokin, H. C. Kolb, and K. B. Sharpless, "On water: Unique reactivity of organic compounds in aqueous suspension," *Angewandte Chemie International Edition*, vol. 44, no. 21, pp. 3275–3279, 2005.

[152] Z. Meng, M. Zhang, and H. Yang, "Pickering emulsion droplets hosting ionic liquid catalysts for continuous-flow cyanosilylation reaction," *Green Chemistry*, vol. 21, no. 3, pp. 627–633, 2019.

[153] H. Li *et al.*, "Application of droplet digital pcr to detect the pathogens of infectious diseases," *Bioscience Reports*, vol. 38, no. 6, 2018.

[154] J. M. P. Gutierrez, T. Hinkley, J. W. Taylor, K. Yanev, and L. Cronin, "Evolution of oil droplets in a chemorobotic platform," *Nature Communications*, vol. 5, no. 1, p. 5571, 2014.

[155] S. Nakayama, T. Kojima, M. Kaburagi, T. Kikuchi, K. Asakura, and T. Banno, "Chemotaxis of oil droplets and their phase transition to aggregates with membrane structures in surfactant solution containing metal salts," *ChemSystemsChem*, no. n/a, e2100035, eprint: https://chemistry-europe.onlinelibrary.wiley.com/doi/pdf/10.1002/syst.202100035.

[156] X. Fan, M. Sun, L. Sun, and H. Xie, "Ferrofluid droplets as liquid microrobots with multiple deformabilities," *Advanced Functional Materials*, vol. 30, no. 24, p. 2 000 138, 2020. eprint: https://onlinelibrary.wiley.com/doi/pdf/10.1002/adfm.202000138.

[157] K. J. Vannoy, I. Lee, K. Sode, and J. E. Dick, "Electrochemical quantification of accelerated fadgdh rates in aqueous nanodroplets," *Proceedings of the National Academy of Sciences*, vol. 118, no. 25, 2021.

[158] S. Banerjee and R. N. Zare, "Syntheses of isoquinoline and substituted quinolines in charged microdroplets," *Angewandte Chemie*, vol. 127, no. 49, pp. 15 008–15 012, 2015.

[159] R. M. Bain, C. J. Pulliam, and R. G. Cooks, "Accelerated hantzsch electrospray synthesis with temporal control of reaction intermediates," *Chemical Science*, vol. 6, no. 1, pp. 397–401, 2015.

[160] V Kulkarni and P. Sojka, "Bag breakup of low viscosity drops in the presence of a continuous air jet," *Physics of Fluids*, vol. 26, no. 7, p. 072 103, 2014.

[161] V. Kulkarni, V. Y. Lolla, S. R. Tamvada, N. Shirdade, and S. Anand, "Coalescence and spreading of drops on liquid pools," *Journal of Colloid and Interface Science*, vol. 586, pp. 257–268, 2021.

[162] B. Zheng, X. Jin, J. Liu, and H. Cheng, "Accelerated metal-free hydration of alkynes within milliseconds in microdroplets," *ACS Sustainable Chemistry & Engineering*, vol. 9, pp. 4383–4390, 2021.

[163] G. Rovelli, M. I. Jacobs, M. D. Willis, R. J. Rapf, A. M. Prophet, and K. R. Wilson, "A critical analysis of electrospray techniques for the determination of accelerated rates and mechanisms of chemical reactions in droplets," *Chem. Sci.*, vol. 11, pp. 13 026–13 043, 48 2020.

[164] B. J. Burris and A. K. Badu-Tawiah, "Enzyme-catalyzed hydrolysis of lipids in immiscible microdroplets studied by contained-electrospray ionization," *Analytical Chemistry*, 2021.

[165] W. Feng, E. Ueda, and P. A. Levkin, "Droplet microarrays: From surface patterning to high-throughput applications," *Advanced Materials*, vol. 30, no. 20, p. 1 706 111, 2018.

[166] L. Zhou *et al.*, "Wetting behavior of surface nanodroplets regulated by periodic nanostructured surfaces," *ACS Applied Materials & Interfaces*, vol. 13, no. 46, pp. 55 726–55 734, 2021.

[167] Z. Wei *et al.*, "In-situ fabrication of metal oxide nanocaps based on biphasic reactions with surface nanodroplets," *Journal of Colloid and Interface Science*, vol. 608, pp. 2235–2245, 2022.

[168] M. Ramiasa *et al.*, "Contact line motion on nanorough surfaces: A thermally activated process," *Journal of the American Chemical Society*, vol. 135, no. 19, pp. 7159–7171, 2013.

[169] E. Asenath Smith and W. Chen, "How to prevent the loss of surface functionality derived from aminosilanes," *Langmuir*, vol. 24, no. 21, pp. 12 405–12 409, 2008.

[170] C. Wakai and M. Nakahara, "Attractive potential effect on the self-diffusion coefficients of a solitary water molecule in organic solvents," *The Journal of Chemical Physics*, vol. 106, no. 18, pp. 7512–7518, 1997.

[171] P. Lv *et al.*, "Self-propelled detachment upon coalescence of surface bubbles," *Phys. Rev. Lett.*, vol. 127, p. 235 501, 23 2021.

[172] K Sporka, J Hanika, V Ržička, and M Halousek, "Diffusion of gases in liquids. iii. diffusion coefficients of hydrogen in organic solvents," *Collection of Czechoslovak Chemical Communications*, vol. 36, no. 6, pp. 2130–2136, 1971.

[173] Z. Wei, J. B. You, H. Zeng, and X. Zhang, "Interfacial partitioning enhances microextraction by multicomponent nanodroplets," *The Journal of Physical Chemistry C*, vol. 126, no. 3, pp. 1326–1336, 2022.

[174] H. Wang, Z. Wei, S. I. Vagin, X. Zhang, B. Rieger, and A. Meldrum, "Ultrasensitive picomolar detection of aqueous acids in microscale fluorescent droplets," *ACS Sensors*, vol. 7, no. 1, pp. 245–252, Jan. 2022.

[175] C. Vega-Sánchez, S. Peppou-Chapman, L. Zhu, and C. Neto, "Nanobubbles explain the large slip observed on lubricant-infused surfaces," *Nature Communications*, vol. 13, no. 1, p. 351, 2022.

[176] X. Zhang and D. Lohse, "Perspectives on surface nanobubbles," *Biomicrofluidics*, vol. 8, no. 4, p. 041 301, 2014. eprint: https://doi.org/10.1063/1.4891097.

[177] R. H. Abou-Saleh, F. J. Armistead, D. V. Batchelor, B. R. Johnson, S. A. Peyman, and S. D. Evans, "Horizon: Microfluidic platform for the production of therapeutic microbubbles and nanobubbles," *Review of Scientific Instruments*, vol. 92, no. 7, p. 074 105, 2021.

[178] M. Fayyaz, M. Jabeen, M. S. Tsipursky, and J. Irudayaraj, "Dextran-based oxygen nanobubbles for treating inner retinal hypoxia," *ACS Applied Nano Materials*, vol. 4, no. 7, pp. 6583–6593, 2021.

[179] Y. Yamini, M. Rezazadeh, and S. Seidi, "Liquid-phase microextraction - the different principles and configurations," *Trends Anal. Chem.*, vol. 112, no. 30, pp. 264–272, 2019.

[180] M. A. Jeannot and F. F. Cantwell, "Solvent microextraction into a single drop," *Anal. Chem.*, vol. 68, no. 13, pp. 2236–2240, 1996.

[181] Y. He and H. K. Lee, "Liquid-phase microextraction in a single drop of organic solvent by using a conventional microsyringe," *Anal. Chem.*, vol. 69, no. 22, pp. 4634–4640, 1997.

[182] K. E. Rasmussen and S. Pedersen-Bjergaard, "Developments in hollow fibre-based liquid-phase microextraction," *Trends Anal. Chem.*, vol. 23, no. 1, pp. 1–10, 2004.

[183] M. Tobiszewski, A. Mechlińska, and J. Namieśnik, "Green analytical chemistry—theory and practice," *Chemical Society Reviews*, vol. 39, no. 8, pp. 2869–2878, 2010.

[184] M. Tobiszewski, "Metrics for green analytical chemistry," *Analytical methods*, vol. 8, no. 15, pp. 2993–2999, 2016.

[185] B. Dyett, Q. Zhang, Q. Xu, X. Wang, and X. Zhang, "Extraordinary focusing effect of surface nanodroplets in total internal reflection mode," *ACS Cent. Sci*, vol. 4, no. 11, pp. 1511–1519, 2018.

[186] F. Tohidi and Z. Cai, "Gc/ms analysis of triclosan and its degradation by-products in wastewater and sludge samples from different treatments," *Environmental Science and Pollution Research*, vol. 22, no. 15, pp. 11 387–11 400, 2015.

[187] B. Quan *et al.*, "Technology and principle of removing triclosan from aqueous media: A review," *Chemical Engineering Journal*, vol. 378, p. 122 185, 2019.

[188] C. W. Levy *et al.*, "Molecular basis of triclosan activity," *Nature*, vol. 398, no. 6726, pp. 383–384, 1999.

[189] K. Liu, L. Chen, L. Huang, Y. Ni, and B. Sun, "Enhancing antibacterium and strength of cellulosic paper by coating triclosan-loaded nanofibrillated cellulose (nfc)," *Carbohydrate polymers*, vol. 117, pp. 996–1001, 2015.

[190] R.-S. Zhao, X. Wang, J. Sun, C. Hu, and X.-K. Wang, "Determination of triclosan and triclocarban in environmental water samples with ionic liquid/ionic liquid dispersive liquid-liquid microextraction prior to hplc-esi-ms/ms," *Microchimica Acta*, vol. 174, no. 1, pp. 145–151, 2011.

[191] A. Mpupa, G. P. Mashile, and P. N. Nomngongo, "Vortex assisted-supramolecular solvent based microextraction coupled with spectrophotometric determination of triclosan in environmental water samples," *Open Chemistry*, vol. 15, no. 1, pp. 255–262, 2017.

[192] C. Zheng, J. Zhao, P. Bao, J. Gao, and J. He, "Dispersive liquid–liquid microextraction based on solidification of floating organic droplet followed by high-performance liquid chromatography with ultraviolet detection and liquid chromatography–tandem mass spectrometry for the determination of triclosan and 2, 4-dichlorophenol in water samples," *Journal of Chromatography A*, vol. 1218, no. 25, pp. 3830–3836, 2011.

[193] M. A. Farajzadeh, M. R. A. Mogaddam, and L. Esrafili, "Surfactant-less water emulsion based dispersive liquid–liquid microextraction for determination of organophosphorus pesticides in aqueous samples," *Analytical Methods*, vol. 7, no. 18, pp. 7899–7906, 2015.

[194] P. Zohrabi, M. Shamsipur, M. Hashemi, and B. Hashemi, "Liquid-phase microextraction of organophosphorus pesticides using supramolecular solvent as a carrier for ferrofluid," *Talanta*, vol. 160, pp. 340–346, 2016.

[195] J. W. Fleeger, K. R. Carman, and R. M. Nisbet, "Indirect effects of contaminants in aquatic ecosystems," *Science of the total environment*, vol. 317, no. 1-3, pp. 207–233, 2003.

[196] B. K. Singh and A. Walker, "Microbial degradation of organophosphorus compounds," *FEMS microbiology reviews*, vol. 30, no. 3, pp. 428–471, 2006.

[197] K. R. Solomon, W. M. Williams, D. Mackay, J. Purdy, J. M. Giddings, and J. P. Giesy, "Properties and uses of chlorpyrifos in the united states," *Ecological risk assessment for chlorpyrifos in terrestrial and aquatic systems in the United States*, pp. 13–34, 2014.